UNIVERSITÀ
DEGLI STUDI
DI PADOVA

UNIVERSITY OF PADOVA

DEPARTMENT OF ELECTRICAL ENGINEERING

Advanced Design of Direct Drive PM Machines

Supervisor: Prof. Silverio Bolognani

PhD Student: Emanuele Fornasiero

1 febbraio 2010

A Vania e alla mia famiglia

Contents

Sommario

Il seguente lavoro di tesi prende in considerazione alcuni aspetti riguardanti il progetto di macchine a magneti permanenti. Il crescente interesse rivolto a questo tipo di macchine è dovuto ad alcune caratteristiche che esse presentano: alta densità di coppia, possibilità di eliminazione del riduttore di giri e quindi conseguente riduzione di costi e manutenzione, ecc. Molte applicazioni si trovano nel campo della generazione eolica, della trazione elettrica e della trazione a fune. Le particolarità costruttive di tali macchine, quali ad esempio la presenza di avvolgimenti a cave frazionarie, le notevoli dimensioni e le grosse potenze che esse possono presentare, portano a dover considerare alcune problematiche spesso non propriamente investigate durante la progettazione.

A questo scopo, il lavoro di tesi analizza i seguenti due aspetti: le perdite rotoriche in macchine con avvolgimenti frazionari e la tolleranza ai guasti.

Perdite rotoriche in macchine con avvolgimenti frazionari - Per quanto riguarda le perdite rotoriche, esse risultano assumere una peculiare importanza in grosse macchine, dove la loro presenza risulta spesso comprometterne il funzionamento.

In macchine di piccola potenza, l'interesse al miglioramento del rendimento porta a doverne considerare la presenza fin dalle prime fasi di progetto.

I primi capitoli della seguente tesi analizzano quindi il fenomeno delle perdite rotoriche, cercando di fornire un approccio generale e delle regole di progetto di macchine a ridotte perdite rotoriche.

Il capitolo 1 analizza analiticamente l'effetto del contenuto armonico della forza magnetomotrice al traferro. Vengono proposti modelli linearizzati, con lo scopo di valutare l'impatto delle grandezze coinvolte sulle perdite rotoriche. Sono ricavate delle regole generali, utili nel progetto di macchine a ridotte perdite rotoriche.

Il capitolo 2 fornisce alcuni confronti utilizzando il calcolo agli elementi finiti.

Il capitolo 3 propone un indice di perdita rotorica per poter confrontare velocemente diverse configurazioni di avvolgimento in relazione alle perdite rotoriche da essi indotte.

Il capitolo 4 analizza e fornisce le misure delle perdite rotoriche in un prototipo di motore assiale.

Tolleranza ai guasti - Gli azionamenti multifase sono impiegati in alcune applicazioni (aeronautica, automotive) dove la continuità di funzionamento è una caratteristica essenziale.

Rispetto ad azionamenti trifase, essi offrono alcuni miglioramenti in termini di rendimento, densità di coppia e ridotte oscillazioni di coppia.

In grosse macchine la presenza di più sezioni permette di poter utilizzare la macchina anche in caso di guasto, seppur con potenza ridotta.

Sono comunque necessarie delle tecniche di diagnostica, atte ad individuare l'insorgere del guasto e la sua gravità. Ciò permette sia di programmare la manutenzione che di prendere gli opportuni provvedimenti per evitare che il guasto si propaghi.

La seconda parte della tesi tratta dei guasti nei sistemi multifase.

Il capitolo 5 introduce un motore pentafase, usato nei successivi capitoli per le prove sperimentali. Il comportamento del motore è analizzato in caso di apertura di una o di due fasi.

Il capitolo 6 fornisce un confronto tra due tipologie di azionamenti multifase, mostrando i vantaggi e svantaggi di entrambe le soluzioni: un azionamento doppio–trifase e un azionamento pentafase.

Il capitolo 7 si occupa del comportamento di sistemi pentafase in caso di asimmetria. Lo studio è basato sullo spettro armonico dei vettori spaziali.

La modellazione del corto circuito di alcune spire è affrontata nel capitolo 8, che presenta risultati analitici e sperimentali e propone una procedura di diagnostica di tale tipo di guasti.

Infine, il capitolo 9 conclude la trattazione riguardante i guasti definendo un indice diagnostico all'interno di una architettura di azionamento pentafase.

Introduction

Permanent magnet (PM) machines can be divided in two categories: surface–mounted permanent magnet (SPM) machines and interior–mounted permanent magnet (IPM) machines. Both machines can be considered to have the same stator configuration. The former represents a machine which rotor is characterized by PMs mounted on the rotor surface; the latter describes a machine in which the PMs are mounted inside the rotor structure. Among IPM machines, it is possible to find two categories: IPM machines with radial magnetization and IPM machines with tangential magnetization.

PM machines are used in many applications spanning from low to large power applications. They can be operated both as motors and as generators. The main applications as motors are naval propulsion, presses, and so on. PM generators are instead mainly used in wind power applications. In these kind of applications, the choice of using PM machines rather than induction or wound machines is mainly due to the possibility of removing the gear box. In fact, PM machines can be suitably designed to operate in direct–drive way.

The PM machines design has some opened issues; they mainly regard rotor losses and multiphase systems.

Rotor losses

In recent years, in medium and high power applications, the trend is to employ direct–drive solutions. This leads to the adoption of PM machines with a large number of poles and the use of fractional–slot windings. Such solutions yield high torque density, low torque ripple, and high efficiency [1, 2]. However, the fractional–slot machines are characterized by a high contents of space harmonics in the air–gap MMF distribution [3]. These harmonics move asynchronously with the rotor, inducing currents in all rotor conductive parts [4–6].

Although the problem of rotor losses is not new, and some papers are devoted to the computation of rotor losses of PM machines [5, 6], they do not give general rules to design the fractional–slot PM motors with reduced rotor losses.

Some analytical models to compute the rotor losses in surface–mounted PM (SPM) motors

have been proposed recently in both integral–slot [7–9] and fractional–slot PM motors [10, 11].

The model of the machine is simplified, the rotor being formed by concentric cylindrical layers. In spite of the adopted simplification of the geometry, complex equations are derived, based on a Fourier series expansion of the Bessel functions.

Other approaches are based on a step–to–step finite element computation of the rotor losses. The actual geometry of the machine is considered, assuming actual PM shape. The achieved results are generally accurate, but the time required to the computation is high. In addition, each change in the machine geometry or in the combination of the number of slots and poles requires a further computation of the losses.

On the contrary, a rapid estimation of the rotor losses (to the aim of settling if a machine solution is suitable or not) is a key issue in any design process. And this is particularly important for a correct choice of the combination of machine slots and poles. The amount of rotor losses assumes a peculiar importance in large machines where the number of slots and poles is high, such as in wind turbine PM generators, PM motors in direct drive lift applications, and so on.

In order to make the comparison faster, a straight–lined model is often adopted [12, 13]. This model is adopted as a practical tool for the choice of slot–pole combination.

The early chapters of the following thesis analyzes the phenomenon of rotor losses, attempting to provide a comprehensive approach and rules for designing machines with reduced rotor losses. Chapter 1 analyze in detail the effect of the harmonic content of the air–gap magnetomotive force. Linearized models are proposed, with the aim of assessing the impact of the involved quantities on the rotor losses. General rules are found out, and they are useful in the design of machines with reduced rotor losses.

Chapter 2 provides some comparisons using finite element analysis.

Chapter 3 proposes an index of loss rotor to quickly compare different winding configurations in relation to the rotor losses induced by them.

Chapter 4 analyzes and provides measurements of rotor losses in a axial–flux motor prototype.

Multiphase systems

The employment of multiphase machines (phase number greater than 3) fed by multiphase converters can introduce an improvement in the area of medium to high power sized drives as they are characterised by a better efficiency, torque/weight and torque/volume ratio compared to three phase machines. With same voltage and power, the increase of the number of phases implies a reduction in the current per phase, thus the thermal stress on the power semiconductors is inversely proportional to the number of phases. Hence high voltages IGBT can be used with higher switching frequency without parallelisation techniques.

Fault-tolerant capability of electrical drives is an essential feature in applications such as automotive [14], aeronautic [15], and many others, where continuous operation is a mandatory option. Although less stringent, fault tolerance is a positive feature also in the industrial environment, due to the related productivity enhancement. A multi-phase PM machine exhibits a high fault-tolerant capability [16], as it can be designed to reduce the fault occurrence as well as to operate indefinitely in the presence of faults [17].

The degrees of freedom of a multiphase machine can be used to enhance the reliability of the drive, provided that electrical and mechanical fault diagnosis techniques are available. This

redundancy might be used for diagnostic purposes. In fact a multiphase machine can continue to operate in case of a phase loss, with a suitable change of power supply, resulting in a reduced torque, but keeping control capabilities.

As for diagnosis techniques for three phase electric machine, they have been extensively studied in the last years with the purpose of detecting the fault at an early state and of compensating its negative effects during scheduled maintenance in order to avoid unnecessary costs [18], [19]. A fault causes asymmetry in the machine, i.e. it produces an electrical signal signature that can be detected by non-invasive techniques based on time domain analysis, frequency analysis and time-frequency analysis. The most common technique, usually referred to as Motor Current Signature Analysis (MCSA), is based on the analysis of the harmonic spectrum of the stator current. It contains information (signature) univocally related to the presence of electrical and mechanical faults [20] and permit a quantitative analysis of faults [21].

The faults of multiphase machines are similar to those of three-phase machines, they can be grossly classified into mechanical (bearing failure), or electrical. The main electrical failures of a multiphase drive are

- Phase windings short-circuit

- Power switch open-circuit fault

- Phase open-circuit fault

Some scientific papers have investigated the effects of faults in multiphase inverter, the methods of bypassing the faulted components and the compensation techniques to increase the reliability of the drive [22], [23], [24], [25]. However a general approach and a systematic analysis of fault effects and compensation is still not available.

The second part of the thesis deals with multiphase systems.
In particular, chapter 5 introduces a five–phase motor, used in following chapters for the experimental tests. The motor is presented in relation to its behavior in case of one or two phases open.
Chapter 6 provides a comparison between two kinds of multi–phase drives, showing the advantages and disadvantages of both solutions: a double three–phase drive and a five–phase drive.
Chapter 7 deals with the study of five–phase systems behavior in case of asymmetry. The study is based on the harmonic spectrum of space vectors.
The modeling of the short circuit of some turns is addressed in Chapter 8, which presents experimental and analytical results and proposes a procedure for the diagnosis of such faults.
Finally, chapter 9 defines a diagnostic index inside a five–phase drive architecture.

CHAPTER 1

Analytical computation of rotor losses

Abstract

The aim of this chapter is to link the rotor losses to the combination of slots and poles of a PM machine. The effort is to determine a general rule to single out easily if a machine topology is suitable or not, as far as the rotor losses are concerned.

By means of a simple model of the rotor losses, the link between the rotor losses and the combination of the slots and the poles of the fractional–slot PM machines is investigated. It has been seen that:

- the rotor losses are generally confined in only one region, for example in the rotor yoke when a solid rotor is used;

- a metal cover sheet is not effective for the reduction of rotor losses in fractional–slot PM machines, especially when there are high contents of sub–harmonics;

- the single–layer winding causes an increase of MMF harmonic contents and consequently of rotor losses;

- useful indications for the choice of an advantageous combination of slots and poles are derived.

Due to the model simplicity, solutions with different number of poles and slots can be rapidly compared. Some computation examples are reported, highlighting better and worse solutions. Both double–layer and single–layer windings are considered.

A further effort is to strictly bound the rotor losses to the MMF harmonic contents, allowing a rapid estimation of the effectiveness of the considered solution.

In order to select a proper winding configuration, maps of rotor losses have been obtained.

1.1 The MMF harmonic contents

Due to the discrete position of the coils within the slots there are space harmonics in the MMF distribution. Let ν be the order of the MMF harmonic, according to $\nu = 1$ for the two–pole MMF harmonic, also called the fundamental harmonic [26]. Therefore, the order of the main harmonic is $\nu = p$, where p is the number of pole pairs. The number ν is considered without sign, differently from [26], that is, it can be only positive. The main harmonic is that harmonic whose order is the same of the number of the pole pairs p. Only this main harmonic is synchronous with respect to the rotor. Conversely, all harmonics of different order are asynchronous with the rotor. Therefore, since they cause a time–varying magnetic field, they induce currents in the rotor, causing losses.

In addition, there are not only harmonics of higher order with respect to the main harmonic, but there are also harmonics of lower order, which are called sub–harmonics. It can be demonstrated that there are sub–harmonics when the machine periodicity (given as the greater common divisor (GCD) between the number of slots and the number of pole pairs $t = GCD(Q, p)$) is lower than the number of pole pairs, Fig. 1.1 [27].
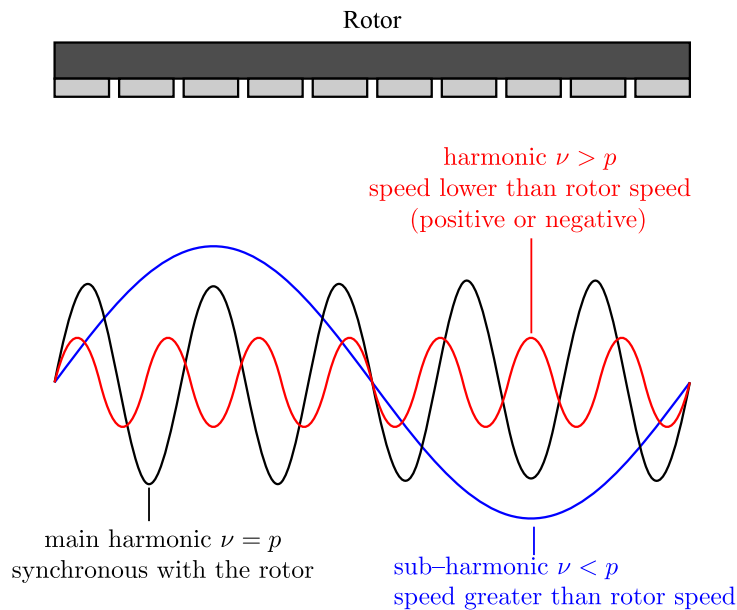
Figure 1.1: *Sketch of the MMF harmonics speed with respect to the rotor*

The sub–harmonics have a wavelength higher than the corresponding wavelength of the main harmonic. This means that the corresponding flux lines enter deeply in the rotor. In addition, the sub–harmonics have a rotation speed that is higher than the rotor speed, all the more so when the speed is backward. This implies that sub–harmonics yield higher losses in the rotor. This will be verified in the following.

The amplitude of the MMF harmonics can be computed by means of the star of slots [26], as also suggested in [27]. The MMF harmonic contents are generally shown by using bars (histograms), as shown in Fig. 1.2. This figure shows the amplitude of the MMF harmonics of a PM machine with 108 slots and 106 poles, when a double layer winding (Fig. 1.2a) and a single

layer winding (Fig. 1.2b) are adopted. The amplitudes are normalized to the amplitude of the main harmonic, highlighted with a circle on the top of the corresponding bar.

(a) *Double layer*
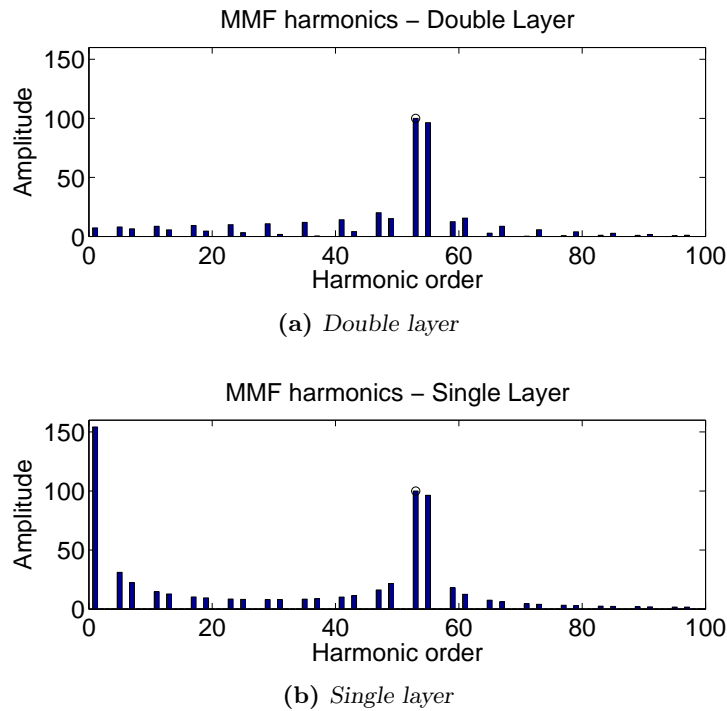
(b) *Single layer*

Figure 1.2: *Normalized MMF harmonic contents of a 108–slot 106–pole machine, with double–layer (a) and single–layer (b) winding*

By adopting a single–layer winding, the amplitude of the harmonics increases, especially of the sub–harmonics, as shown in Fig. 1.2b. Thus, it is expected that rotor losses in machines with single–layer winding are higher than rotor losses in the same machines with double–layer winding.

The MMF harmonics rotate in the air–gap with different speeds. The mechanical speed of the generic ν–th MMF harmonic in the stator reference frame can be computed as

$$\omega_{\nu s} = \frac{\omega}{sgn \cdot \nu} \tag{1.1}$$

where sgn is the sign function, and $sgn = +1$ if the ν–th harmonic rotates in the same direction of the rotor, while $sgn = -1$ if the ν–th harmonic rotates in the opposite direction.

The sign function is defined in [26]; harmonics that correspond to the values of:

$$\nu = 1 + 3k \qquad\qquad \text{with } k = 0, 1, 2, \dots \text{ positive integer} \tag{1.2}$$

have the same sign, while harmonics that correspond to the values of:

$$\nu = 2 + 3k \qquad\qquad \text{with } k = 0, 1, 2, \dots \text{ positive integer} \tag{1.3}$$

also have the same sign but opposite to that of the previous series. A positive sign is conventionally assigned to the series containing the main harmonic (that with $\nu = p$).

The speed with respect to the rotor is computed as:

$$\omega_{r\nu} = 2\pi f \left(\frac{sgn}{\nu} - \frac{1}{p} \right) \tag{1.4}$$

The rotating MMF harmonics induce in the rotor an EMF at the frequency $f_{r\nu}$. Such a frequency can be expressed as a function of the harmonic order ν as

$$f_{r\nu} = \nu \frac{\omega_{r\nu}}{2\pi} = f \left| sgn - \frac{\nu}{p} \right| \tag{1.5}$$

The MMF harmonic contents depend on the combination of the number of slots and poles of the machine, as well as the winding arrangement (in particular if the winding is single– or double–layer). As an example, Fig. 1.3a shows the harmonic contents of a 36–slot 34–pole double–layer winding. The corresponding electric loading is shown in Fig. 1.3b.
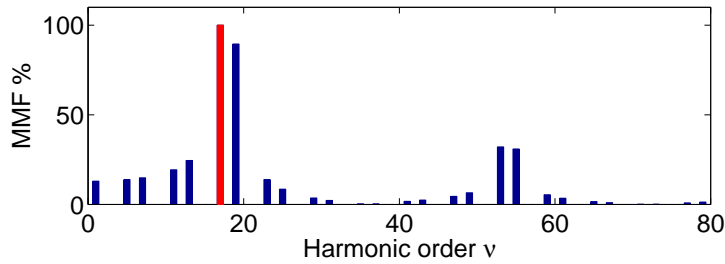
(a) *MMF harmonic contents*
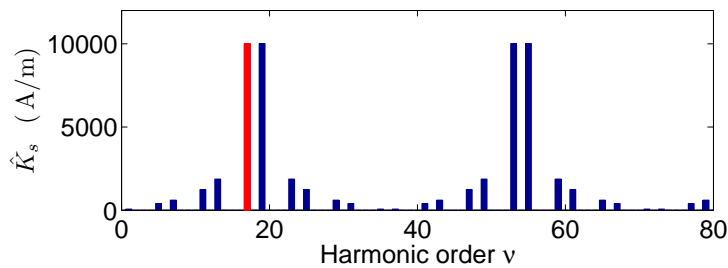
(b) *Electric loading harmonic contents*

Figure 1.3: *MMF harmonic contents (a) and electric loading harmonic contents (b) of a 36–slot 34–pole double–layer winding.*

Fig. 1.4 shows the MMF harmonics rotating speed in the rotor reference frame up to the order $\nu = 80$ (assuming a rotating machine), for the 36–slot 34–pole double–layer winding. It is worth noticing that the bars in Fig. 1.4 follow the two curves defined by $sgn = +1$ (rotation in

the same direction of the rotor) and $sgn = -1$ (rotation in the opposite direction of the rotor). It is noticed that when ν tends to infinity, the speed of the ν–th harmonic approaches $-2\pi f/p$, irrespective of whether function sgn is positive or negative.
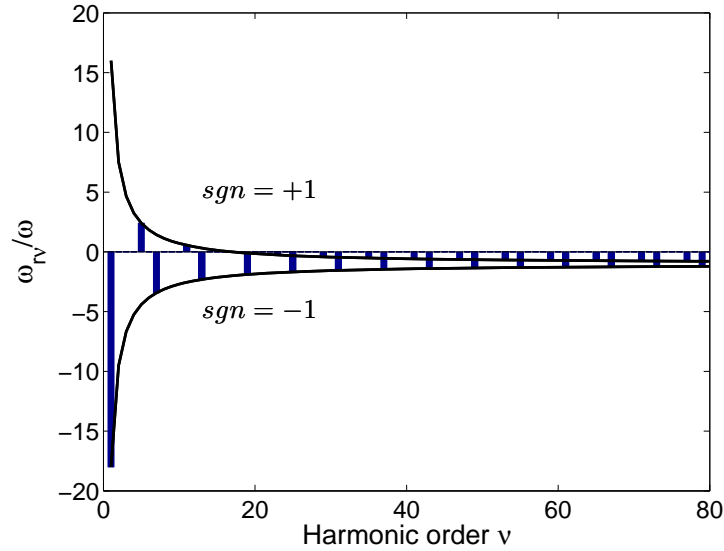
Figure 1.4: *Speed of the MMF harmonics in the rotor reference frame, for a 36–slot 34–pole double–layer winding.*

The corresponding representation of the frequency induced in the rotor is shown in Fig. 1.5.
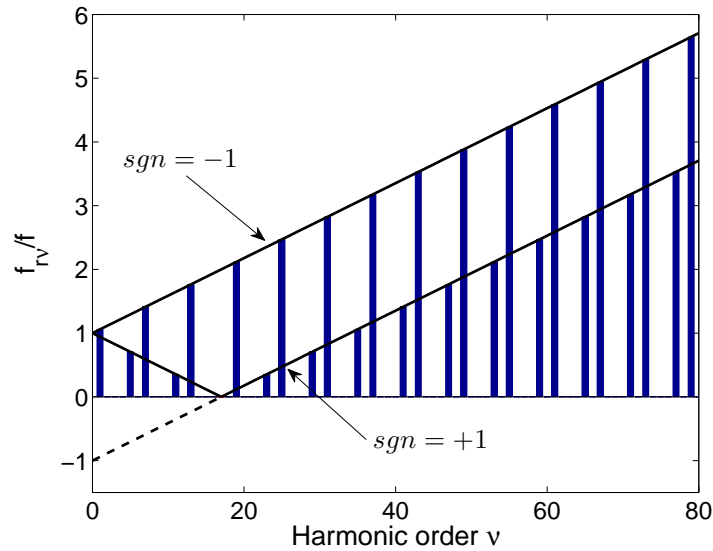
Figure 1.5: *Rotor induced frequency of a 36–slot 34–pole double–layer winding.*

Depending on the sign of the function sgn, two curves can be identified to interpolate the

frequency values, as also reported in Fig. 1.5. The figure gives also a rapid rule to easily find out the rotor frequency behaviour: the $f-$axis intersection corresponds to the frequency f, the $\nu-$axis intersection to the pole pairs p and the straight lines slope is f/p. The parameters f and ν are then linked together, depending on the winding configuration.

1.2 Analytical straight–lined models

Among the several models proposed for the study of rotor losses, the analytical models are preferred to finite elements (FE) models, which are generally time–consuming. In fact, although the analytical models are based on a simplified geometry, they are very flexible to compare rapidly different machine topologies, that is, different combinations of slots and poles.

The analytical approach is based on the solution of Maxwell equations in a two–dimensional space. The solution of Maxwell equations can be carried out taking into account a cylindrical geometry [4, 28]. The solution consists of a series of Bessel equations, that are approximated by series.

Hereafter, a straight–lined model is preferred. This models are often characterized by four or five layers of different materials [9, 11].

Vector magnetic potential results to be expressed as a series of hyperbolic sines and cosines. Three models are described hereafter considering one, two and four layers; differences in using either of them will be discussed.

The one–layer straight–lined model

Let's start from a straight–lined model characterized by one conductive layer. It is adopted for obtaining some useful considerations about the impact of some quantities (such as the frequency, the electric loading, the materials, the dimensions) on rotor losses.

Since the losses are often concentrated (and confined) in one layer only, a model with only one or two layers could be enough to predict the losses of the machine.

Magnetic Field Analysis

A medium of height y_m and infinite depth is considered, as shown in Fig. 1.6. The medium is characterized by an electrical conductivity σ and a magnetic permeability μ. Although the border effects are neglected, the reference length is L_x. In a rotating machine L_x corresponds to the circumference πD where D is the stator inner diameter.

A linear current density $K_{s\nu}(x)$ with amplitude $\hat{K}_{s\nu}$ and wavelength $\tau_\nu = L_x/(2\nu)$ is imposed along the lower surface of the medium (i.e., at $y = 0$). The parameter ν indicates the number of wavelengths contained in the reference length L_x. The waveform moves at the speed $v_{nu} = \omega_{r\nu}L_x/(2\pi)$. The linear current density expressed using the complex notation is

$$\dot{\mathbf{K}}_{s\nu}(x) = \hat{K}_{s\nu}e^{\jmath\pi x/\tau_\nu} \tag{1.6}$$

From Maxwell's equations, the field problem is expressed by means of the magnetic vector potential $\dot{\mathbf{A}}$. Current density and magnetic vector potential have only the z component, so that
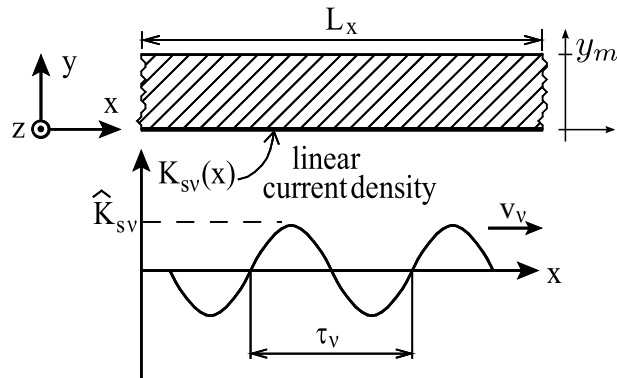
Figure 1.6: *Straight–lined model with one layer*

the field problem can be expressed as

$$\frac{\partial^2 \dot{A}_z(x,y)}{\partial x^2} + \frac{\partial^2 \dot{A}_z(x,y)}{\partial y^2} - \jmath 2\pi f_{r\nu}\mu_0\sigma \dot{A}_z(x,y) = 0 \tag{1.7}$$

Such a field problem can be solved by means of the separation of variables, and assigning the following boundary conditions: (**i**) along the lower surface of the medium, at $y = 0$, the tangential magnetic field is fixed to be equal to the imposed linear current density, as

$$\dot{\mathbf{H}}_x(x,0) = \dot{\mathbf{K}}_{s\nu}(x) \tag{1.8}$$

then, (**ii**) the vector magnetic potential approaches zero when y increases. Finally the vector magnetic potential results in

$$\dot{A}_z(x,y) = -\frac{\mu \hat{K}_{s\nu}}{\dot{d}}\, e^{\jmath \frac{\pi}{\tau_\nu}x}\, e^{-\dot{d}y} \tag{1.9}$$

where

$$\dot{d} = \sqrt{\left(\frac{\pi}{\tau_\nu}\right)^2 + \jmath 2\pi f_{r\nu}\mu\sigma} \tag{1.10}$$

Computation of the losses

The power loss density in the medium is given by

$$q = 2\sigma\pi^2 f_{r\nu}^2 \int_0^{y_g} \dot{A}\dot{A}^* dy \tag{1.11}$$

where $\dot{A}^*$ means the complex conjugate of $\dot{A}$. The power loss density (1.11) can be rearranged as

$$q = \frac{\xi^4}{\sqrt[4]{(\pi^4 + \xi^4)^3}} \frac{1}{\cos(\varphi/2)} \frac{\hat{K}_{s\nu}^2}{4\sigma\tau_\nu} k_{ym} \tag{1.12}$$

where ξ is defined as the specific wavelength, given by

$$\xi = \sqrt{2}\frac{\tau_\nu}{\delta} \tag{1.13}$$

defining δ as the penetration thickness as $\delta = 1/\sqrt{\pi f_{r\nu}\mu\sigma}$; then the angle φ can be defined by $\tan\varphi = (\xi/\pi)^2$. Finally,

$$k_{ym} = 1 - e^{-2\sqrt[4]{\pi^4 + \xi^4}\cos(\varphi/2)y_m/\tau_\nu} \tag{1.14}$$

represents a reduction factor of the power loss density. It decreases as the wavelength τ_ν decreases with respect to the height of the medium y_m (see Fig. 1.7). It is verified that this factor is different from the unity only for harmonic of low order and for low values of ξ, and only with low values of y_m, too. This simplified model allows an easy interpretation of the induced losses phenomenon, highlighting the impact on the losses of the following variables: frequency $f_{r\nu}$, harmonic order ν, conductivity σ, and permeability μ.
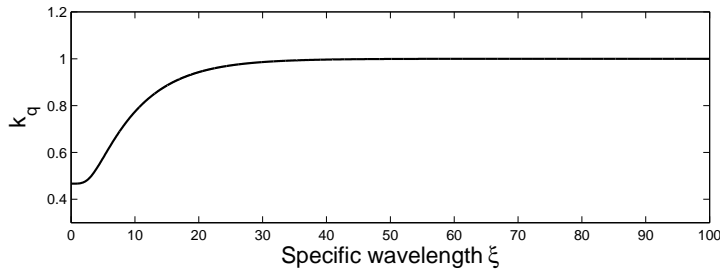
Figure 1.7: *Behavior of k_{ym} versus ξ for $\nu = 1$ and $y_m = 5mm$*

Fig. 1.8a shows the behavior of $\cos(\varphi/2)$ versus the specific wavelength ξ.

(a)

(b)

(c) *Detailed view of $f_{1\xi}$*
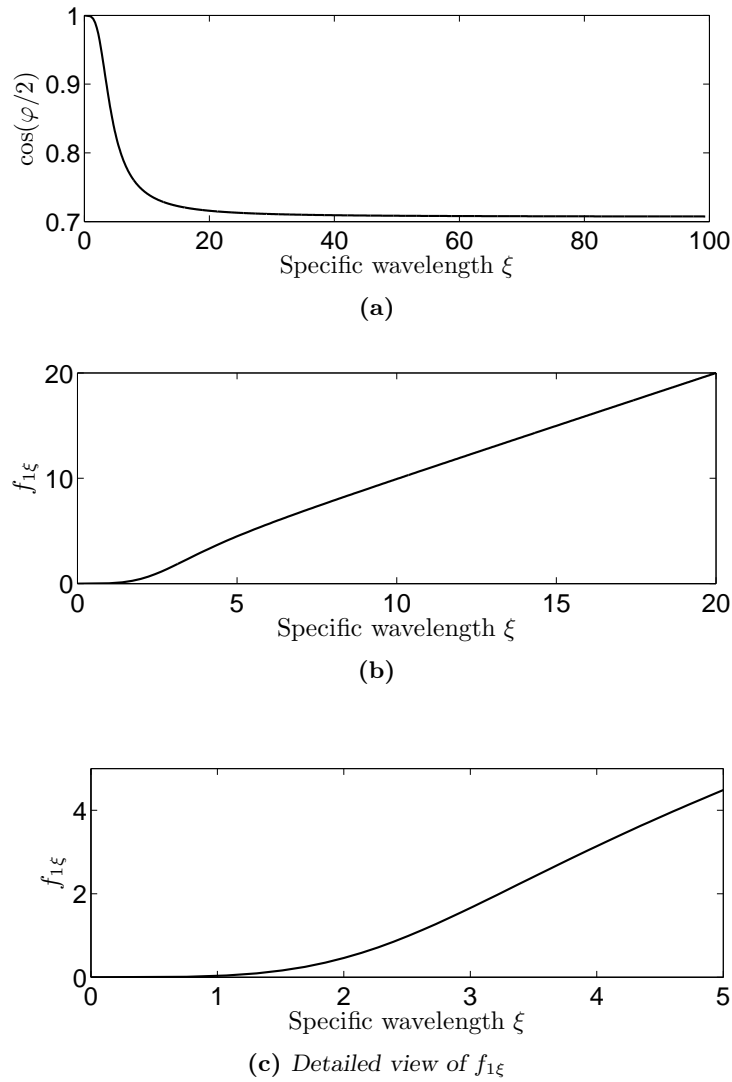
Figure 1.8: *Behavior of $\cos(\varphi/2)$ (a) and of $f_{1\xi} = \frac{\xi^4}{\sqrt[4]{(\pi^4+\xi^4)^3}}$ (b) versus ξ*

It decreases when ξ increases, ranging between $1/\sqrt{2}$ and 1. For this reason, $\cos(\varphi/2)$ exhibits a minimum impact on power loss density.

Fig. 1.8b shows the behavior of the first factor of (1.12) $\left(f_{1\xi} = \frac{\xi^4}{\sqrt[4]{(\pi^4+\xi^4)^3}}\right)$, labeled $f_{1\xi}$, versus the specific wavelength ξ, so as to emphasize the influence of ξ on the power loss density. For low ξ, function $f_{1\xi}$ is low as well, and it tends to zero when ξ approaches zero. Therefore, the power loss density can be neglected for low values of ξ, e.g. for $\xi < 1$ (see Fig. 1.8c). When ξ increases, the function increases, approaching the straight line $f_{1\xi} = \xi$.

Impact of the harmonic order

For a given harmonic order, the specific wavelength ξ can be rewritten as

$$\xi = k_\xi \frac{\sqrt{f_{r\nu}}}{\nu} \tag{1.15}$$

where $k_\xi = L_x \sqrt{\pi\mu\sigma/2}$ is constant for a given machine and $f_{r\nu}$ is computed from (1.5).

It can be observed that lower the harmonic order ν, higher the ratio $\sqrt{f_{r\nu}}/\nu$ i.e., ξ. In fact, remember that the frequency $f_{r\nu}$ is linked to the harmonic order (equation (1.5) and Fig. 1.5).

Since ξ contains information about both the frequency and the harmonic order, it is enough to understand their impact on the losses.

Fig. 1.9 shows ξ as a function of the harmonic order ν, for the machine with 36–slot 34–pole winding. Two curves are drawn according to the function sgn is positive or negative.

(i) When $sgn = -1$, the specific wavelength ξ decreases monotonically with the harmonic order ν (i.e. with the increasing frequency, see Fig. 1.5).

(ii) When $sgn = +1$, ξ decreases monotonically for $\nu < p$ (the frequency decreases towards zero), becoming equal to zero in correspondence of the number of pole pairs p at $\nu = p$ (e.g. $\nu = 17$ according to the 36–slot 34–pole). In fact, the waveform of order $\nu = p$ is the main harmonic that is synchronous with the rotor and induces no rotor currents. Then, for $\nu > p$ (the frequency increases), ξ increases up to a maximum that arises at $\nu = 2p$ and then it decreases again. Such maximum of ξ is $k_\xi \sqrt{f}/(2p)$.
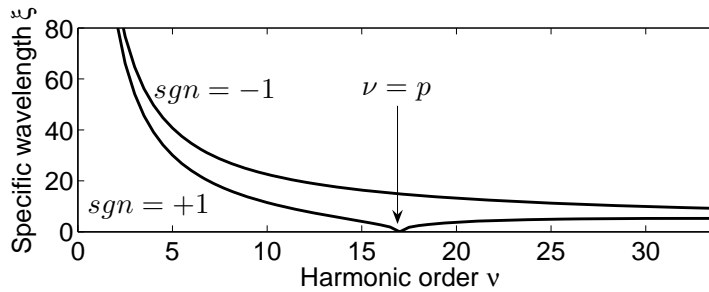
Figure 1.9: *Specific wavelength ξ as a function of harmonic order ν for the 36–slot 34–pole winding*

Fig. 1.9 shows that ξ decreases when ν increases, and high values of ξ occur for low values of ν. This is carried out for a particular winding configuration, nevertheless it is a general result.

Fig. 1.10 shows the power loss density versus the frequency square root. The figure highlights the difference between the various harmonic orders.

Thus, the MMF sub–harmonics generally might induce higher rotor losses than MMF harmonics of higher order.
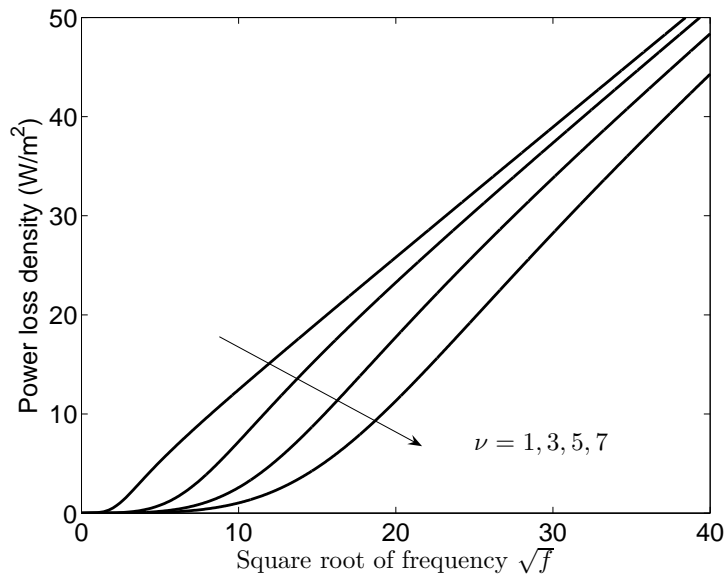
Figure 1.10: *Power loss density as a function of the frequency square root*
$\sqrt{f_{r\nu}}$, *for different harmonic orders*

Impact of the electric loading harmonics

The electric loading harmonics are characterized by the amplitude $\hat{K}_{s\nu}$, which vary with the winding arrangement. They have a strong influence on the power loss density since $\hat{K}_{s\nu}$ appears with power of two in (1.12).

So, losses depend upon $\hat{K}_{s\nu}^2$, or, in other words, upon $k_{w\nu}^2$. The impact of a particular harmonic on the losses has to be weighed with its corresponding winding factor. Therefore, even if low order harmonics present high value of ξ, the corresponding power loss density is not necessarily higher.

For the computation of the power loss density, it is important not only to get the specific wavelength ξ, corresponding to a given harmonic order ν, but also to compute the amplitude of the electric loading harmonic of the same order.

According to this consideration, in a fractional–slot machine, the harmonics close to the main harmonic (i.e of order $\nu \approx p$), and multiple of it, are characterized by a electric loading amplitude equal to the main harmonic electric loading amplitude. For instance, see Fig. 1.3b. In other words, the winding factor of order ν is $k_{w\nu} \simeq 1$ around of $\nu = p$. These harmonics can cause high rotor losses, all the more if they are characterized by a backward speed (i.e. $sgn = -1$).

Effect of the material

The materials and the dimensions influence the power loss density. Figs. 1.11, 1.12 and 1.13 show the impact of different materials on power loss density.
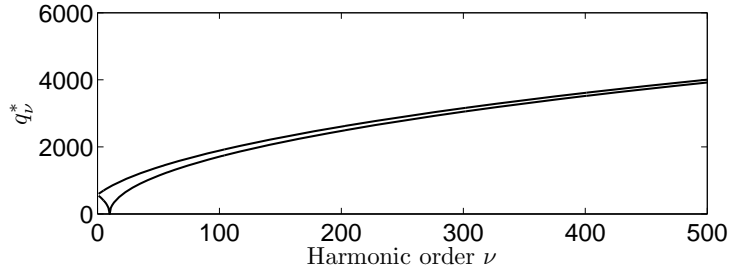
Figure 1.11: $q^*(\nu) = \frac{\xi^4}{\sqrt[4]{(\pi^4 + \xi^4)^3}} \nu$ *for iron*
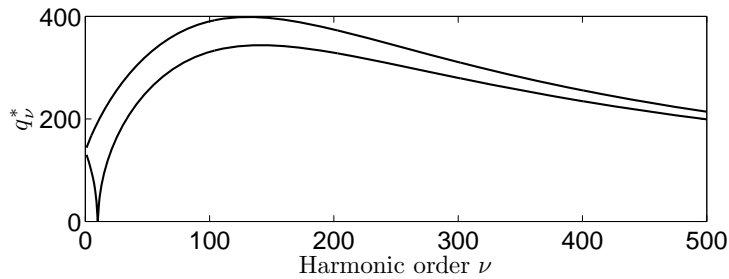
Figure 1.12: $q^*(\nu) = \frac{\xi^4}{\sqrt[4]{(\pi^4 + \xi^4)^3}} \nu$ *for copper*
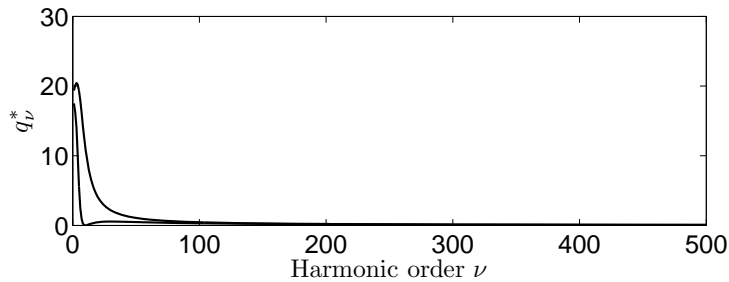
Figure 1.13: $q^*(\nu) = \frac{\xi^4}{\sqrt[4]{(\pi^4 + \xi^4)^3}} \nu$ *for magnet*

Since many terms are constant, a normalized power loss density

$$q^*(\nu) = \frac{\xi^4 \nu}{\sqrt[4]{(\pi^4 + \xi^4)^3}} \tag{1.16}$$

has been used. In the comparisons, the number of pole pairs is fixed to $p = 17$, the speed to $n = 100$ rpm and the machine diameter to $D = 1$ m.
The material characteristics are shown in Table 1.1:

Table 1.1: *Material characteristics used for computations*

1)	iron	$\mu = 100\mu_0$	$\sigma = 10$ MS/m
2)	copper	$\mu = \mu_0$	$\sigma = 58$ MS/m
3)	magnet	$\mu = 1.05\mu_0$	$\sigma = 1$ MS/m

A constant permeability is also adopted for iron, considering that rotor iron is mainly saturated by the PM flux and then by the flux due to the main harmonic of stator current distribution, which is synchronous with the rotor. The phenomenon of the rotor losses is due to harmonics that are not synchronous with the rotor, which are parasitic harmonics.

Besides the amplitude variation of the power losses according to the different material, it is worth noticing that the maximum of the power loss density is achieved at different harmonic orders. Considering iron (e.g. a solid rotor), higher loss density is caused by harmonic of order higher than 500. Considering copper, higher loss density is caused by harmonic of order close to 100. Finally, considering the permanent magnet, higher loss density is induced by the sub–harmonics.

Effect of the machine dimension

Considering the impact of dimensions, it can be noticed that the impact of the harmonic order on the power loss density changes. This is reasonable because the pole pitch τ_ν is a function of D.

In the following comparison, material properties, winding configuration, and electric current density are fixed. Only the machine diameter is changed. Fig. 1.14 shows that not only the power loss density increases when the diameter increases, but also the maximum is found at different harmonic orders: the higher the machine diameter, the higher the harmonic order.
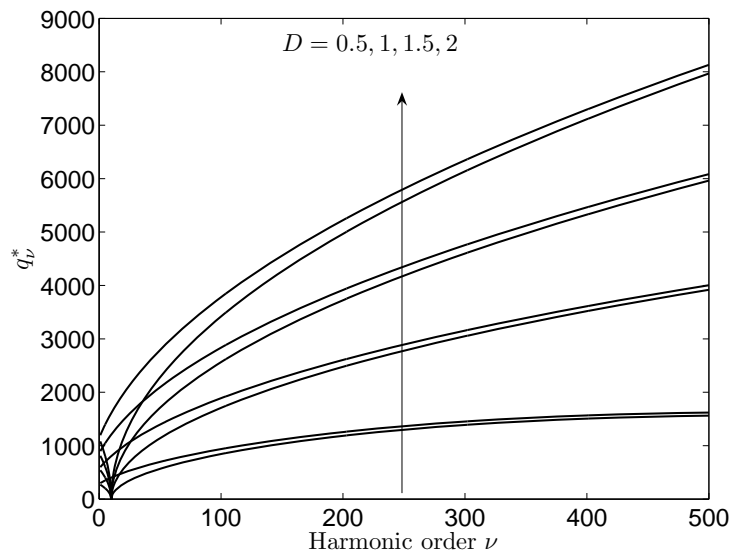
Figure 1.14: $q^*(\nu) = \dfrac{\xi^4}{\sqrt[4]{(\pi^4 + \xi^4)^3}}\nu$ *for iron, with different diameters D (m)*

Comments to the results

The identification of the harmonic order that causes the highest power loss density is not immediate. There is a sort of compensation between the increase of ν and the decrease of ξ. The identification of the harmonic inducing the maximum power loss density is not immediate. However, the higher contribution to the rotor losses is due to two groups of harmonics: the sub–harmonics and the slot harmonics.

The sub–harmonics are harmonics of order $\nu < p$. They may induce high rotor losses since they are characterised by a low harmonic order ν, that is, by a high specific length ξ, as shown in Fig. 1.9.

By definition, the slot harmonics are those harmonics characterised by a winding factor $k_{w\nu}$ equal to the winding factor of the main harmonic k_w, [26, 29]. Although this definition is extensively dealt with in technical literature for integral–slot windings, there is no information about the fractional–slot windings. Using the theory of the star of slot [26, 27], it is possible to demonstrate that in a fractional–slot winding the harmonic orders of the slot harmonics are given by $\nu = kQ \pm p$, where $k = 1, 2, 3, ...$ is an integer number.

Among all the slot harmonics the first one has the worst impact. It is the closest to the main harmonic (e.g. of order $\nu = 19$ in Fig. 1.3b). Although its specific length ξ is not high, the amplitude of its electric loading is equal to the amplitude of the main harmonic. Thus, the rotor losses that it induces are high. Conversely, the slot harmonics of higher order are characterised by a high electric loading amplitude, however their contribution to the rotor losses is moderate because of the decreasing of the specific wavelength ξ with the harmonic order ν.

The two–layers straight–lined model

In the following, a straight–lined two–dimensional model with two layers is adopted, as shown in Fig. 1.15. A air–gap region is added in order to determine its impact on rotor losses.
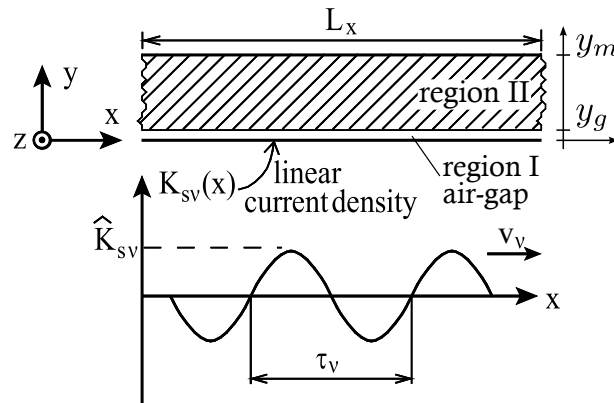
Figure 1.15: *Straight–lined model with two layers.*

Magnetic field analysis

This model considers a medium of height $y_m - y_g$, an air–gap of thickness y_g, both with infinite depth. Although the border effects are neglected, the reference length is L_x. The medium is characterized by an electrical conductivity σ and a magnetic permeability μ.

A linear current density $K_s(x)$ characterized by a direction along the z–axis, an amplitude $\hat{K}_s$ and a wavelength $\tau_\nu = L_x/(2\nu)$ is imposed along the lower surface of the air–gap, at $y = 0$. The parameter ν indicates the number of wavelengths contained in the reference length L_x. The waveform moves at the speed $v_\nu = \omega L_x/(2\pi)$. The linear current density expressed using the complex notation is

$$\dot{\mathbf{K}}_s(x) = \hat{K}_s e^{\jmath \pi x/\tau_\nu} \tag{1.17}$$

By adopting Maxwell's equations, the field problem is formulated using the magnetic vector potential $\dot{\mathbf{A}}$. In region I, the air–gap, (i.e. for $0 \le y \le y_g$), it is

$$\nabla^2 \dot{\mathbf{A}}^I = 0 \tag{1.18}$$

and in region II, (i.e. for $y_g \le y \le y_m$), it is

$$\nabla^2 \dot{\mathbf{A}}^{II} - \jmath \omega \mu \sigma \dot{\mathbf{A}}^{II} = 0 \tag{1.19}$$

The power losses are confined in region II. They depend on (**i**) the frequency, (**ii**) the harmonic order, (**iii**) the wavelength τ_ν (i.e. on the harmonic order ν), (**iv**) the linear current density, and (**v**) the conductivity and permeability of the materials.

Effect of the air–gap

Fig. 1.16 shows the power loss density, versus the specific wavelength ξ, for different values of harmonic order, i.e. $\nu = 1, 3, 5, 7$ for given air–gap thickness $y_g = 1$ mm. So, for each curve, the parameter ξ yields information about the frequency and characteristics of the materials, being the harmonic order ν fixed.

For a given ξ, the power loss density increases rapidly when the harmonic order ν increases. For the purpose to limit the power loss density, it is essential that ξ becomes lower and lower as ν increases. In the following, it will be shown that this condition is verified in the MMF harmonics of electrical machines.

Fig. 1.17 shows the power loss density for a wide range of air–gap thickness.

When ν is low (e.g. $\nu = 1$), the increase of the air–gap yields a negligible impact on the power loss density. On the contrary, the impact is visible for higher values of ν.

Thus, the effect of the air–gap is to reduce the impact of high–order harmonics on the rotor losses. In other words, it can be considered that the effect of the air–gap is that of a "low pass filter" for the MMF harmonics.
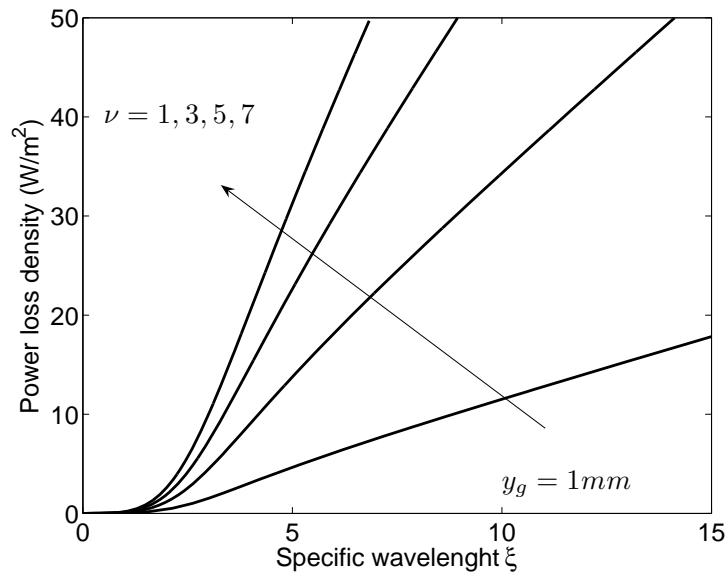
Figure 1.16: *Power loss density as a function of ξ, for different values of ν, with $y_g = 1mm$*
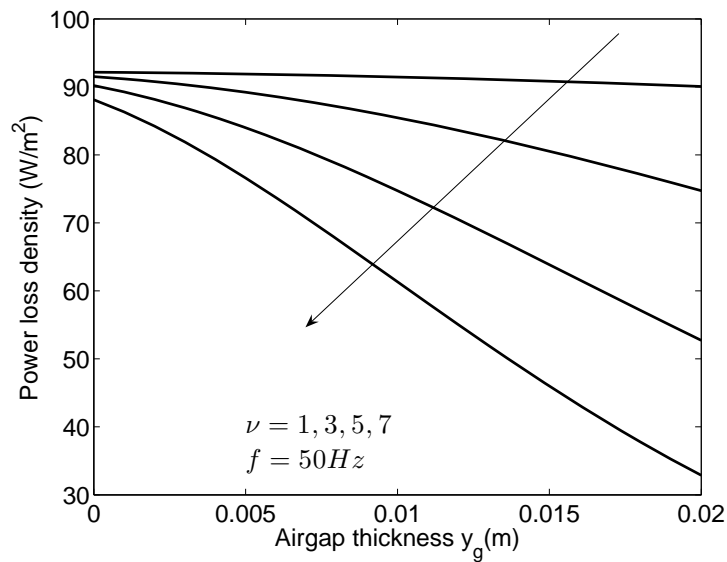
Figure 1.17: *Power loss density as a function of y_g, for different ν, with $f = 50Hz$*

Examples

Some examples are reported hereafter, referring to some combinations of number of slots and poles. For all comparisons, the linear current density is fixed to be equal to 10 kA/m, and the machine speed to 100 r/min. The straight–lined model with two layers has been adopted. A reference diameter equal to $D = 0.5$ m has been considered.

First example

Fig. 1.18 shows the power loss density due to the various harmonics in a 36–slot 34–pole surface–mounted permanent magnet machine, with an air–gap thickness $y_g = 2$ mm. The material considered in the model is Neodymium Iron Boron (that represents the permanent magnet). The MMF and linear current density harmonics are shown in Fig. 1.3a and Fig. 1.3a respectively.
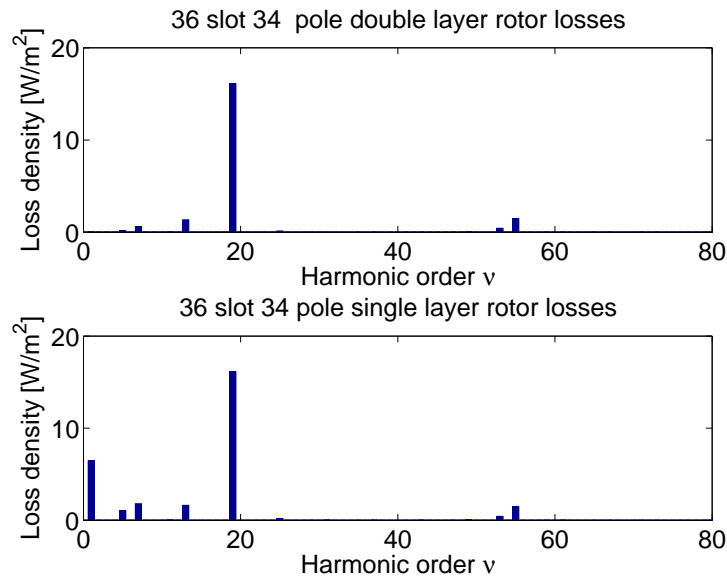
Figure 1.18: *36–slot 34–pole machine: power loss density with $y_g = 2$ mm for magnetic material.*

Fig. 1.18 shows that the MMF harmonic causing the higher power loss is that of order $\nu = 19$. It is characterized by the same winding factor of the main harmonic ($\nu = p = 17$), so that the electric loading squared $\hat{K}_s^2$ assumes a high value as well as the corresponding losses.

On the contrary, the sub–harmonics are characterized by a low winding factor. Thus, even if the low–order harmonics yield a high specific wavelength ξ (see Fig. 1.9), which involves higher power loss density (see Fig. 1.16), such harmonics are characterized by a low electric loading squared $\hat{K}_s^2$. Thus their contribution to the power loss is limited.

At last, as expected, the single–layer winding machine yields higher power losses with respect to the double–layer winding machine. In particular, the sub–harmonic increases when the single–layer is adopted.

Second example

A similar result is achieved with a surface–mounted permanent magnet machine with 51 slots and 28 poles. The harmonics of the linear current density are shown in Fig. 1.19. With this combination of slots and poles, the harmonics with a high winding factor are all multiples of the main harmonic.
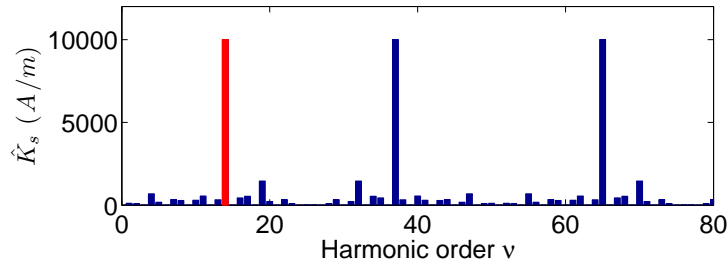
Figure 1.19: *51–slot 28–pole machine: electric loading*

Fig. 1.20 shows the power loss density, achieved in the permanent magnet, with an air–gap thickness $y_g = 1$ mm. The harmonic of order $\nu = 37$ (it is a slot harmonic) induces the higher losses, while the sub–harmonics, which are characterized by a low winding factor, induce limited losses, even though not negligible.
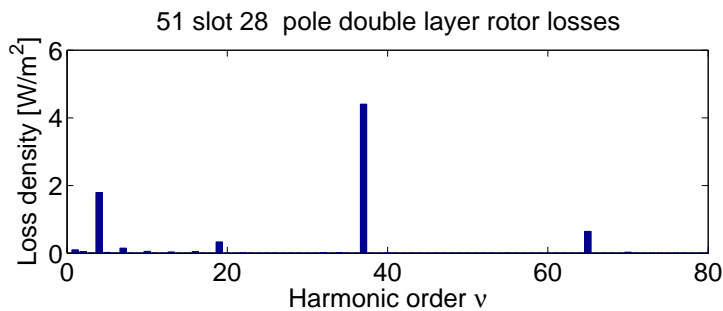
Figure 1.20: *51–slot 28–pole machine: power loss density with $y_g = 1$ mm for magnetic material.*

Impact of the air–gap

As seen before, the impact of the air–gap is to reduce the influence of the MMF harmonics of higher order. Thus, in a machine with a larger air–gap, it is expected a decrease of the power loss density for any harmonic order, especially for the harmonics of high order.

Fig. 1.21 and Fig. 1.22 show the power loss density versus the harmonic order. Increasing the air–gap from $y_g = 1$ mm to $y_g = 2$ mm, the losses decrease greatly: they become almost one third in the second case. The contribution of the sub–harmonics is almost the same. In this model, iron is considered so as to emphasize the effect of the variation of the air–gap, however the same effect is observed with a different material.
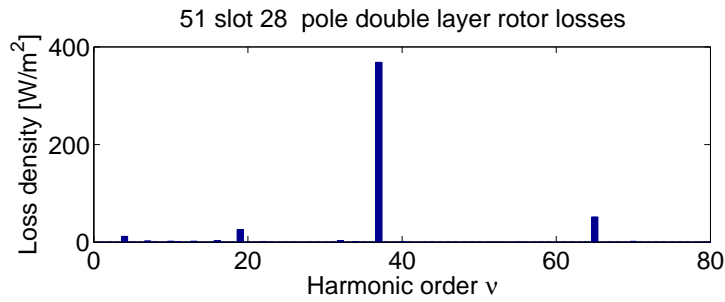
Figure 1.21: *51–slot 28–pole machine: power loss density $y_g = 1$ mm for iron*
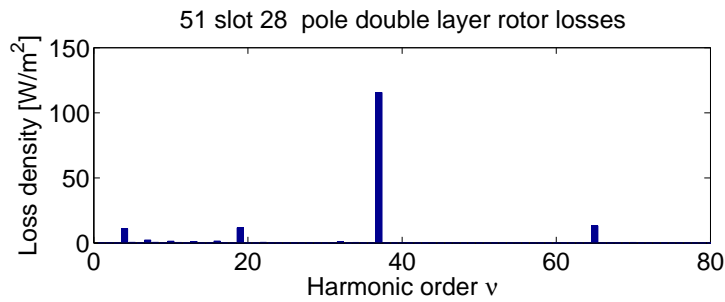
Figure 1.22: *51–slot 28–pole machine: power loss density $y_g = 2$ mm for iron*

The four–layers straight–lined model

The geometry shown in Fig. 1.23 is used. It is characterised by four laid upon layers. This model is useful for analyzing the effect of a current sheet on the surface of a multiple layers solid.
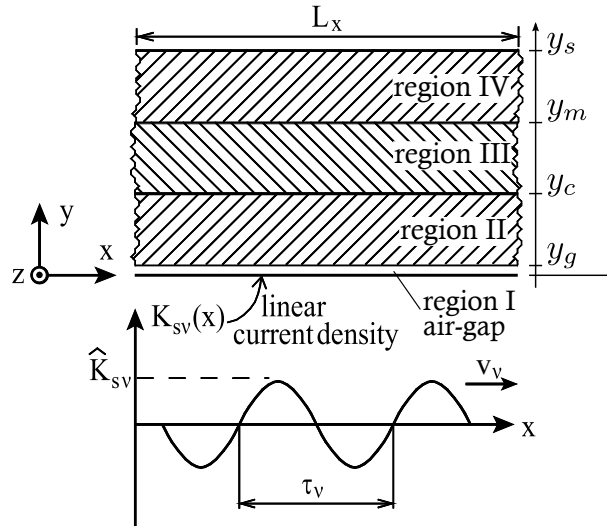
Figure 1.23: *Straight–lined model with four layers*

It is verified that losses are mainly concentrated on one layer only, so that the achieved results could be obtained with a one or two layer model as well.

Magnetic field analysis

The four regions here considered are the airgap (region I), the copper region (region II), the magnets region (region III), and the steel region (region IV). The analysis is carried out using Maxwell's equations. The source is assumed to be a linear current density at $y = 0$ given by:

$$\dot{\mathbf{K}}_s(x) = \hat{K}_s e^{\jmath \pi x / \tau_\nu}$$

Maxwell's equations for each region can be formulated using the magnetic vector potential $\dot{\mathbf{A}}$:

$$\nabla^2 \dot{\mathbf{A}} - \jmath \omega \mu_0 \sigma \dot{\mathbf{A}} = 0$$

in particular, in the airgap region (region I, $0 \leq y \leq y_g$), the equation results in:

$$\nabla^2 \dot{\mathbf{A}}^I = 0$$

in the copper region (region II, $y_g \leq y \leq y_c$):

$$\nabla^2 \dot{\mathbf{A}}^{II} - \jmath \omega \mu_0 \sigma^{II} \dot{\mathbf{A}}^{II} = 0$$

in the magnets region (region III, $y_c \leq y \leq y_m$):

$$\nabla^2 \dot{\mathbf{A}}^{III} - \jmath \omega \mu_0 \sigma^{III} \dot{\mathbf{A}}^{III} = 0$$

in the steel region (region IV, $y_m \leq y \leq y_s$):

$$\nabla^2 \dot{\mathbf{A}}^{IV} - \jmath \omega \mu_0 \mu_{rs} \sigma^{IV} \dot{\mathbf{A}}^{IV} = 0$$

These equations can be resolved by means of variables separation method, that is considering the magnetic vector potential $\dot{\mathbf{A}}$ to be the product of two functions, $\dot{\mathbf{X}}(x)$ and $\dot{\mathbf{Y}}(y)$:

$$\dot{\mathbf{A}}(x, y) = \dot{\mathbf{X}}(x) \dot{\mathbf{Y}}(y)$$

Moreover, according to the symmetry of the model, currents have only the z component. Therefore the magnetic vector potential will have only the z component as well:

$$\dot{\mathbf{A}}(x, y) = \dot{A}_z(x, y) \mathbf{u_z}$$

The equation becomes:

$$\frac{\partial^2 \dot{A}_z(x,y)}{\partial x^2} + \frac{\partial^2 \dot{A}_z(x,y)}{\partial y^2} - \jmath\omega\mu_0\sigma\dot{A}_z(x,y) = 0$$

Considering $\dot{A}_z(x,y) = \dot{X}(x)\dot{Y}(y)$ it is:

$$\dot{Y}(y)\frac{\partial^2 \dot{X}(x)}{\partial x^2} + \dot{X}(x)\frac{\partial^2 \dot{Y}(y)}{\partial y^2} - \jmath\omega\mu_0\sigma\dot{X}(x)\dot{Y}(y) = 0$$

$$\frac{1}{\dot{X}(x)}\frac{\partial^2 \dot{X}(x)}{\partial x^2} + \frac{1}{\dot{Y}(y)}\frac{\partial^2 \dot{Y}(y)}{\partial y^2} - \jmath\omega\mu_0\sigma = 0$$

Now let's replace $\jmath\omega\mu_0\sigma$ with $\dot{a}^2$; then:

$$\frac{1}{\dot{X}(x)}\frac{\partial^2 \dot{X}(x)}{\partial x^2} = -\dot{c}^2$$

and

$$\frac{1}{\dot{Y}(y)}\frac{\partial^2 \dot{Y}(y)}{\partial y^2} - \dot{a}^2 = \dot{c}^2$$

The partial differential equation solution of (1.2) corresponds to solve the following system:

$$\begin{cases} \dfrac{1}{\dot{X}(x)}\dfrac{\partial^2 \dot{X}(x)}{\partial x^2} + \dot{c}^2 & = 0 \\[2ex] \dfrac{1}{\dot{Y}(y)}\dfrac{\partial^2 \dot{Y}(y)}{\partial y^2} - (\dot{c}^2 + \dot{a}^2) & = 0 \end{cases}$$

For the first equation, the general solution, is:

$$\dot{X}(x) = (\dot{c}_1 e^{\jmath\dot{c}x} + \dot{c}_2 e^{-\jmath\dot{c}x})$$

and for the second equation the general solution is:

$$\dot{Y}(y) = \dot{c}_3 e^{\dot{d}y} + \dot{c}_4 e^{-\dot{d}y}$$

where $\dot{d} = \sqrt{\dot{c}^2 + \dot{a}^2}$ and $\dot{c}_1, \dot{c}_2, \dot{c}_3, \dot{c}_4$ are complex coefficients. For each region these general solutions can be used, except for the airgap region, where $\dot{d}^2 = \dot{c}^2$. The aim is to determine the

complex coefficients of the magnetic vector potential for all the regions.

It's worth to observe that the forcing term on the x axis is represented by the linear current density, and for all regions this term influences the trend on x axis. Infact, in the first region, the airgap, it is:

$$\dot{A}_z^I(x,y) = (\dot{c}_1^I e^{\jmath \dot{c}^I x} + \dot{c}_2^I e^{-\jmath \dot{c}^I x})(\dot{c}_3^I e^{\dot{d}^I y} + \dot{c}_4^I e^{-\dot{d}^I y})$$

In order to determine the coefficients, some boundary conditions have to be fixed. Along the surface at $y = 0$, where the linear current density flows, it is:

$$\dot{\mathbf{H}}_t^I(x,0) = \dot{\mathbf{K}}_\mathbf{s}(x)$$

or:

$$\frac{1}{\mu^I} \left. \frac{\partial \dot{A}_z^I(x,y)}{\partial y} \right|_{y=0} = \hat{K}_s e^{\jmath \pi x / \tau_\nu}$$

$$\frac{1}{\mu^I} \dot{X}(x) \dot{c}^I (\dot{c}_3^I - \dot{c}_4^I) = \hat{K}_s e^{\jmath \pi x / \tau_\nu}$$

Equating the two members term by term, on the left and on the right of equation (1.2),

$$(\dot{c}_1^I e^{\jmath \dot{c}^I x} + \dot{c}_2^I e^{-\jmath \dot{c}^I x}) = e^{\jmath \pi x / \tau_\nu}$$

So the unknown coefficients are:

$$\begin{cases} \dot{c}^I &= \frac{\pi}{\tau_\nu} \\ \dot{c}_1^I &= 1 \\ \dot{c}_2^I &= 0 \\ \dot{d}^I &= \dot{c}^I = \frac{\pi}{\tau_\nu} \end{cases}$$

As for the $\dot{X}(x)$ function, it can be assumed that for all regions it is the same; thus it can be assumed that:

$$\begin{cases} \dot{c}_1^I &= \dot{c}_1^{II} &= \dot{c}_1^{III} &= \dot{c}_1^{IV} &= 1 \\ \dot{c}_2^I &= \dot{c}_2^{II} &= \dot{c}_2^{III} &= \dot{c}_2^{IV} &= 0 \end{cases}$$

and $\dot{c}^I = \dot{c}^{II} = \dot{c}^{III} = \dot{c}^{IV} = \frac{\pi}{\tau_\nu}$. Equating the other coefficients of equation (1.2) it is:

$$\frac{1}{\mu^I} \dot{c}^I (\dot{c}_3^I - \dot{c}_4^I) = \hat{K}_s$$

so that the relation between the coefficients $\dot{c}_3^I$ and $\dot{c}_4^I$ is:

$$\boxed{\dot{c}_3^I - \dot{c}_4^I = \mu^I \frac{\tau_\nu}{\pi} \hat{K}_s}$$

Then the vector magnetic potential in region I is:

$$\dot{A}_z^I(x,y) = e^{\jmath \pi x / \tau_\nu}(\dot{c}_3^I \, e^{\pi y \tau_\nu} + \dot{c}_4^I \, e^{-\pi y / \tau_\nu})$$

Now let's consider the vector magnetic potential in region II, $\dot{A}_z^{II}(x,y)$, that is expressed as:

$$\dot{A}_z^{II}(x,y) = (\dot{c}_1^{II} e^{\jmath \dot{c}^{II} x} + \dot{c}_2^{II} e^{-\jmath \dot{c}^{II} x})(\dot{c}_3^{II} \, e^{\dot{d}^{II} y} + \dot{c}_4^{II} \, e^{-\dot{d}^{II} y})$$

or

$$\dot{A}_z^{II}(x,y) = e^{\jmath \pi x / \tau_\nu}(\dot{c}_3^{II} \, e^{\dot{d}^{II} y} + \dot{c}_4^{II} \, e^{-\dot{d}^{II} y})$$

The boundary conditions at the border between region I and region II, at $y = y_g$, yield:

$$\begin{cases} \dot{\mathbf{H}}_t^I(x, y_g) = \dot{\mathbf{H}}_t^{II}(x, y_g) \\ \dot{\mathbf{B}}_n^I(x, y_g) = \dot{\mathbf{B}}_n^{II}(x, y_g) \end{cases}$$

or:

$$\begin{cases} \dfrac{1}{\mu^I} \left. \dfrac{\partial \dot{A}_z^I(x,y)}{\partial y} \right|_{y=y_g} = \dfrac{1}{\mu^{II}} \left. \dfrac{\partial \dot{A}_z^{II}(x,y)}{\partial y} \right|_{y=y_g} \\[3mm] -\left. \dfrac{\partial \dot{A}_z^I(x,y)}{\partial x} \right|_{y=y_g} = -\left. \dfrac{\partial \dot{A}_z^{II}(x,y)}{\partial x} \right|_{y=y_g} \end{cases}$$

The results of the derivations are:

$$\begin{cases} \dfrac{1}{\mu^I} e^{\jmath \pi x / \tau_\nu}(\dot{c}_3^I \, e^{\dot{d}^I y_g} - \dot{c}_4^I \, e^{-\dot{d}^I y_g})\dot{d}^I = \dfrac{1}{\mu^{II}} e^{\jmath \pi x / \tau_\nu}(\dot{c}_3^{II} \, e^{\dot{d}^{II} y_g} - \dot{c}_4^{II} \, e^{-\dot{d}^{II} y_g})\dot{d}^{II} \\[4mm] \jmath \dfrac{\pi}{\tau_\nu} e^{\jmath \pi x / \tau_\nu}(\dot{c}_3^I e^{\pi y_g / \tau_\nu} + \dot{c}_4^I e^{-\pi y_g / \tau_\nu}) = \jmath \dfrac{\pi}{\tau_\nu} e^{\jmath \pi x / \tau_\nu}(\dot{c}_3^{II} \, e^{\dot{d}^{II} y_g} + \dot{c}_4^{II} \, e^{-\dot{d}^{II} y_g}) \end{cases}$$

The relationships between the coefficients $\dot{c}_3^{II}$ and $\dot{c}_4^{II}$ are:

$$\begin{cases} \dot{c}_3^I \dfrac{\pi}{\tau_\nu}\mu^I \, e^{\pi y_g/\tau_\nu} - \dot{c}_4^I \dfrac{\pi}{\tau_\nu}\mu^I \, e^{-\pi y_g/\tau_\nu} - \dot{c}_3^{II} \dfrac{\dot{d}^{II}}{\mu^{II}} e^{\dot{d}^{II} y_g} + \dot{c}_4^{II} \dfrac{\dot{d}^{II}}{\mu^{II}} e^{-\dot{d}^{II} y_g} & = 0 \\[2mm] \dot{c}_3^{II} e^{\pi y_g/\tau_\nu} + \dot{c}_4^{II} e^{\pi y_g/\tau_\nu} - \dot{c}_3^{II} \, e^{\dot{d}^{II} y_g} - \dot{c}_4^{II} \, e^{-\dot{d}^{II} y_g} & = 0 \end{cases}$$

The procedure can be repeated for other regions, obtaining, for region III:

$$\dot{A}_z^{III}(x,y) = (\dot{c}_1^{III} e^{\jmath \dot{c}^{III} x} + \dot{c}_2^{III} e^{-\jmath \dot{c}^{III} x})(\dot{c}_3^{III} \, e^{\dot{d}^{III} y} + \dot{c}_4^{III} \, e^{-\dot{d}^{III} y})$$

or

$$\dot{A}_z^{III}(x,y) = e^{\jmath \pi x/\tau_\nu}(\dot{c}_3^{III} \, e^{\dot{d}^{III} y} + \dot{c}_4^{III} \, e^{-\dot{d}^{III} y})$$

The boundary conditions at the border between region II and region III, at $y = y_c$, are:

$$\begin{cases} \dot{\mathbf{H}}_t^{II}(x,y_c) = \dot{\mathbf{H}}_t^{III}(x,y_c) \\ \dot{\mathbf{B}}_n^{II}(x,y_c) = \dot{\mathbf{B}}_n^{III}(x,y_c) \end{cases}$$

or:

$$\begin{cases} \dfrac{1}{\mu^{II}} \left. \dfrac{\partial \dot{A}_z^{II}(x,y)}{\partial y} \right|_{y=y_c} = \dfrac{1}{\mu^{III}} \left. \dfrac{\partial \dot{A}_z^{III}(x,y)}{\partial y} \right|_{y=y_c} \\[4mm] -\left. \dfrac{\partial \dot{A}_z^{II}(x,y)}{\partial x} \right|_{y=y_c} = -\left. \dfrac{\partial \dot{A}_z^{III}(x,y)}{\partial x} \right|_{y=y_c} \end{cases}$$

The results of the derivations are:

$$\begin{cases} \dfrac{1}{\mu^{II}} e^{\jmath \pi x/\tau_\nu}(\dot{c}_3^{II} \, e^{\dot{d}^{II} y_c} - \dot{c}_4^{II} \, e^{-\dot{d}^{II} y_c})\dot{d}^{II} = \dfrac{1}{\mu^{III}} e^{\jmath \pi x/\tau_\nu}(\dot{c}_3^{III} \, e^{\dot{d}^{III} y_c} - \dot{c}_4^{III} \, e^{-\dot{d}^{III} y_c})\dot{d}^{III} \\[4mm] \jmath \dfrac{\pi}{\tau_\nu} e^{\jmath \pi x/\tau_\nu}(\dot{c}_3^{II} \, e^{\pi y_c/\tau_\nu} + \dot{c}_4^{II} e^{-\pi y_c/\tau_\nu}) = \jmath \dfrac{\pi}{\tau_\nu} e^{\jmath \pi x/\tau_\nu}(\dot{c}_3^{III} \, e^{\dot{d}^{III} y_c} + \dot{c}_4^{III} \, e^{-\dot{d}^{III} y_c}) \end{cases}$$

The relationships between the coefficients $\dot{c}_3^{III}$ and $\dot{c}_4^{III}$ are:

$$\begin{cases} \dot{c}_3^{II} \dfrac{\dot{d}^{II}}{\mu^{II}} e^{\dot{d}^{II} y_c} - \dot{c}_4^{II} \dfrac{\dot{d}^{II}}{\mu^{II}} e^{-\dot{d}^{II} y_c} - \dot{c}_3^{III} \dfrac{\dot{d}^{III}}{\mu^{III}} e^{\dot{d}^{III} y_c} + \dot{c}_4^{III} \dfrac{\dot{d}^{III}}{\mu^{III}} e^{-\dot{d}^{III} y_c} & = 0 \\[2mm] \dot{c}_3^{II} e^{\dot{d}^{II} y_c} + \dot{c}_4^{II} e^{-\dot{d}^{II} y_c} - \dot{c}_3^{III} e^{\dot{d}^{III} y_c} - \dot{c}_4^{III} e^{-\dot{d}^{III} y_c} & = 0 \end{cases}$$

For the region IV:

$$\dot{A}_z^{IV}(x,y) = (\dot{c}_1^{IV} e^{J\dot{c}^{IV}x} + \dot{c}_2^{IV} e^{-J\dot{c}^{IV}x})(\dot{c}_3^{IV} e^{\dot{d}^{IV}y} + \dot{c}_4^{IV} e^{-\dot{d}^{IV}y})$$

or

$$\dot{A}_z^{IV}(x,y) = e^{J\pi x/\tau_\nu}(\dot{c}_3^{IV} e^{\dot{d}^{IV}y} + \dot{c}_4^{IV} e^{-\dot{d}^{IV}y})$$

The boundary conditions at the border between region III and region IV, at $y = y_m$, are:

$$\begin{cases} \dot{\mathbf{H}}_t^{III}(x,y_m) = \dot{\mathbf{H}}_t^{IV}(x,y_m) \\ \dot{\mathbf{B}}_n^{III}(x,y_m) = \dot{\mathbf{B}}_n^{IV}(x,y_m) \end{cases}$$

or:

$$\begin{cases} \dfrac{1}{\mu^{III}} \left.\dfrac{\partial \dot{A}_z^{III}(x,y)}{\partial y}\right|_{y=y_m} = \dfrac{1}{\mu^{IV}} \left.\dfrac{\partial \dot{A}_z^{IV}(x,y)}{\partial y}\right|_{y=y_m} \\ -\left.\dfrac{\partial \dot{A}_z^{III}(x,y)}{\partial x}\right|_{y=y_m} = -\left.\dfrac{\partial \dot{A}_z^{IV}(x,y)}{\partial x}\right|_{y=y_m} \end{cases}$$

The results of the derivations are:

$$\begin{cases} \dfrac{1}{\mu^{III}} e^{J\pi x/\tau_\nu}(\dot{c}_3^{III} e^{\dot{d}^{III}y_m} - \dot{c}_4^{III} e^{-\dot{d}^{III}y_m})\dot{d}^{III} = \dfrac{1}{\mu^{IV}} e^{J\pi x/\tau_\nu}(\dot{c}_3^{IV} e^{\dot{d}^{IV}y_m} - \dot{c}_4^{IV} e^{-\dot{d}^{IV}y_m})\dot{d}^{IV} \\ J\dfrac{\pi}{\tau_\nu} e^{J\pi x/\tau_\nu}(\dot{c}_3^{III} e^{\dot{d}^{III}y_m} + \bar{c}_4^{III} e^{-\dot{d}^{III}y_m}) = J\dfrac{\pi}{\tau_\nu} e^{J\pi x/\tau_\nu}(\dot{c}_3^{IV} e^{\dot{d}^{IV}y_m} + \dot{c}_4^{IV} e^{-\dot{d}^{IV}y_m}) \end{cases}$$

The relation between the coefficients $\dot{c}_3^{IV}$ and $\dot{c}_4^{IV}$ is:

$$\begin{cases} \dot{c}_3^{III} \dfrac{\dot{d}^{III}}{\mu^{III}} e^{\dot{d}^{III}y_m} - \dot{c}_4^{III} \dfrac{\dot{d}^{III}}{\mu^{III}} e^{-\dot{d}^{III}y_m} - \dot{c}_3^{IV} \dfrac{\dot{d}^{IV}}{\mu^{IV}} e^{\dot{d}^{IV}y_m} + \dot{c}_4^{IV} \dfrac{\dot{d}^{IV}}{\mu^{IV}} e^{-\dot{d}^{IV}y_m} = 0 \\ \dot{c}_3^{III} e^{\dot{d}^{III}y_m} + \dot{c}_4^{III} e^{-\dot{d}^{III}y_m} - \dot{c}_3^{IV} e^{\dot{d}^{IV}y_m} - \dot{c}_4^{IV} e^{-\dot{d}^{IV}y_m} = 0 \end{cases}$$

As for the region IV it can be assumed that the vector magnetic potential approaches zero if the y coordinate approaches infinity:

$$\lim_{y \to +\infty} \dot{A}_z^{IV}(x,y) = 0$$

So that

$$\dot{c}_3^{IV} = 0$$

Finally, the system can be reassumed in matrix notation as:

$$\mathbf{Ax} = \mathbf{B}$$

where the matrix $\mathbf{A}$ is defined as:

$$\mathbf{A} = \begin{pmatrix} 1 & -1 & 0 & 0 & 0 & 0 & 0 \\ \frac{\pi\mu^I}{\tau}e^{\frac{\pi y_g}{\tau}} & -\frac{\pi\mu^I}{\tau}e^{-\frac{\pi y_g}{\tau}} & -Be^{\dot{d}^{II}y_g} & Be^{-\dot{d}^{II}y_g} & 0 & 0 & 0 \\ e^{\frac{\pi y_g}{\tau}} & e^{-\frac{\pi y_g}{\tau}} & -e^{\dot{d}^{II}y_g} & -e^{-\dot{d}^{II}y_g} & 0 & 0 & 0 \\ 0 & 0 & Be^{\dot{d}^{II}y_c} & -Be^{-\dot{d}^{II}y_c} & -Ce^{\dot{d}^{III}y_c} & Ce^{-\dot{d}^{III}y_c} & 0 \\ 0 & 0 & e^{\dot{d}^{II}y_c} & e^{-\dot{d}^{II}y_c} & -e^{\dot{d}^{III}y_c} & -e^{-\dot{d}^{III}y_c} & 0 \\ 0 & 0 & 0 & 0 & Ce^{\dot{d}^{III}y_m} & -Ce^{-\dot{d}^{III}y_m} & De^{-\dot{d}^{IV}y_m} \\ 0 & 0 & 0 & 0 & e^{\dot{d}^{III}y_m} & e^{-\dot{d}^{III}y_m} & -e^{-\dot{d}^{IV}y_m} \end{pmatrix}$$

with $B = \frac{\dot{d}^{II}}{\mu^{II}}$, $C = \frac{\dot{d}^{III}}{\mu^{III}}$ and $D = \frac{\dot{d}^{IV}}{\mu^{IV}}$, and:

$$\mathbf{x} = \begin{pmatrix} \dot{c}_3^I \\ \dot{c}_4^I \\ \dot{c}_3^{II} \\ \dot{c}_4^{II} \\ \dot{c}_3^{III} \\ \dot{c}_4^{III} \\ \dot{c}_4^{IV} \end{pmatrix} \qquad\qquad \mathbf{B} = \begin{pmatrix} \frac{\tau_\nu}{\pi}\mu^I\hat{K}_s \\ 0 \\ 0 \\ 0 \\ 0 \\ 0 \\ 0 \end{pmatrix}$$

Losses calculation

For losses computation in each layer, the following expression can be used; it yields the surface loss density:

$$q_i = \frac{\omega^2\sigma_i}{2}\int_{y_{i-1}}^{y_i}\dot{A}^i\dot{A}^{i*}dy$$

Where $i = 1$ for region I, $i = 2$ for region II and so on, and the superscript * is used to indicate che complex conjugate. The product $\dot{A}^i\dot{A}^{i*}$ can be written as:

$$\dot{A}^i\dot{A}^{i*} = e^{\jmath\pi x/\tau_\nu}(\dot{c}_3^i\,e^{\dot{d}^iy} + \dot{c}_4^i\,e^{-\dot{d}^iy})e^{-\jmath\pi x/\tau_\nu}(\dot{c}_3^{i*}\,e^{\dot{d}^{i*}y} + \dot{c}_4^{i*}\,e^{-\dot{d}^{i*}y})$$

or:

$$\dot{A}^i\dot{A}^{i*} = \dot{c}_3^i\,e^{\dot{d}^i y}\dot{c}_3^{i*}\,e^{\dot{d}^{i*} y} + \dot{c}_3^i\,e^{\dot{d}^i y}\dot{c}_4^{i*}\,e^{-\dot{d}^{i*} y} + \dot{c}_4^i\,e^{-\dot{d}^i y}\dot{c}_3^{i*}\,e^{\dot{d}^{i*} y} + \dot{c}_4^i\,e^{-\dot{d}^i y}\dot{c}_4^{i*}\,e^{-\dot{d}^{i*} y} =$$
$$\dot{c}_3^i\dot{c}_3^{i*}\,e^{\dot{d}^{i*} y}\,e^{\dot{d}^i y} + \dot{c}_3^i\dot{c}_4^{i*}\,e^{-\dot{d}^{i*} y}\,e^{\dot{d}^i y} + \dot{c}_4^i\dot{c}_3^{i*}\,e^{\dot{d}^{i*} y}\,e^{-\dot{d}^i y} + \dot{c}_4^i\dot{c}_4^{i*}\,e^{-\dot{d}^{i*} y}\,e^{-\dot{d}^i y}$$

The following simplifications can be used:

$$\begin{aligned}
e^{\dot{d}^{i*} y}\,e^{\dot{d}^i y} &= e^{2Re(\dot{d}^i)y} \\
e^{-\dot{d}^{i*} y}\,e^{\dot{d}^i y} &= e^{j2Im(\dot{d}^i)y} \\
e^{\dot{d}^{i*} y}\,e^{-\dot{d}^i y} &= e^{-j2Im(\dot{d}^i)y} \\
e^{-\dot{d}^{i*} y}\,e^{-\dot{d}^i y} &= e^{-2Re(\dot{d}^i)y}
\end{aligned}$$

so the expression become:

$$\dot{A}\dot{A}^* = |\dot{c}_3^i|^2\,e^{2Re(\dot{d}^i)y} + |\dot{c}_4^i|^2\,e^{-2Re(\dot{d}^i)y} + \dot{c}_3^i\dot{c}_4^{i*}e^{j2Im(\dot{d}^i)y} + \dot{c}_3^{i*}\dot{c}_4^i e^{-j2Im(\dot{d}^i)y}$$

The terms $\dot{c}_3^i\dot{c}_4^{i*}e^{j2Im(\dot{d}^i)y}$ and $\dot{c}_3^{i*}\dot{c}_4^i e^{-j2Im(\dot{d}^i)y}$ are complex conjugated, so that its sum yields:

$$\begin{aligned}
\dot{c}_3^i\dot{c}_4^{i*}e^{j2Im(\dot{d}^i)y} + \dot{c}_3^{i*}\dot{c}_4^i e^{-j2Im(\dot{d}^i)y} &= 2Re(\dot{c}_3^i\dot{c}_4^{i*}e^{j2Im(\dot{d}^i)y}) = \\
&= 2Re(|\dot{c}_3^i||\dot{c}_4^i|e^{j(\angle\dot{c}_3^i - \angle\dot{c}_4^i)}\,e^{j2Im(\dot{d}^i)y}) = \\
&= 2Re(|\dot{c}_3^i||\dot{c}_4^i|e^{j(\angle\dot{c}_3^i - \angle\dot{c}_4^i + 2Im(\dot{d}^i)y)}) = \\
&= 2|\dot{c}_3^i||\dot{c}_4^i|\cos(\angle\dot{c}_3^i - \angle\dot{c}_4^i + 2Im(\dot{d}^i)y)
\end{aligned}$$

Finally, for obtaining the surface loss in each region, in W/m^2, the following expression have to be integrated:

$$q = \frac{\omega^2\sigma^i}{2}\int_{y_{i-1}}^{y_i}\left\{|\dot{c}_3^i|^2\,e^{2Re(\dot{d}^i)y} + |\dot{c}_4^i|^2\,e^{-2Re(\dot{d}^i)y} + 2|\dot{c}_3^i||\dot{c}_4^i|\cos(\angle\dot{c}_3^i - \angle\dot{c}_4^i + 2Im(\dot{d}^i)y)\right\}dy =$$

$$= \frac{\omega^2\sigma^i}{2}\left\{|\dot{c}_3^i|^2\left.\frac{e^{2Re(\dot{d}^i)y}}{2Re(\dot{d}^i)}\right|_{y_{i-1}}^{y_i} + |\dot{c}_4^i|^2\left.\frac{e^{-2Re(\dot{d}^i)y}}{-2Re(\dot{d}^i)}\right|_{y_{i-1}}^{y_i} + \right.$$

$$\left. + 2|\dot{c}_3^i||\dot{c}_4^i|\left.\frac{\sin(\angle\dot{c}_3^i - \angle\dot{c}_4^i + 2Im(\dot{d}^i)y)}{2Im(\dot{d}^i)}\right|_{y_{i-1}}^{y_i}\right\} =$$

$$= \frac{\omega^2\sigma^i}{2}\left\{\frac{|\dot{c}_3^i|^2\,(e^{2Re(\dot{d}^i)y_i} - e^{2Re(\dot{d}^i)y_{i-1}})}{2Re(\dot{d}^i)} - \frac{|\dot{c}_4^i|^2\,(e^{-2Re(\dot{d}^i)y_i} - e^{-2Re(\dot{d}^i)y_{i-1}})}{2Re(\dot{d}^i)} + \right.$$

$$\left. + \frac{2|\dot{c}_3^i||\dot{c}_4^i|}{2Im(\dot{d}^i)}(\sin(\angle\dot{c}_3^i - \angle\dot{c}_4^i + 2Im(\dot{d}^i)y_i) - \sin(\angle\dot{c}_3^i - \angle\dot{c}_4^i + 2Im(\dot{d}^i)y_{i-1}))\right\}$$

Map of the rotor losses

In spite of the inevitable simplifications, e.g. the straighten geometry, the analytical model allows a rapid comparison between various machines. Hereafter, a comparison is carried out referring to various combinations of the number of slots Q and number of poles $2p$.

The analytical straight–lined model with four layers is considered for the computations. The four layers of the model are fixed like this:

- The first layer (Fig. 1.24) represents the air–gap (conductivity $\sigma_{gap} = 0$ MS/m and relative permeability $\mu_{gap} = 1$), whose thickness is equal to 1 mm.

- Second layer represents the cover sheet whose thickness is equal to 1 mm as well. Its conductivity and permeability are considered as a non–conductive sheet (air): $\sigma_{cover} = 0$ and $\mu_{cover} = 1$.

- The third layer has thickness of 15 mm and represents the PMs ($\sigma_{PM} = 0.694$ MS/m, $\mu_{PM} = 1.05$).

- The fourth layer has thickness of 20 mm and represents the iron yoke ($\sigma_{Fe} = 10.44$ MS/m, $\mu_{Fe} = 5000$).
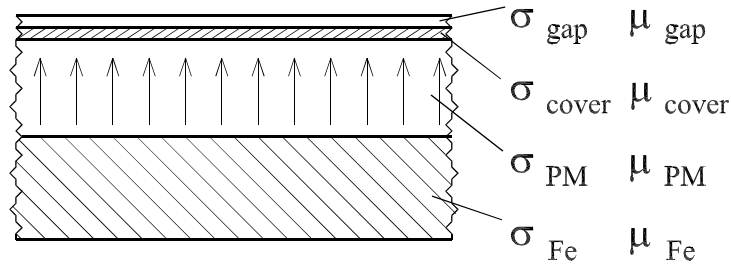
Figure 1.24: *Four–layer model used in the analytical computation.*

In the computation, the amplitude of the main stator linear current density has been fixed to be $\hat{K}_s = 50$ kA/m, and the rotor speed to $n = 100$ rpm. The harmonic effect has been considered up to the 1000–th harmonic. Their rotating speed has been computed as reported in (1.4). The computed losses are reported to a machine with diameter $D = 1$ m and a stack length $L_{stk} = 1$ m.

Table 1.2 and Table 1.3 report the computed rotor losses assuming a double–layer and a single–layer winding, respectively. The slots are reported along the columns, while the poles are reported along the rows.

Other configurations have been simulated, even though not reported here: they exhibit a similar dependence of rotor losses on the slot and pole combination. The addition of a 1 mm conductive cover sheet yields an increase of the losses.

Table 1.2: *Rotor losses (kW), non–conductive sheet, double–layer winding*

2p	number of slots																				
	78	81	84	87	90	93	96	99	102	105	108	111	114	117	120	123	126	129	132	135	138
40	2.0	1.8	1.8	1.8	2.1	1.9	1.3	0.8	1.1	1.9	1.3	0.8	0.7	0.5	**0.3**	0.4	0.5	0.5	0.6	0.8	0.5
42	—	1.9	—	1.7	1.7	—	—	1.6	—	—	1.3	—	—	0.8	—	—	**0.3**	—	—	0.5	—
44	1.8	2.0	1.8	1.6	1.5	1.6	1.6	1.8	1.7	**1.3**	**0.7**	**0.7**	1.5	1.6	0.8	0.7	0.5	0.4	**0.2**	0.3	0.4
46	2.1	1.6	1.9	1.8	1.5	1.4	1.4	1.4	1.6	1.6	1.5	1.0	**0.6**	0.9	1.6	1.3	0.7	0.7	0.5	0.4	**0.2**
48	—	2.1	—	—	1.9	—	—	1.3	—	—	1.6	—	—	**0.8**	—	—	1.6	—	—	0.6	—
50	1.7	1.7	2.0	1.4	1.6	1.7	1.4	1.2	1.2	1.2	1.2	1.4	1.4	1.4	**1.0**	**0.6**	**0.6**	1.2	1.4	0.9	0.6
52	**1.4**	1.6	1.6	1.9	1.4	1.5	1.6	1.3	1.2	1.1	1.1	1.2	1.2	1.4	1.3	1.2	0.8	**0.5**	**0.7**	1.3	1.3
54	—	**1.3**	—	—	—	—	—	—	—	—	—	—	—	—	—	—	—	—	—	—	—
56	2.0	1.6	**1.2**	1.4	1.4	1.6	1.4	1.2	1.4	1.5	1.1	1.0	1.0	1.0	1.0	1.1	1.2	1.2	1.1	**0.8**	**0.5**
58	2.3	1.8	1.5	**1.1**	1.3	1.4	1.5	1.4	1.1	1.4	1.4	1.1	1.0	0.9	0.9	1.0	0.9	1.1	1.2	1.2	1.0
60	—	2.1	—	—	**1.0**	—	—	1.3	—	—	1.3	—	—	0.9	—	—	0.9	—	—	1.1	—
62	2.4	2.4	1.9	1.6	1.3	**1.0**	1.1	1.2	1.2	1.4	0.9	1.2	1.2	1.1	0.9	0.8	0.8	0.8	0.9	0.8	1.0
64	2.8	2.2	2.2	1.7	1.5	1.2	**0.9**	1.1	1.1	1.1	1.3	0.9	1.1	1.2	1.2	0.9	0.8	0.7	0.8	0.8	0.8
66	—	2.5	—	—	1.5	—	—	**0.8**	—	—	1.0	—	—	1.0	—	—	0.8	—	—	0.7	—
68	3.3	2.9	2.2	2.0	1.9	1.4	1.3	1.1	**0.8**	1.0	1.0	0.9	1.2	1.0	0.8	1.1	1.0	0.9	0.8	0.7	0.7
70	3.5	3.0	2.7	2.0	1.9	1.8	1.4	1.2	1.0	**0.7**	0.9	0.9	0.9	1.2	1.0	0.7	1.1	1.0	0.9	0.8	0.7
72	—	3.3	—	—	—	—	—	—	—	—	**0.7**	—	—	—	—	—	—	—	—	0.9	—
74	3.6	3.1	3.0	2.6	2.2	1.7	1.8	1.5	1.2	1.0	0.9	**0.7**	0.8	0.8	0.8	1.0	1.0	0.7	0.9	1.0	0.9
76	3.8	3.4	3.0	2.7	2.5	2.0	1.6	1.7	1.4	1.1	1.0	0.8	**0.6**	0.8	0.8	0.8	1.0	1.0	0.7	0.8	1.0
78	—	3.5	—	—	2.5	—	—	1.6	—	—	1.1	—	—	**0.6**	—	—	0.8	—	—	0.7	—
80	4.5	3.6	3.2	2.8	2.7	2.3	2.2	1.6	1.5	1.5	1.2	1.0	0.9	0.7	**0.6**	0.7	0.7	0.7	0.8	0.9	0.7
82	5.0	3.9	3.3	2.9	2.6	2.5	2.2	2.1	1.5	1.5	1.4	1.1	1.0	0.8	0.7	**0.5**	0.7	0.7	0.7	0.8	0.9
84	—	4.4	—	—	2.8	—	—	2.1	—	—	1.4	—	—	0.9	—	—	**0.5**	—	—	0.7	—
86	6.2	4.9	3.8	3.2	2.8	2.5	2.4	2.1	2.0	1.7	1.3	1.4	1.2	1.0	0.9	0.7	0.6	**0.5**	0.6	0.7	0.7
88	6.7	5.3	4.3	3.4	2.9	2.6	2.2	2.3	2.0	2.0	1.5	1.2	1.3	1.2	0.9	0.8	0.7	0.6	**0.5**	0.6	0.6
90	—	6.0	—	—	—	—	—	—	—	—	1.9	—	—	—	—	—	—	—	—	**0.4**	—
92	8.2	6.4	5.2	4.2	3.3	2.8	2.5	2.3	2.1	2.0	1.8	1.8	1.2	1.2	1.2	1.0	0.8	0.8	0.6	0.5	**0.4**
94	8.8	7.3	5.8	4.6	3.7	3.0	2.6	2.3	2.1	2.0	1.8	1.7	1.6	1.1	1.1	1.1	1.0	0.8	0.7	0.6	0.5
96	—	7.8	—	—	4.1	—	—	2.4	—	—	1.9	—	—	1.4	—	—	1.1	—	—	0.7	—
98	12.1	8.5	7.0	5.5	4.5	3.6	2.9	2.5	2.2	2.1	1.8	1.8	1.6	1.7	1.3	1.0	1.1	1.0	0.9	0.7	0.6
100	13.4	9.9	7.3	6.1	5.0	4.0	3.2	2.6	2.3	2.1	1.9	1.8	1.7	1.5	1.6	1.2	1.0	1.1	1.0	0.8	0.7
102	—	11.4	—	—	5.2	—	—	2.9	—	—	1.9	—	—	1.6	—	—	1.0	—	—	0.9	—
104	15.6	12.7	9.5	7.0	5.9	4.8	3.8	3.2	2.6	2.2	2.0	1.9	1.6	1.6	1.5	1.5	1.4	1.0	0.9	1.0	0.9

Table 1.3: *Rotor losses (kW), non–conductive sheet, single–layer winding*

2p										number of slots											
	78	81	84	87	90	93	96	99	102	105	108	111	114	117	120	123	126	129	132	135	138
40	—	—	—	—	—	—	—	—	7.8	—	3.6	—	0.9	—	**0.3**	—	1.4	—	0.9	—	0.9
42	—	—	—	—	—	—	—	—	—	—	2.3	—	—	—	—	—	**0.3**	—	—	—	—
44	—	—	—	—	—	—	—	—	—	—	—	—	5.7	—	1.3	—	1.6	—	**0.2**	—	0.5
46	—	—	—	—	—	—	—	—	—	—	—	—	—	—	2.2	—	2.0	—	0.7	—	**0.2**
48	—	—	—	—	—	—	—	—	—	—	—	—	—	—	—	—	2.1	—	—	—	—
50	16.8	—	—	—	—	—	—	—	—	—	—	—	—	—	—	—	2.8	—	2.0	—	1.5
52	—	—	—	—	—	—	—	—	—	—	—	—	—	—	—	—	—	—	3.0	—	1.8
54	—	—	—	—	—	—	—	—	—	—	—	—	—	—	—	—	—	—	—	—	—
56	13.9	—	15.1	—	—	—	—	—	—	—	—	—	—	—	—	—	—	—	—	—	—
58	4.7	—	16.8	—	—	—	—	—	—	—	—	—	—	—	—	—	—	—	—	—	—
60	—	—	—	—	13.6	—	—	—	—	—	—	—	—	—	—	—	—	—	—	—	—
62	6.1	—	17.8	—	**2.7**	—	—	—	—	—	—	—	—	—	—	—	—	—	—	—	—
64	10.6	—	18.0	—	15.6	—	12.2	—	—	—	—	—	—	—	—	—	—	—	—	—	—
66	—	—	—	—	3.8	—	—	—	—	—	—	—	—	—	—	—	—	—	—	—	—
68	9.3	—	6.0	—	16.7	—	14.1	—	11.1	—	—	—	—	—	—	—	—	—	—	—	—
70	14.3	—	13.9	—	4.9	—	14.7	—	**2.1**	—	—	—	—	—	—	—	—	—	—	—	—
72	—	—	—	—	—	—	—	—	—	—	10.1	—	—	—	—	—	—	—	—	—	—
74	11.4	—	10.6	—	6.0	—	15.5	—	2.8	—	11.5	—	—	—	—	—	—	—	—	—	—
76	5.1	—	13.3	—	13.6	—	15.1	—	7.0	—	**2.1**	—	9.3	—	—	—	—	—	—	—	—
78	—	—	—	—	8.9	—	—	—	—	—	12.2	—	—	—	—	—	—	—	—	—	—
80	8.7	—	5.3	—	9.3	—	12.9	—	7.6	—	6.5	—	10.8	—	8.5	—	—	—	—	—	—
82	12.8	—	4.4	—	12.5	—	12.2	—	3.9	—	13.4	—	**2.2**	—	9.6	—	—	—	—	—	—
84	—	—	—	—	5.7	—	—	—	—	—	3.7	—	—	—	—	—	—	—	—	—	—
86	21.0	—	5.0	—	9.1	—	8.4	—	5.8	—	13.5	—	2.5	—	10.3	—	7.8	—	—	—	—
88	15.9	—	8.2	—	3.9	—	6.2	—	6.0	—	13.3	—	6.2	—	**2.3**	—	**1.3**	—	7.2	—	—
90	—	—	—	—	—	—	—	—	—	—	11.9	—	—	—	—	—	7.5	—	—	—	—
92	22.5	—	18.5	—	6.6	—	4.2	—	7.5	—	5.6	—	5.7	—	11.8	—	5.7	—	**1.4**	—	6.7
94	26.6	—	13.7	—	10.1	—	3.5	—	11.0	—	10.1	—	4.1	—	12.1	—	**1.9**	—	8.8	—	**1.1**
96	—	—	—	—	7.7	—	—	—	—	—	8.4	—	—	—	—	—	11.0	—	—	—	—
98	28.4	—	18.2	—	16.6	—	3.9	—	7.4	—	6.7	—	5.5	—	12.1	—	2.9	—	9.8	—	1.4
100	30.7	—	23.6	—	9.2	—	5.1	—	3.1	—	10.3	—	9.3	—	11.1	—	5.2	—	**2.1**	—	5.4
102	—	—	—	—	20.7	—	—	—	—	—	4.1	—	—	—	—	—	2.9	—	—	—	—
104	31.3	—	14.2	—	11.9	—	8.1	—	5.1	—	3.5	—	6.1	—	5.5	—	11.6	—	10.8	—	9.5

Discussion

Fig. 1.25 and Fig. 1.26 aim to summarize and generalize the results achieved in Tables 1.2 and 1.3.
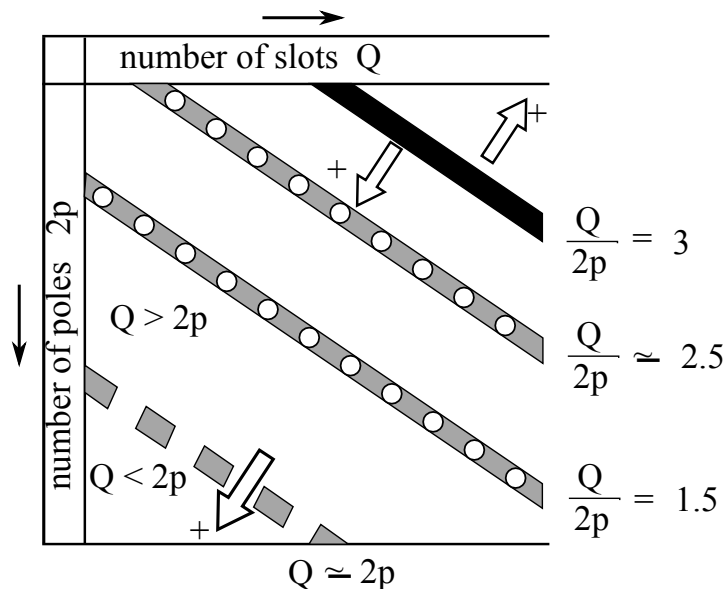
Figure 1.25: *Map of the rotor losses with double layer windings.*
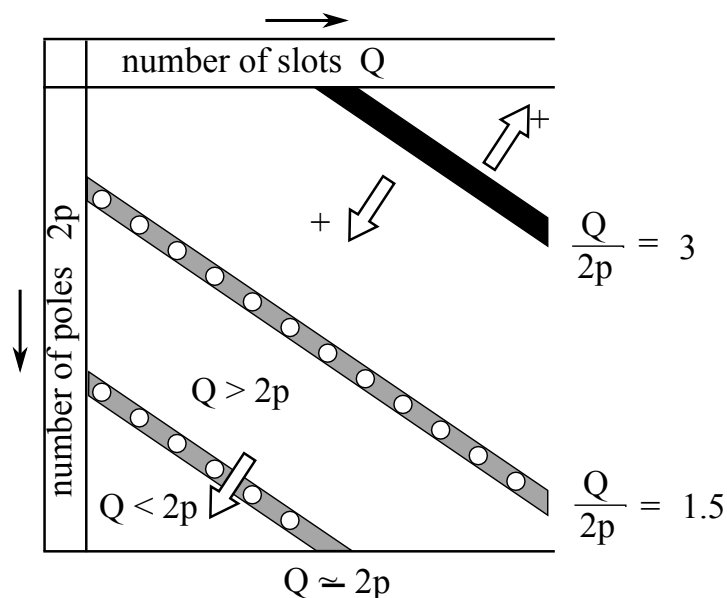

Figure 1.26: *Map of the rotor losses with single layer windings.*

At first, let us consider Fig. 1.25 that refers to the machines with double–layer winding. The lower rotor losses are found along the line of the integer–slot configurations, the black bold line of Fig. 1.25, where the number of slots per poles $Q/2p$ is equal to the number of phases $m = 3$.

This configuration is characterized by low harmonic contents: there are only harmonics of odd order multiple of p, with decreasing amplitude, and no third harmonics and sub–harmonics.

Moving along all directions from the line $Q/2p = 3$, the rotor losses increase, as highlighted by the white arrows around the line.

Although the rotor losses increase when moving away from the line, the increase is not monotonic. There are some local minima, highlighted with circles. They are found along the lines characterized by $Q/2p \approx 2.5$ and $Q/2p = 1.5$. They are represented by two gray lines in Fig. 1.25. Along these lines, there are local minima. Let us note that in the machines with $Q/2p = 1.5$, the machine periodicity returns to be $t = p$, so that there are not MMF sub–harmonics. It is possible to demonstrate that there are all harmonics of the corresponding integer–slot configuration plus the harmonics of even order.

Fig. 1.25 also shows the border line $Q = 2p$. There is no local minima along this line (to this aim, the line has been drawn with dashes). On the contrary, the rotor losses continue to increase as the number of slots decreases with respect to the number of poles. This is underlined by the white arrow crossing the line $Q/2p = 1$.

As far as the machines with single–layer winding are concerned, Fig. 1.26 tries to summarize the results of the Table 1.3.

The lower rotor losses are found again along the line of the integer–slot configurations, the black bold line of Fig. 1.26 where $Q/2p = 3$. Of course, the computed rotor losses are the same of those computed with the double–layer winding.

As above, along all directions from the line $Q/2p = 3$, the rotor losses increase (white arrows are used again). These losses are generally higher than those computed with the same slot and pole combinations using a double–layer winding. Fig. 1.26 also highlights that there are many combinations of slots and poles that do not yield a feasible three–phase winding. In other words, the transformation from double– to single–layer winding is not feasible [27].

There are again some local minima (see the small white circles). They are found along the line $Q/2p = 1.5$, the gray dashed line in Fig. 1.26. However, these minima are not all the combinations along the line $Q/2p = 1.5$, but there are only some combinations that exhibit lower rotor losses. In order to highlight the presence of some local minima, small circles are drawn in the map.

Finally, it has been found that other rotor losses minima are around the line $Q = 2p$, as also highlighted in Fig. 1.25 using small circles again. Let us note that this happens only when single–layer windings are used. Then, the rotor losses continue to increase as the number of slots decreases with respect to the number of poles, as pointed out by the white arrow.

1.3 Conclusions

Simple straight–lined analytical models have been considered for the computation of the losses induced in the rotor by the MMF harmonics. They have been used to compare the rotor losses due to different combinations of slot and pole numbers. The advantage of such models is that they allow to focus on the impact of the various parameters such as frequency f, harmonic order ν, material properties μ and σ, air–gap thickness y_g, on the power loss density.

These models prove to be an useful tool in the design task of such machines. The obtained results yield to give general rules to design fractional–slot PM machines with reduced rotor losses.

It has been demonstrated that rotor losses depend on contrasting factors. They increase with the specific wavelength ξ and with the harmonic order ν. However ξ decreases when ν increases. Therefore, it is not easy to determine the order of the MMF harmonic causing the highest rotor losses.

In addition, the losses caused by a given MMF harmonic of order ν result to be proportional to the winding factor of order ν squared. Since the MMF sub–harmonics are characterized by the higher values of the specific wavelength ξ, their winding factor has to be low, in order to avoid to get very high rotor losses.

The impact of the air–gap has been also investigated. The main effect is a reduction of the power loss density caused by the harmonics of higher order, while its impact is negligible for the harmonics of lower order. The effect of the air–gap is like a "low pass filter" for the MMF harmonics.

Finite elements computation of rotor losses

Abstract

The effort of this chapter is to fix a reference PM machine (i.e. a benchmark PM machine) whose rotor losses are easily computed for any given geometry. The computation is necessarily based on a simplified model of the machine, so as to achieve a more general result that can be easily applied to a set of PM machines.

The analytical prediction of the rotor losses is compared with the results obtained by means of the finite element computation. A good agreement between analytical and FE results is achieved.

2.1 Finite element modeling

This chapter deals with the computation of rotor losses by means of finite elements. At first, the MMF distribution is split in its harmonic components, using the Fourier series expansion. An example is shown in Fig. 1.2. Then, for each ν-th MMF harmonic, the following procedure is adopted:

- The stator is substituted by an infinitesimal conductive sheet placed at the stator inner diameter D, as shown in Fig. 2.1.
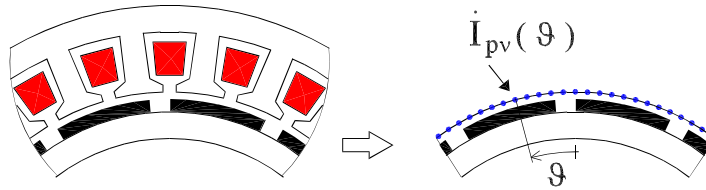

Figure 2.1: *Model used in rotor losses computation by means of finite elements.*

- A linear current density $K_{s\nu}(\vartheta)$, sinusoidally distributed in the space, is imposed in such a conductive sheet. The distribution is described by $\sin(\nu\vartheta)$, where ϑ is the azimuthal coordinate in mechanical radians. The peak value is achieved from the corresponding amplitude of the MMF harmonic $\hat{U}_{s\nu}$ as

$$\hat{K}_{s\nu} = 2\nu \frac{\hat{U}_{s\nu}}{D} \tag{2.1}$$

- The circumference is split in a large number of points, say N_p. Their distance is $\pi D/N_p$. In each point a prefixed *point current* $I_{p\nu}$ is assigned, as shown in Fig. 2.1. According to the ν-th harmonic, the maximum current value is computed from the electric loading $\hat{K}_{s\nu}$, as $\hat{I}_{p\nu} = \hat{K}_{s\nu}\pi D/N_p$.

- The linear current density waveform rotates along the air-gap with a fixed speed (i.e. $\omega_{\nu r}$ given by (1.4) in the rotor reference frame). Thus the source current has to be alternating at a given frequency. Using the symbolic notation, in the generic angular position ϑ, the *point current* is forced to be

$$\dot{I}_{p\nu}(\vartheta) = \hat{I}_{p\nu}e^{j\nu\vartheta} \tag{2.2}$$

In other words, the phase of the current (i.e. $\nu\vartheta$) is fixed to be a function of the geometrical position ϑ of the point in which the current itself is assigned.

- The frequency of the simulation is computed as in (1.5).

As far as the rotor is concerned, the simulation needs a particular care adopting a two–dimensional analysis, so as the eddy currents are computed correctly. In each object, electrically insulated by the others, a total current equal to zero is imposed as a further constraint. This avoids that eddy currents may flow through different objects. In addition, when insulated laminations are considered, no eddy current flows through them, therefore a zero conductivity is fixed.

The rotor losses are computed separately for harmonics of various orders. Then they are superimposed to achieved the total losses.

Finally, let us remember that in a two–dimensional simulation the end effects are neglected. The resistance of the rotor paths are lower than actual values, and this yields a slightly overestimation of the rotor losses.

2.2 Cases of study: simplified rotor models

The computation using finite elements is not constrained in the rotor geometry, unlike the analytical computation that requires a simplified multi–layer rotor. The actual rotor geometry can be taken into account, including both surface–mounted and interior permanent magnet rotors. However, for the sake of generality, the finite element computation of rotor losses is carried out over some simple rotor models, that can be considered as benchmarks. The model geometries are shown in Fig. 2.2.
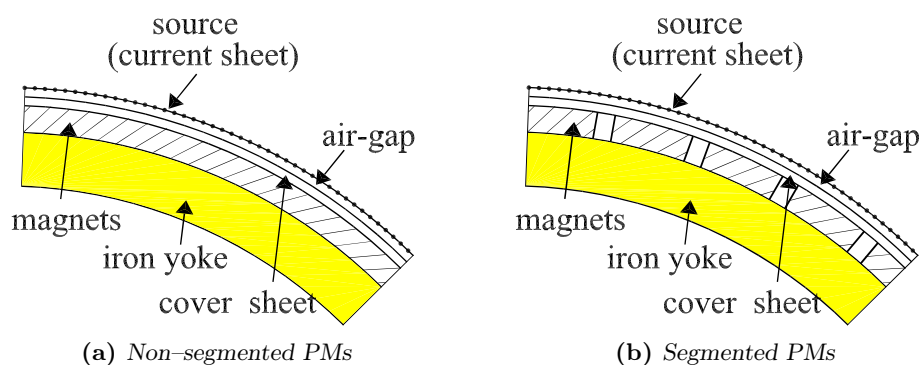

(a) *Non–segmented PMs*   (b) *Segmented PMs*

Figure 2.2: *Cases of study*

The cases of study are:

case 1: Machine with conductive surface-mounted PM (e.g. NdFeB PMs), and a copper sheet covering the PMs. The PMs are considered as a unique ring in which the currents can flow with no limitations. The corresponding geometry is drawn in Fig. 2.2a.

case 2: Machine with conductive PMs (e.g. NdFeB PMs), and no cover sheet. The geometry is shown in Fig. 2.2b. The PMs are considered as a unique ring in which the currents can flow with no limitations.

case 3: As before, but the PMs are separated and insulated, as shown in Fig. 2.2b. The total current over the cross–area of each PM is constrained to be zero, so as to avoid that eddy currents flow through various PMs (that is possible in a two–dimensional analysis).

Table 2.1: *Computation data*

	gap	copper		magnets		yoke	
		σ	thick.	σ	thick.	σ	thick.
case	(mm)	(MS/m)	(mm)	(MS/m)	(mm)	(MS/m)	(mm)
1	1	58	1	0.694	15	10.44	20
2	2	–	–	0.694	15	10.44	20
3	2	–	–	0.694	15	10.44	20
4	2	–	–	0	15	10.44	20

case 4: Machine with surface-mounted PM of low conductivity (e.g. plastic NdFeB PM), and no cover sheet.

In all models, the air–gap diameter is assumed to be $D = 1$ m, and the stack length $L_{stk} = 1$ m. Air–gap thickness has been fixed to be equal to 2 mm, except in the first case, in which 1–mm copper cover sheet reduced the air–gap to 1 mm. Each material is characterized by the conductivity σ and by the thickness reported in Table 2.1.

2.3 Impact of harmonics of different order on rotor losses

In this section, the impact of the various harmonics on the rotor losses is investigated. It is demonstrated that the sub–harmonics are the main causes of rotor losses. In the following comparison, the main harmonic has been fixed to be the harmonic of order $\nu = p = 50$. Then, **all** harmonics of order lower and higher than the main one have been superimposed, and the corresponding rotor losses have been computed.

For all harmonics, the amplitude of the stator linear current density has been fixed to be $\hat{K}_{s\nu} = 10$ kA/m. The rotating speed $\omega_{\nu r}$ of the harmonics has been computed from (1.4) with ω=314 rad/s and assuming always $sgn = +1$.

Although this is not a real case (it is assumed that there are all harmonics of linear current density of constant amplitude), the result highlights which harmonic order induces higher rotor current causing higher rotor losses.

Fig. 2.3 shows the rotor losses computed in the various models versus the order of the MMF harmonics. Because of the same amplitude of the stator linear current density, these figures gives an immediate view of the impact of each harmonic order. In all cases, it is worth noticing that rotor losses decrease with the increasing harmonic order. This confirms that the sub–harmonics have a heavy impact on rotor losses. Because of their large wavelength, they enter deeply in the rotor yoke and are only marginally shielded by a copper sheet or PMs.

Fig. 2.3a shows the rotor losses computed in the model of case 1, considering the copper sheet covering the PMs. The higher losses are in the sheet that shields the flux lines, and in the rotor yoke.

Fig. 2.3b shows the rotor losses computed in the model of case 2. Without the copper sheet, the losses are found in the PM and in the iron yoke, allocated about one fifth in the PM and four fifth in the yoke. The losses are higher than in case 1: this means that copper losses has

a beneficial effect on losses reduction. However this will be contradicted when actual machines will be analyzed.

In case 3, in which the PMs are separated, the eddy current in the PMs are very low, see Fig. 2.3c. Therefore the flux lines enter in the magnetic rotor yoke (especially the low order harmonic) and the rotor losses are almost only in the iron yoke. The result is practically the same than in case 4 (see Fig. 2.3d), in which there are not current in the PMs because of $\sigma_{PM} = 0$.
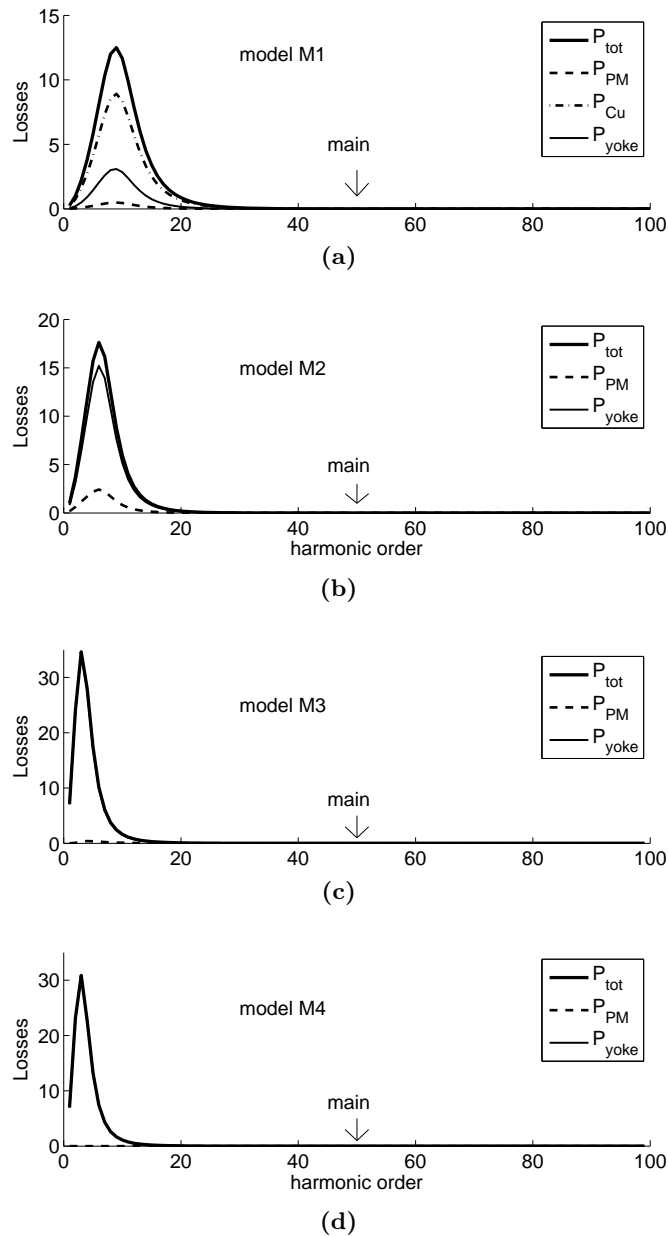

Figure 2.3: *Analysis of the impact of the MMF harmonics of various order on the rotor losses (case 1 to 4). All harmonics are considered.*

2.4 Rotor losses in two specific machines

Let us consider now two different machines, with their actual MMF harmonic contents. A 108–slot 106–pole machine and a 96–slot 160–pole machine are investigated. A double–layer winding is considered for both machines. The MMF harmonic contents of the 108–slot 106–pole machine are shown in Fig. 1.2a, which underlines that there are several sub–harmonics but of low amplitude. The MMF harmonic contents of the 96–slot 160–pole machine are shown in Fig. 2.4. This combination of slots and poles has been chosen to have one MMF harmonic of low–order of high amplitude so as to emphasize its impact on rotor losses.
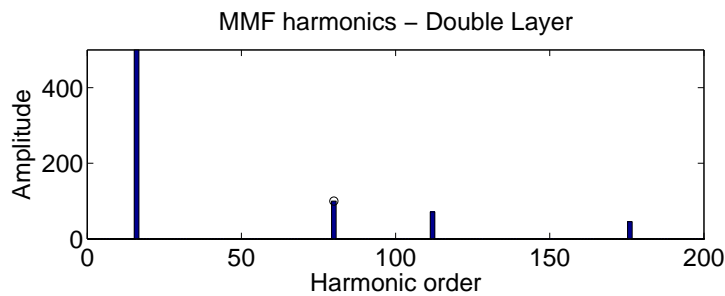
Figure 2.4: *Normalized MMF harmonic contents of a 96–slot 160–pole machine, with double–layer*

The resulting losses are reported in Fig. 2.5 and Fig. 2.6 respectively.

Figure 2.5: *Rotor losses in a 108–slot 106–pole SPM machine (double–layer winding), whose MMF harmonics are drawn in Fig. (a).*

They refer to the four cases described in Table 2.1. The amplitude of the main stator linear current density is fixed to be equal to $\hat{K}_s = 50$ kA/m, and to a rotor speed of $n = 100$ rpm.

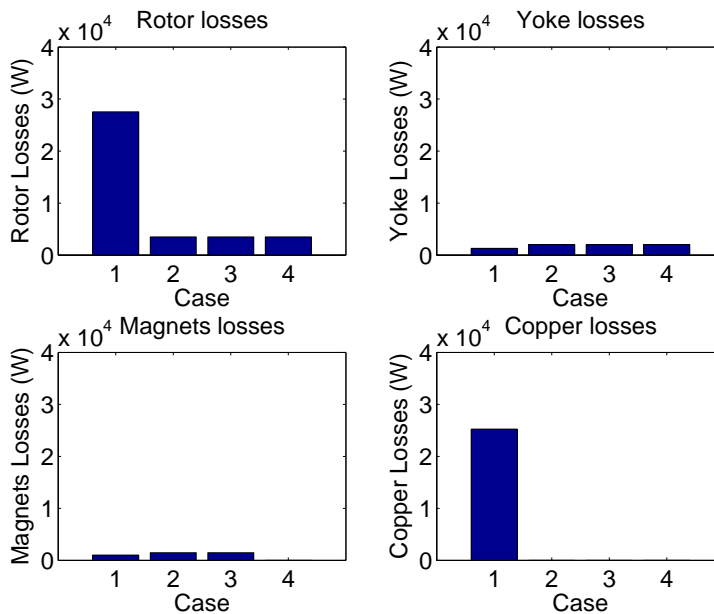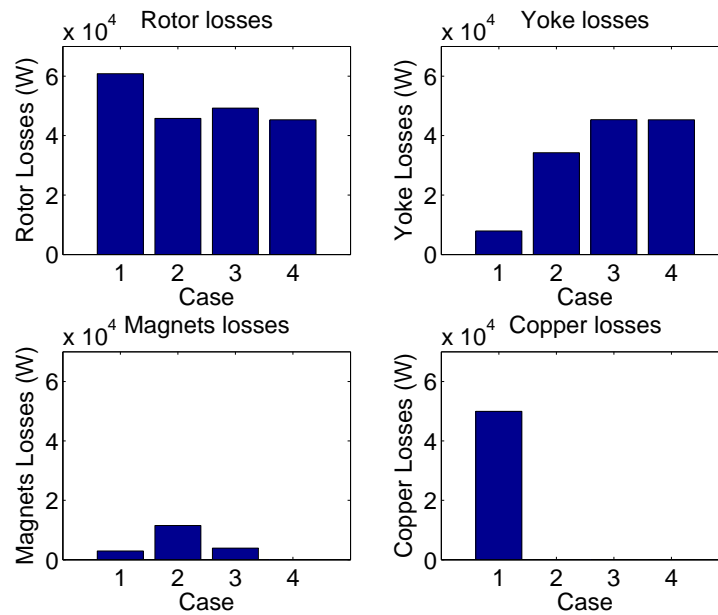**Figure 2.6:** *Rotor losses in a 96–slot 160–pole SPM machine (double–layer winding), whose MMF harmonics are drawn in Fig. 2.4.*

In both motors, the copper sheet (used in configuration of case 1) has a negative effect. When the copper sheet is used, the total rotor losses always increase. This result is mainly due to the presence of the MMF sub–harmonics, which are not shielded by the copper sheet.

In the other cases, that is, without the copper sheet, the higher losses are found in the rotor yoke. The losses in the PM are lower, especially when the PMs are insulated (case 3).

Comparing the two motor configurations, it is worth noticing that the losses in the 108–slot 106–pole SPM machine are very lower than in the 96–slot 160–pole SPM machine. This is caused by the high MMF sub–harmonic in the second configuration. Because of the large wavelength, the sub–harmonic flux enters deeply in the rotor. One sub–harmonic of high amplitude is enough to produce a great amount of rotor losses, higher than those produced by a large number of sub–harmonics of lower amplitude.

2.5 FEM comparisons

This section reports a comparison between the analytical and the FEM computation of the power loss density. The comparison has been carried out imposing a linear current density equal to $\hat{K}_s = 10$ kA/m. The main frequency has been chosen equal to 50 Hz, and various harmonic order ν are considered.

Both models with one and two layers have been considered. Table 2.2 compares the results of the analytical model with the results of the FE computation according to a straight–lined model and a cylindrical model, with concentric layers and diameter $D = 0.5$ m.

Table 2.2: *Comparison between FE (straight–lined and cylindrical models) and analytical computation of the power loss density*

	Model with $y_g = 0$ mm				Model with $y_g = 1$ mm		
	straight–lined		cylindrical		straight–lined		cylindrical
ν	Analytical	FEM	FEM	ν	Analytical	FEM	FEM
1	7024.8	7192.4	7414.9	1	6640.0	6823.9	7095.0
2	7024.7	7196.7	7415.0	2	5616.2	5785.4	6023.8
3	7024.5	7196.5	7415.1	3	4294.5	4435.6	4617.2
4	7024.3	7196.3	7415.1	4	3043.6	3148.3	3269.3
5	7023.9	7196.0	7415.1	5	2065.2	2136.7	2210.3
6	7023.5	7195.6	7415.0	6	1380.6	1427.5	1470.3
7	7023.1	7195.2	7414.8	7	926.8	957.4	982.1
8	7022.6	7194.7	7414.6	8	631.4	651.5	666.0
9	7022.0	7194.1	7414.3	9	438.6	452.1	460.8
10	7021.3	7193.5	7413.9	10	311.1	320.4	325.7

In the comparisons, the losses computed by means of the FE models are always higher than those computed analytically. In particular, cylindrical FE model shows higher losses (about 4%). However the difference between the analytical model and the FE straight–lined model is moderate (lower than 3%). Therefore, the straight–lined model is a good approximation of the cylindrical model (which better approximates an electrical machine), and the analytical computation is a valid alternative to the FE analysis.

Finally, Table 2.2 highlights the effect of the air–gap in reducing the impact of the harmonics of high order on the rotor losses (as said above, there is a "low–pass filter" effect).

2.6 Conclusions

The above considerations highlight that rotor losses are mainly due to the MMF sub–harmonics. Effect of the conductive sheet is taken into account. Adopting a conductive sheet does not reduce the rotor losses when they are caused by low–order harmonics. The impact of using a single– or double–layer winding is also investigated. It has been shown that the PM machines adopting single–layer winding exhibit higher rotor losses.

Finite element approach is used to predict the rotor losses induced by MMF harmonics. There is a reasonable agreement between the results found with FE and with analytical models; general considerations can be pointed out.

CHAPTER 3

An index of rotor losses

Abstract

The aim of this chapter is to define an index of the rotor losses induced by the MMF space harmonics in fractional–slot permanent magnet (PM) machines. Such an index allows a rapid discrimination of the various fractional–slot permanent magnet machines, based on the number of slots and poles.

For the sake of generality, a simple model of the rotor losses is adopted to compute such an index of rotor losses. However, the index behaviour follows that of rotor losses computed by means of more complex models.

Even though some design strategies can be adopted to reduce the PM losses, such as PM segmentation [8,11,30] and choice of appropriate retaining structure [12], the proposed index gives a valid help in the starting design steps.

3.1 Definition of the index

The aim is to define an index of rotor losses, mainly depending on the winding arrangement. As a consequence, such an index allows a rapid comparison of the rotor losses due to the MMF harmonics of fractional–slot PM machines.

The first step is to analyse the total rotor losses. For a given machine, characterized by a fixed combination of slots and poles, the total rotor losses can be computed by means of (1.12) (one–layer model is adopted) summing all the contributions of the MMF harmonics. Then, a sum of the power loss density for all the harmonics has to be considered, which is

$$q_{tot} = \sum_{\nu} \frac{\xi^4}{\sqrt[4]{(\pi^4 + \xi^4)^3}} \frac{1}{\cos(\varphi/2)} \frac{\hat{K}_{s\nu}^2}{4\sigma\tau_\nu} k_{ym} \tag{3.1}$$

where all the terms ξ, φ, τ_ν, $\hat{K}_{s\nu}$, and k_{ym} (see eq. 1.14) are computed for the specific harmonic order ν.

Terms of low influence

Some terms in (3.1) have a low influence in the computation and can be neglected. This is particularly true, when the effective losses are not investigated in details, but a rapid comparison of various machine configurations is carried out, as in this case.

At first, $\cos(\varphi/2)$ ranges from $1/\sqrt{2}$ and 1, as shown in Fig. 1.8a. It is equated to unity in the computation of the index, with a small overestimation of the rotor loss density.

Even k_{ym}, given in (1.14), is a reduction factor of the power loss density that tends towards zero as the ratio τ_ν/y_m tends to infinity. This factor is also equated to unity in the computation of the index. Neglecting this reduction factor, an overestimation of the rotor losses is achieved, especially for the harmonics of high order ν (i.e. with low wavelength τ_ν).

Air–gap effect

The effect of the air–gap on the rotor losses is similar to a "low pass filter": the air–gap has a negligible effect on the sub–harmonics, while it reduces the impact of the high–order harmonics. In other words, increasing the air–gap, the losses due to the sub–harmonics remain almost the same, while the losses due to the harmonics of higher order decrease considerably [12, 13].

For the purpose of including the effect of the air–gap in the simple model adopted for the estimation of the rotor losses, a corrective factor can be used, defined as

$$k_{gap} = k\, e^{-\left(a\frac{g}{D}+b\right)\nu} \tag{3.2}$$

where g is the air–gap and D is the stator diameter. The coefficients k, a, and b are achieved by comparing the losses achieved by means of a straight–lined model with a single medium (using the two–layer model) and the losses achieved by means of a straight–lined model with two media, the first being the air–gap (using the two–layer model).

According to the more commonly used material, some results are

magnet	$k = 1$	$a = 4.2$	$b = 0.00017$
copper	$k = 1.15$	$a = 3.5$	$b = 0.0012$
iron	$k = 1.25$	$a = 15$	$b = 0.040$

They are achieved with g/D in the range 0.002 to 0.01.

Index of rotor losses

It is convenient to express the index as a dimensionless quantity. For this purpose, the total power loss density (3.1) is divided by $\hat{K}_s^2/(\sigma \tau_p)$, where $\hat{K}_s$ and τ_p refer to the main harmonic, of order $\nu = p$. The ratio $\hat{K}_{s\nu}/\hat{K}_s = k_{w\nu}/k_w$, where $k_{w\nu}$ is the winding factor of the harmonic of order ν and k_w is the winding factor of the main harmonic. Since $\tau_p/\tau_\nu = \nu/p$, the index of rotor losses can be defined as

$$I_{rl} = \sum_\nu \frac{\xi^4}{\sqrt[4]{(\xi^4 + \pi^4)^3}} \left(\frac{k_{w\nu}}{k_w}\right)^2 \frac{\nu}{p} k_{gap} \tag{3.3}$$

An evident advantage of such an index of rotor losses (3.3) is its simplicity. For a given combination of slots and poles, it is sufficient to compute the winding factors and the frequency with respect to the rotor of the various harmonics. Then, the specific wavelength ξ is achieved for each harmonic order, k_{gap} from the ratio g/D, and, finally, the index (3.3) is computed.

Examples

Some examples are reported hereafter, referring to some combinations of number of slots and poles. For all comparisons, the linear current density is fixed to be equal to 10 kA/m, and the machine speed to 100 r/min. The straight–lined model with one layer has been adopted. The permanent magnet has been chosen as conductive material with $\sigma = 1$ MS/m and $\mu = 1.05\mu_0$ and the ratio g/D has been fixed to 0.002 (from which $L_x = \pi D$ is computed).

A 24–slot 20–pole machine

The first example refers to a 24–slot 20–pole machine. The corresponding MMF and electric loading harmonic contents are reported in Fig. 3.1a and 3.1b, respectively.

The impact of various harmonics of order ν on the index of rotor losses I_{rl} is shown in Fig. 3.2, with double–layer and single–layer winding arrangement, respectively.

As commented in chapter 1, the harmonic causing the highest rotor losses is the first slot harmonic (i.e. of order $\nu = 14$) and the sub–harmonic (i.e. of order $\nu = 2$) especially with single–layer winding.
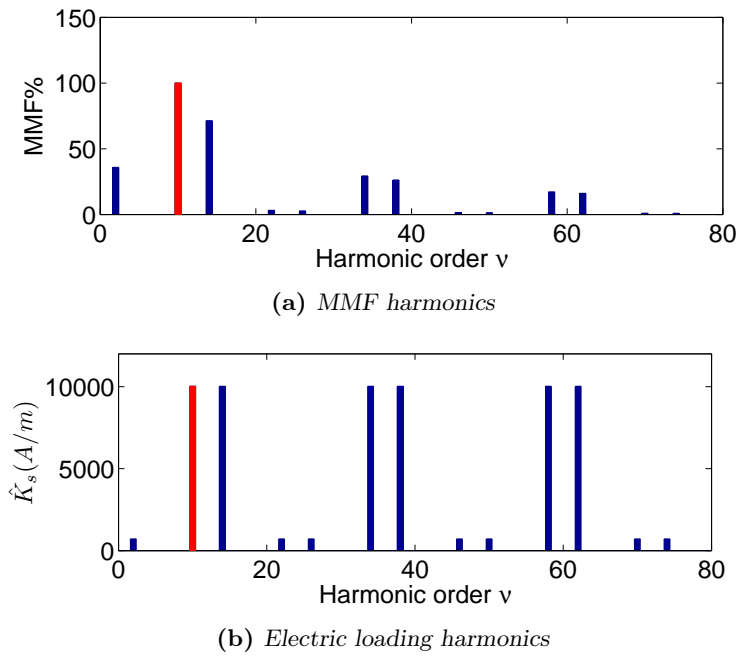
(a) *MMF harmonics*

(b) *Electric loading harmonics*

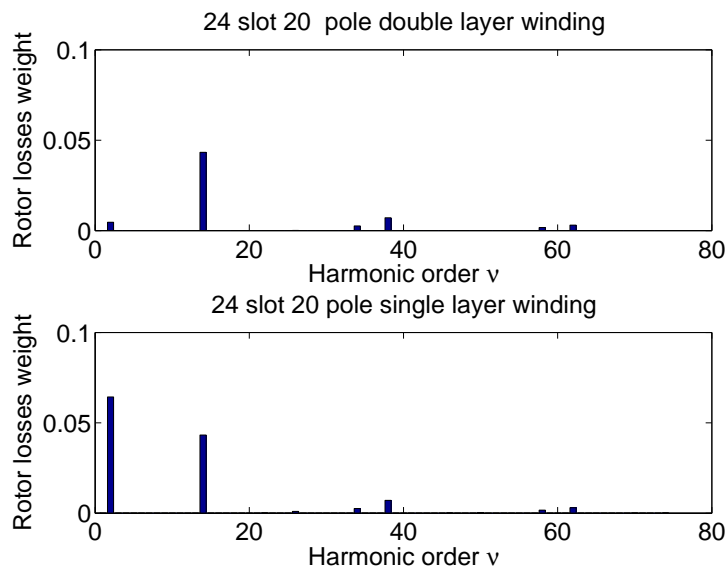**Figure 3.1:** *MMF harmonic (a) and electric loading (b) contents of a 24–slot 20–pole double–layer winding*

Figure 3.2: *Impact of harmonics on the index of rotor losses in a 24–slot 20–pole machine, considering permanent magnet as conductive material.*

A 18–slot 20–pole machine

The second example refers to a 18–slot 20–pole machine. The corresponding electric loading harmonic contents are reported in Fig. 3.3a and 3.3b, for double– and single–layer winding respectively. The impact of various harmonics of order ν on the index of rotor losses I_{rl} is shown in Fig. 3.4.
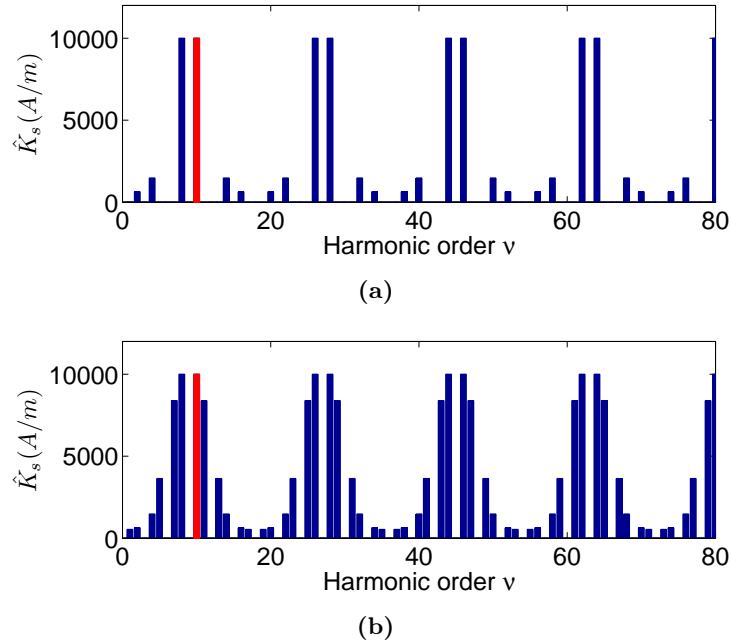

(a)

(b)

Figure 3.3: *Electric loading harmonic contents of a 18–slot 20–pole machine with double–layer (a) and single–layer (b) winding*

Comparison among various slot and pole combinations

The immediate advantage is that the simple model presented above is well suited to compare the rotor losses in machines characterized by different combinations of slot and pole numbers. Since the index of rotor losses is based on the analytical expression (3.3), the comparison among different machine solutions is very rapid.

The following tables report the index of rotor losses computed for a machine with $g/D = 0.002$, rotating at the speed $n = 100$ r/min. Permanent magnet is considered as conductive material. The frequency $f_{r\nu}$ of the various harmonics are computed according to the given speed n and number of pole pairs p.

Table 3.1 and Table 3.2 report the comparison of the index of rotor losses computed for machines with double–layer and single–layer winding, respectively. The index values can be compared with the results sketched in Figs. 1.26 and 1.25. As expected, the lower rotor losses are achieved when integral–slot windings are adopted, i.e. $Q/(2p) = 3$. The rotor losses increase departing from these winding combinations. In addition, local minima exist, according to combination of the number of slots and number of poles.

It is worth noticing that the results reported in Table 3.1 and Table 3.2 are the same of those
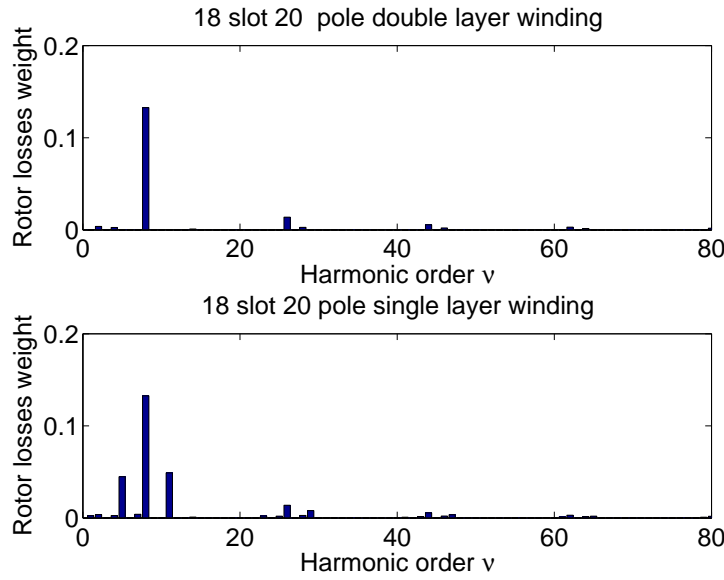
Figure 3.4: *Impact of harmonics on the index of rotor losses in a 18–slot 20–pole machine considering permanent magnet as conductive material.*

achieved in [10, 13], in which a more involved model, with four layers, has been used for the computation of the rotor losses. This confirms the effectiveness of the index of rotor losses, for a rapid comparison among various machine configurations.

Table 3.1: *Index of rotor losses (double–layer winding, magnets)*

2p\Q	120	123	126	129	132	135	138	141	144	147	150
40	**4.0**	5.6	6.5	7.0	8.5	10.1	7.2	5.7	15.8	16.1	13.6
42	——	——	**3.3**	——	——	6.7	——	——	8.1	——	——
44	9.9	10.1	6.8	4.7	**2.8**	4.0	4.8	6.0	5.0	7.4	8.0
46	20.3	14.9	7.9	8.5	5.6	4.0	**2.3**	3.4	4.1	5.2	4.1
48	——	——	17.2	——	——	6.9	——	——	**1.9**	——	——
50	16.5	8.1	7.7	17.6	14.1	10.7	5.9	5.5	4.1	2.9	**1.6**
52	15.1	15.7	12.7	5.5	10.1	16.5	12.0	8.6	5.7	4.5	3.6
54	——	——	——	——	——	——	——	——	——	——	——
56	11.7	12.1	12.4	12.5	13.5	12.3	5.8	5.6	14.2	12.0	9.0
58	10.1	9.9	9.8	11.2	11.4	12.0	12.2	9.5	3.9	7.5	13.4
60	——	——	9.6	——	——	10.3	——	——	11.6	——	——

Table 3.2: *Index of rotor losses (single–layer winding, magnets)*

2p\Q	120	123	126	129	132	135	138	141	144	147	150
40	**4.0**	––	18.8	––	13.6	––	14.1	––	––	––	––
42	––	––	**3.3**	––	––	––	––	––	14.0	––	––
44	16.1	––	19.4	––	**2.8**	––	7.0	––	8.5	––	12.6
46	29.3	––	25.8	––	8.1	––	**2.3**	––	5.9	––	14.1
48	––	––	25.6	––	––	––	––	––	**1.9**	––	––
50	––	––	40.0	––	22.3	––	18.4	––	6.0	––	**1.6**
52	––	––	––	––	44.1	––	19.5	––	9.4	––	5.3
54	––	––	––	––	––	––	––	––	––	––	––
56	––	––	––	––	––	––	––	––	22.5	––	21.9
58	––	––	––	––	––	––	––	––	––	––	36.8
60	––	––	––	––	––	––	––	––	––	––	––

3.2 Conclusions

For a rapid comparison of the effect of the MMF harmonics on the rotor losses of fractional–slot PM machines, an index of rotor losses has been defined. It refers to a simple analytical model, characterized by a single straight–lined conductive material, and linear current density distributions placed along its surface.

Although the model is really simplified, it is useful for a rapid comparison of various machine configurations, i.e. characterized by different combinations of number of slots and number of poles, with both single– and double–layer windings.

Comparing the values of the index with that of the rotor loss density computed by means of more complex models, a good correspondence is found. This confirms that the index of rotor losses is a reasonable parameter to weight the rotor losses in fractional–slot permanent magnet machines.

CHAPTER 4

Impact of rotor losses in a 12–slot 10–pole axial flux PM machine

Abstract

This chapter presents the impact of the rotor losses on the performance of a 12–slot 10–pole axial flux PM machine. The machine was designed to achieve a wide flux weakening range, the detailed design procedure of the machine can be found in [31]. The influence of both MMF harmonics and slot harmonics is considered.

Comparisons between predictions and experimental results are included.

The analytical model presented in the previous chapters is used to predict the rotor losses due to both MMF harmonics and slot openings. Then, experimental results on a specific prototype are presented to compare predictions with measurements.

The prototype is an axial flux machine equipped with three different rotor disks: a disk without PMs, a disk with energized PMs and a disk with de–energized PMs.

4.1 The 12–slot 10–pole MMF harmonic contents

Fig. 4.1 shows the MMF harmonics contents, according to the 12–slot 10–pole machine. Due to the low machine periodicity ($t = 1$), the sub–harmonic of order $\nu = 1$ exists. Then, only harmonics of odd order exist (i.e. $\nu = 5, 7, 11, 13, ...$), adopting both double–layer and single–layer winding. However, the harmonic amplitudes increase in the second case. Thus, as said before, it is expected that rotor losses in machines with single–layer winding are higher than rotor losses in the same machines with double–layer winding.
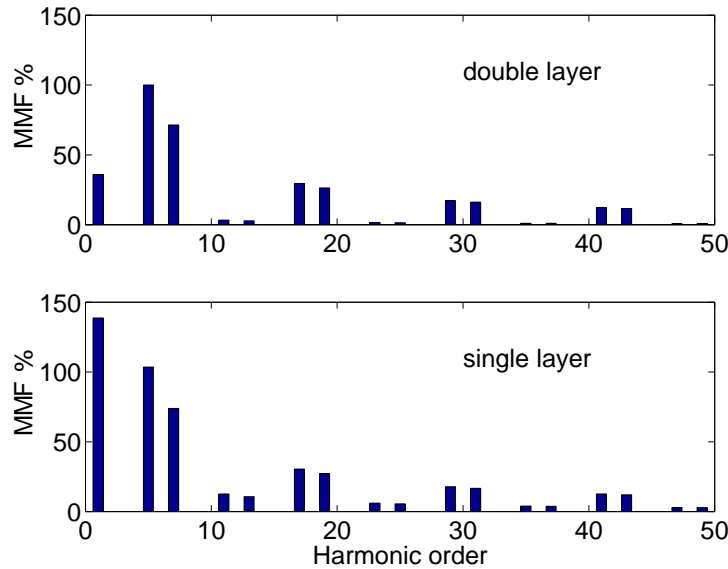

Figure 4.1: *MMF harmonic contents as percentage of the main harmonic ($\nu = 5$) of 12–slot 10–pole motor, with single–layer and double–layer winding.*

4.2 Computation of rotor losses

Both analytical and finite element approaches can be used to predict the rotor losses, caused by the stator MMF harmonics. The analytical computation has the advantage to be very rapid, even though it requires some geometry simplifications (a simplified multi–layer rotor is considered). Then, in a two–dimensional simulation the resistance of the rotor paths is lower than actual values, and the end effects are neglected. On the contrary, the computation using finite elements is not constrained to the rotor geometry, but requires more computation time.

To the aim of highlighting the impact of the stator MMF harmonics, the MMF distribution is split in its harmonic components, using the Fourier series expansion (see Fig. 4.1). The rotor losses are computed separately for harmonics of various orders. Then, they are superimposed to achieve the total losses.

Another source of rotor losses are the slot openings, which produce a decreasing of the permeance corresponding to the stator slots. So that, a variation of the flux density which moves with respect to the rotor is present and hence rotor losses rise when the rotor moves. This contribution to the rotor losses could be significant in machines with open slots.

Computation of rotor losses due to MMF harmonics

A straight–lined model of the machine for the generic radius r is considered (see Fig. 4.2), and then the result is integrated from the inner radius R_i to the outer radius R_e of the AxF machine.
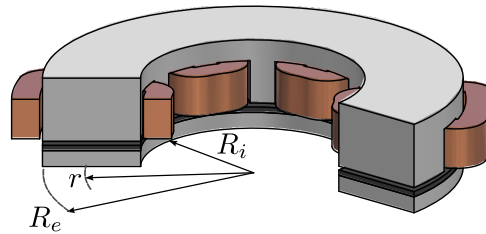

Figure 4.2: *AxF machine before linearization.*

The adopted model was described in chapter 1.

Computation of rotor losses due to slot openings

For the flux density drop estimation in front of the stator slots, both FE simulations and analytical model can be used. In Fig. 4.3 the result of a slot pitch FE simulation is shown.
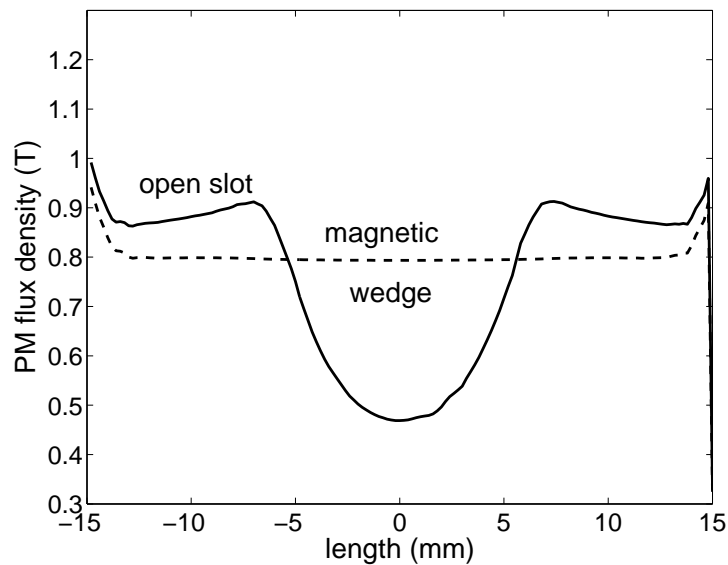

Figure 4.3: *Flux density distribution in the PM in front of the slot. Abscissa is centered on the slot openings. Dashed line: with an open slot. Solid line: with magnetic wedge.*

In the simulation there is no current in the slots, hence the PMs are the only field source. The solid line shows the flux density in the PMs. The flux density drop due to the slot openings is about 0.46 T. In order to reduce the wide flux density variation, magnetic wedges can be used. The PMs flux density when a soft magnetic wedge with relative permeability 500 is introduced

in the slot is shown in Fig. 4.3 with dashed line. Some experimental tests considering magnetic wedges will be presented in the following.

An analytical estimation of the flux density drop is given by

$$\Delta B = \frac{B_{rem}}{1 + \frac{\mu_r\ g}{t_m}} \left(1 - \frac{1}{1 + \frac{\mu_r\ w_s}{2\ (t_m + \mu_r\ g)}} \right) \tag{4.1}$$

where B_{rem} is the PM remanent flux, μ_r the PM relative permeability, t_m the PM thickness, g is the air-gap thickness and w_s is the slot width [29].

It is assumed that the flux density varies sinusoidally. An equivalent current distribution can be used instead of the actual slot openings geometry, so as to reproduce the slot openings effect. From ΔB estimated in (4.1), the peak current of the sine wave current density distribution is computed as:

$$I_{\Delta B} = \frac{\Delta B}{\mu_0} \left(g + \frac{t_m}{\mu_r} \right) \tag{4.2}$$

and the peak value of the corresponding electric loading is:

$$\hat{K}_{\Delta B} = \pi\ \frac{I_{\Delta B}}{p_s} \tag{4.3}$$

where $p_s = \pi/Q_s(R_e + R_i)$ is the average slot pitch. The harmonic order of this distribution is equal to the number of slot, i.e. $\nu = Q_s = 12$. This equivalent current distribution can be used to compute the rotor losses due to the slot openings by means of the model described previously. Comparison between prediction and measurement of rotor losses due to the slot openings will be shown in next sections.

For the considered motor (see Table 4.1), the flux density drop is estimated from (4.1) as $\Delta B = 0.48$ T, very close to the value calculated from the FE simulations (see Fig. 4.3). Then from (4.2)–(4.3) it is $I_{\Delta B} = 1837$ A and $\hat{K}_{\Delta B} = 190$ kA/m.

4.3 Description of the measurement system

This section describes the machine under test, the measurement system and the test methods.

Axial flux motor description

The considered motor is a 1–kW axial flux (AxF) motor with 12 slots and 10 poles. The stator is shown in Fig. 4.4.
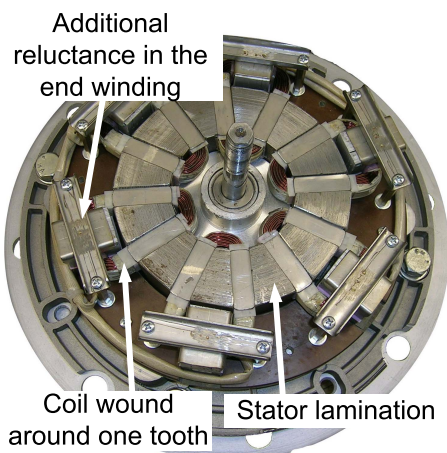

Figure 4.4: *The stator of the AxF motor.*

The main geometrical data are reported in Table 4.1. The motor structure allows an easy adjustment of the parameters, according to the various tests. A rotor disk without PMs can replace easily the actual rotor disk with PMs, in order to distinguish the impact of the slot openings and of the MMF harmonics on the rotor losses. The two rotor disks are shown in Fig. 4.5.
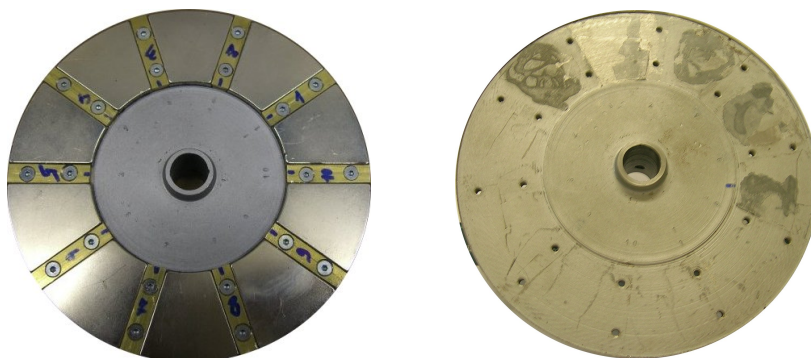

Figure 4.5: *Rotor disk with PMs and without PMs.*

In addition, a rotor disk with de–energized PMs is considered to measure the rotor losses (in the PMs and in the rotor disk) due to the MMF harmonics only.

In the AxF motor prototype, designed for a wide speed operating region, the inductances can be adjusted introducing additional reluctances in the machine end winding [31]. The six addi-

**Table 4.1:** *Main geometrical data of the motor.*

R_e	$= 75$ mm	outer radius
R_i	$= 40$ mm	inner radius
h_r	$= 35$ mm	difference between radii
h_s	$= 21$ (16) mm	slot height (available)
w_s	$= 12$ mm	slot width
h_{bi}	$= 24$ mm	back iron height
Q_s	$= 12$	number of slots
w_{sp}	$= 8$ mm	aluminum separator width
B_{rem}	$= 1.1$ T	remanent magnetization
μ_r	$= 1.05$	permeability
g	$= 1$ mm	air-gap
t_m	$= 4$ mm	permanent magnet thickness
$2\alpha_m$	$= 70$ deg	permanent magnets width

tional reluctances are recognizable in Fig. 4.4. A high inductance filters the current harmonics so that the resulting current is very close to a sinusoidal waveform.

The motor currents are controlled by an inverter. A control algorithm has been implemented so as to perform various specific tests on the motor to identify its rotor losses. Depending on the test, the $d-$ or $q-$axis current references are imposed and the currents controlled through current loops.

Measurement system

Fig. 4.6 shows a picture of the test bench.
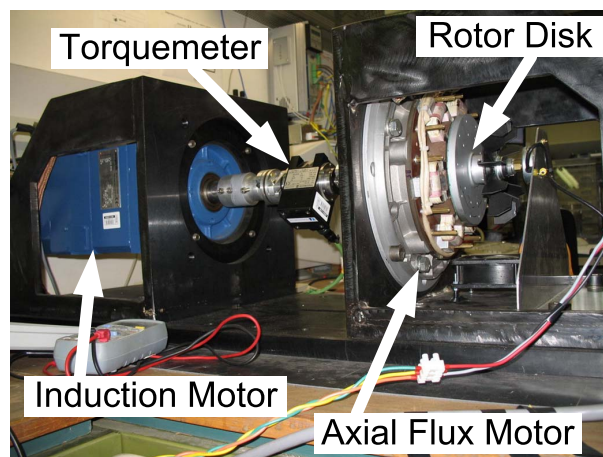
Figure 4.6: *The test bench used for the tests.*

It is composed by an induction motor that can be operated in speed control mode, a torque–meter and the AxF motor prototype.

The layout of the measurement system is shown in Fig. 4.7. For any fixed speed, the current I, the voltage V and the input electrical power P_1 are measured. In addition, the input mechanical power P_2 is measured by means of the torque–meter. In Fig. 4.7, the machine losses are highlighted: P_{Js} are the stator Joule losses, P_{Fe} are the stator iron losses, P_{mech} are the mechanical losses due to the friction and ventilation, and P_{rl} are the rotor losses due to the induced currents.

The machine power balance yields:

$$P_1 + P_2 = P_{Js} + P_{Fe} + P_{mech} + P_{rl} \tag{4.4}$$

On the left hand side of (4.4) there are the measured powers. On the right hand side there are the motor losses. The stator Joule losses are estimated as $P_{Js} = 3RI^2$. The stator losses are corrected according to the measured temperature rise in the stator winding. The stator iron losses P_{Fe} are estimated using search coils in the teeth and in the back iron (see following sections). The mechanical losses P_{mech} are measured dragging the rotor disk (see following sections). From the power balance (4.4) it is possible to estimate the rotor losses P_{rl}. Rotor losses are computed as difference, and so they can be affected by error.
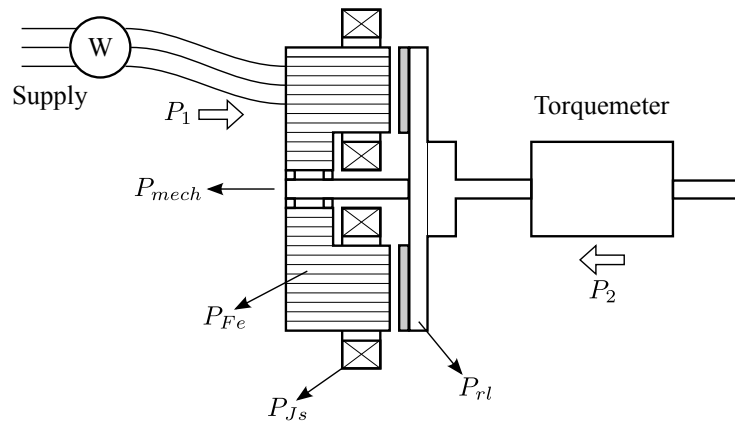

Figure 4.7: *The layout of the test bench.*

4.4 Experimental results

Stator iron losses

The flux density in the stator back iron and stator teeth are measured during all tests. The flux density in the stator back iron is achieved by means of a search coil mounted on the AxF machine stator. The flux density in the teeth is achieved by using the phase coil, since each tooth is wound by one coil (see Fig. 4.4).

The voltages measured during each test in the search coil and in the phase coil are integrated so as to achieve the magnetic flux in the iron. From that, the flux density is obtained and, finally, the iron losses are computed adjusting the specific losses according to the operating frequency.

Mechanical losses estimation

The basic idea to measure the mechanical losses P_{mech} is to drag the rotor, measuring the input mechanical power P_2 by means of the torque–meter.

The considered prototype is a single–sided AxF machine, and due to the axial magnetic pull, the force on the bearing when the magnets are present is significantly larger than the force when the magnets are removed. For this reason, it is not possible to measure the mechanical losses removing the PMs.

However, if the PMs are included in the rotor, the interaction between the slot openings and the PMs flux gives rise to significant rotor losses (see the following sections), making difficult, if not impossible, to estimate the mechanical losses.

Therefore, the following solution has been adopted to measure the proper mechanical losses: the stator of the machine prototype has been mounted with the slots in the direction opposite to the airgap (as shown in Fig. 4.8), so that the rotor PMs are in front of the smooth stator yoke.
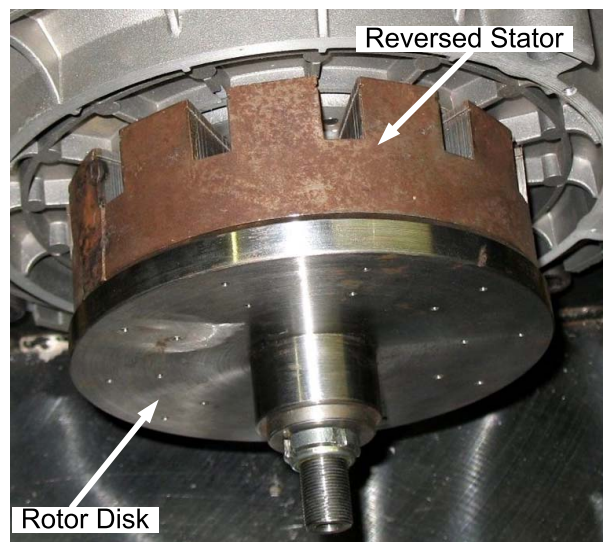

Figure 4.8: *The PM rotor and the reversed–mounted stator for testing the mechanical losses.*

In this way, the power P_2 measured by the torque–meter during a dragged test approximates the mechanical losses P_{mech}, since the stator iron losses are negligible. In fact, the stator is laminated and the stator flux density is very low (see measurements of stator back iron flux density reported in Fig. 4.9).

The measured mechanical losses P_{mech} with the reversed–mounted stator are reported in Fig. 4.10 using square–marked line. It is assumed that the behaviour of these losses with the speed remains the same during any following test.
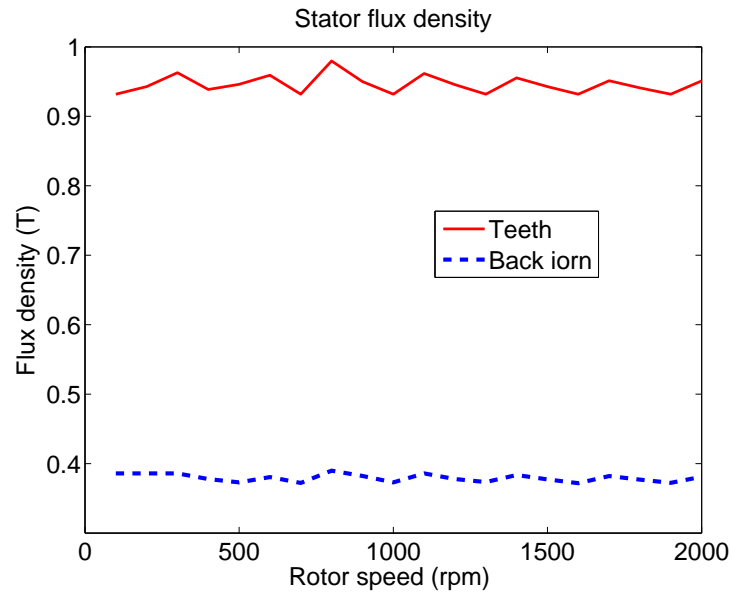
Figure 4.9: *Peak value of the flux density in the stator back iron and in the teeth measured by means of search coils.*
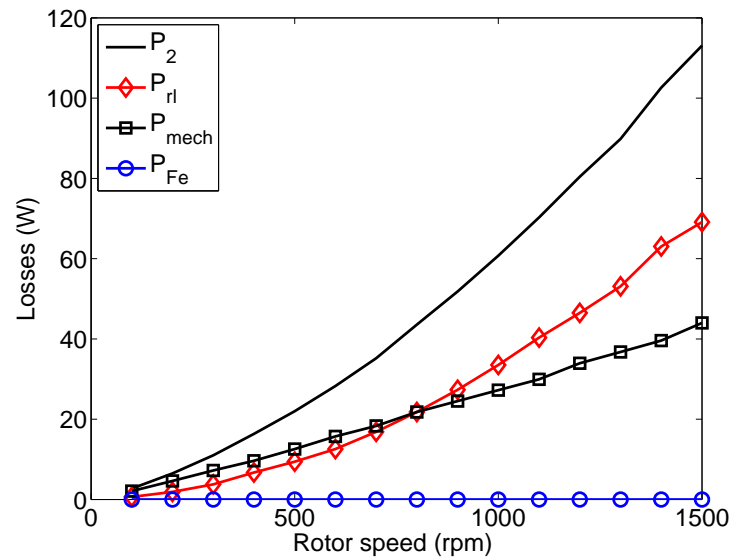

Figure 4.10: *AxF machine losses versus rotor speed, during the dragged test without currents in the stator (experimental tests).*

Dragged rotor test (without currents)

In this test, the rotor disk with the PMs is adopted. The motor is dragged with no current in the stator winding thus $P_1 = 0$ and the power balance (4.4) becomes $P_2 = P_{Fe} + P_{mech} + P_{rl}$. The rotor losses are due to the variation of slot permeance encountered by the PM flux.

The input mechanical power P_2 has been measured by the torque-meter as the mechanical power to run the disk. It is shown using solid line in Fig. 4.10.

**Table 4.2:** *Material properties used in the analytical model.*

Region	I	II	III	IV
Material	Air	PMs	Iron	Air
σ (S/m)	0	0.7	10	0
μ_r $(-)$	1	1.05	10000	1
Dimensions (mm)	1	4	10	60

The mechanical losses P_{mech} are shown using square–marked line in Fig. 4.10. The stator iron losses P_{Fe} are estimated using the flux density measured by means of search coils as explained above, and they are reported with the circle–marked curve in Fig. 4.10. In Fig. 4.9 the measured flux density in the stator teeth and stator back iron during this test are reported. The contribution of stator iron losses to the total losses is negligible in the prototype under test.

Then, the rotor losses are computed as $P_{rl} = P_2 - P_{Fe} - P_{mech}$. They are reported using diamond–marked curve in Fig. 4.10. As could be noted, the rotor losses increase almost quadratically with the speed and are the predominant contribution to the total losses at no load.

The rotor losses during the dragged rotor test are also computed analytically. The parameters of the model are reported in Table 4.2, and are considered the same in all the computations of this chapter. Although they might be variable (depending on the operating conditions, e.g. temperature, rotor-to-stator attractive force, etc.), it was preferred to keep them constant.

In Fig. 4.11 the measured rotor losses (diamond–marked curve of Fig. 4.10) are reported together with the analytical prediction.
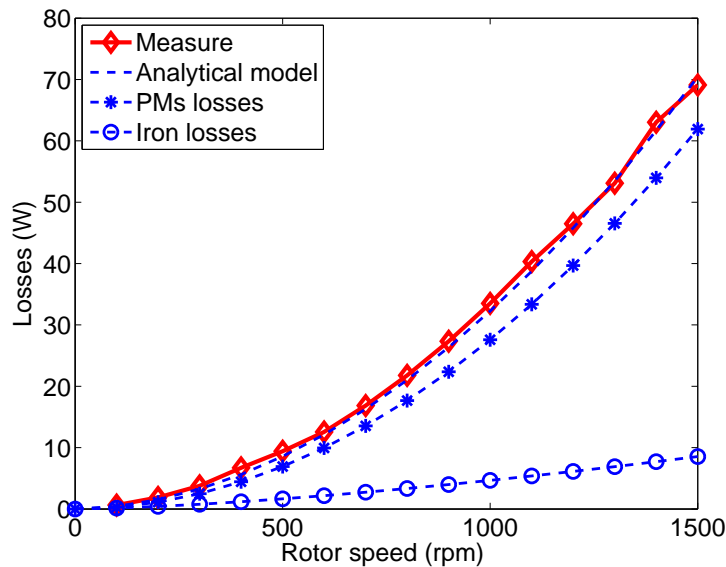
Figure 4.11: *Rotor losses versus speed with PMs and no stator currents: comparison between measurements (solid line) and predictions (dashed lines).*

A very good agreement can be noted. From the analytical model, information about the localization of the rotor losses can be achieved. As shown in Fig. 4.11, the losses are localized both in PMs and rotor disk. However, the amount of loss in the PMs is higher.

This suggests the necessity to segment the PMs in the rotor [8].

In order to reduce the losses due to the slot openings, magnetic wedges can be adopted to close the slots [32]. Fig. 4.12 shows the rotor losses with two different types of magnetic wedges. Both soft magnetic composite wedge with relative permeability equal to 500, and fiberglass–iron
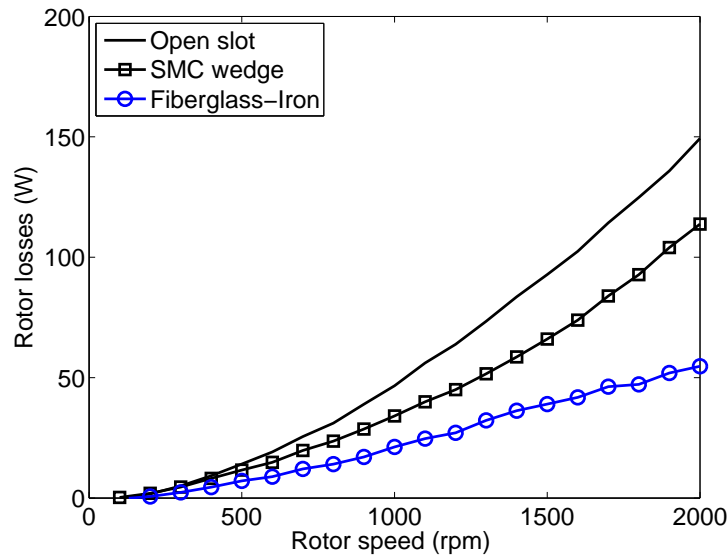

Figure 4.12: *Rotor losses of the AxF motor with PMs and no stator currents. Comparison using wedges of different material (experimental tests).*

magnetic wedge with relative permeability equal to 20 are tested. Always the losses decrease closing the slot. From the results reported in Fig. 4.12, it is worth noticing that the rotor losses with SMC magnetic wedges are higher. Therefore, in this case the wedges with higher permeability seems not to be better for reducing the rotor losses due to the slot openings.

It is worth noticing that, when magnetic wedges are adopted, a portion of the PM flux goes through the wedges themselves. During the rotor movement the flux variation causes losses in the wedges. However, it is not possible to separate these losses from the rotor losses, so that they are included as a rotor loss part in Fig. 4.12.

Dragged rotor test (with dc currents)

Further tests have been carried out, feeding the AxF motor by a dc current, so as to reproduce a particular time instant of the ac current supply. In particular, the coils of the phase a have been series connected with the parallel of the phases b and c. A 6–A current has been supplied in the phase a and then 3–A current, with opposite direction, is supplied in phases b and c.

The rotors with de–energized PMs and without PMs have been adopted in these tests. Therefore, there is no influence of the slot openings and only the MMF harmonics (including the main harmonic) cause rotor losses.

The rotor has been dragged at different speeds, measuring the power P_1 and P_2. In these tests, the power P_1 corresponds to the Joule losses P_{Js} in the stator winding, and the power P_2 corresponds to the sum of stator iron, mechanical and rotor losses. Due to the dc current, the stator iron losses are negligible.

Fig. 4.13 shows the rotor losses referring to the rotor disk without PMs. The measured rotor losses are compared with those predicted by the analytical model, achieving a satisfactory agreement.
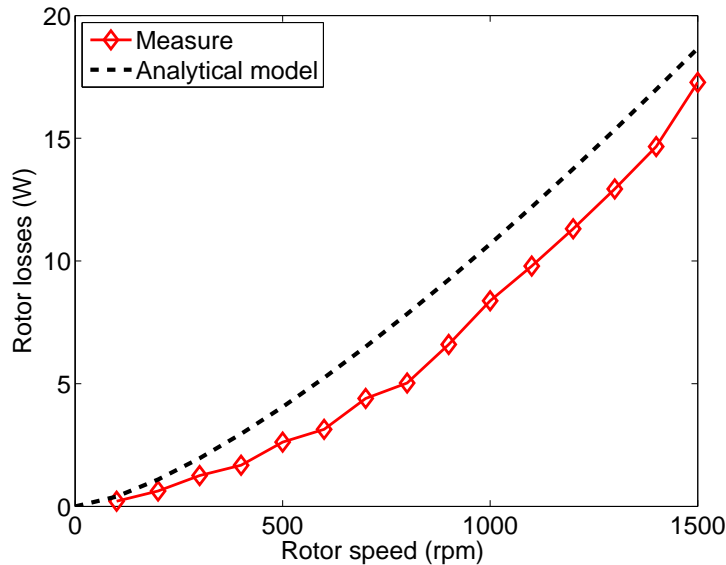

Figure 4.13: *Rotor losses in the rotor disk (without PMs) dragging the rotor, and imposing a dc current in the stator winding. Prediction and measure comparison.*

Fig. 4.14 shows the rotor losses referring to the rotor disk with de–energized PMs. Also in this case, there is a satisfactory agreement between predictions and measurements. Fig. 4.14 also shows the two components of the rotor losses: in the PMs (the higher losses) and in the iron disk.

Rotor losses in the iron disk due to MMF harmonics (without PMs)

For these tests, the PMs are removed from the rotor disk. Thus, only the losses in the iron disk due to the MMF harmonics are considered. For any fixed rotor speed, the current control imposes that the main MMF harmonic is rotating synchronously with the rotor. Thus, all MMF harmonics, except the main harmonic, induce currents in the rotor disk. The nominal current, equal to 8 A (peak value), is imposed during the test by the inverter. The corresponding Joule losses are then constant. Such a current corresponds to the torque of 10 Nm in normal conditions [31].

The rotor losses resulting from the measurements are reported in Fig. 4.15 using diamond–marked curve. As expected, rotor losses P_{rl} increase with the rotor speed as the MMF harmonic frequency increases. They increase quite linearly with the rotor speed.
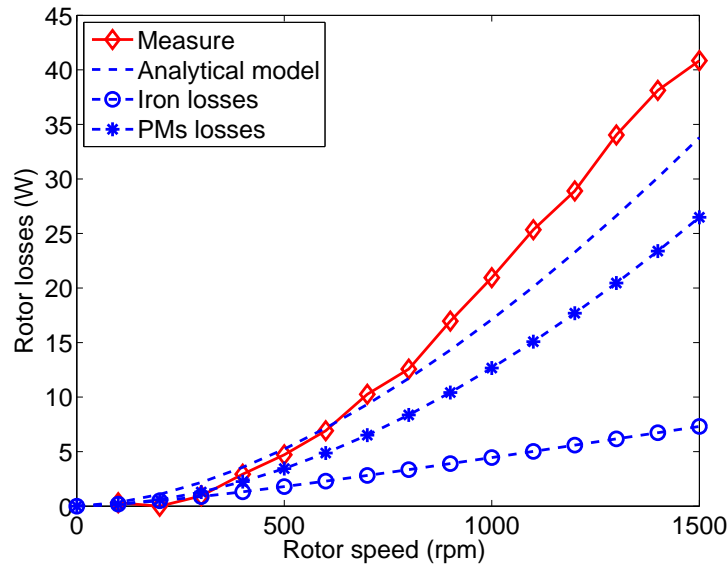
Figure 4.14: *Rotor losses in the rotor disk with de–energized PMs, dragging the rotor, and imposing a dc current in the stator winding. Prediction and measurement comparison. The two loss contributions in iron disk and in PMs are also shown.*
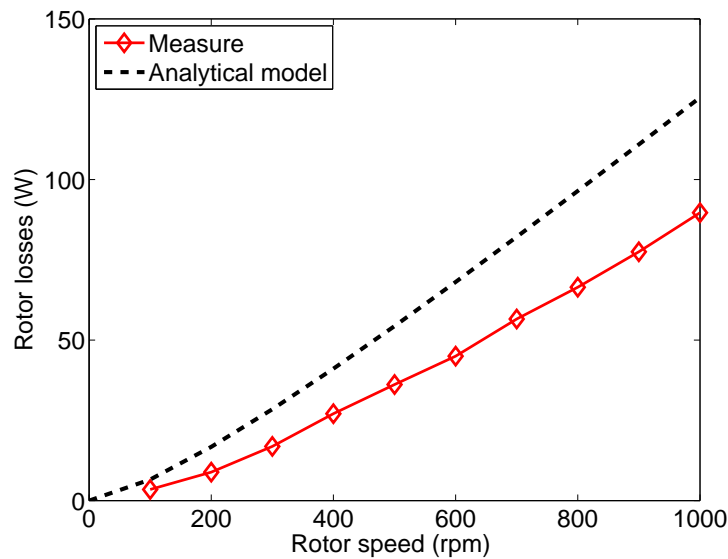

Figure 4.15: *Rotor losses due to MMF harmonics analytically predicted (dashed line) and measured (solid diamond–marked line). Without PMs, the rotor losses are only in the iron disk.*

The four–layer model described in Chapter 1 is used to compute analytically the rotor losses with this machine configuration. The model parameters are as reported in Table 4.2. For this special case, in Region II air data have been adopted, the PM being removed. In Fig. 4.15 the measured rotor losses are compared with the model prediction.

There is a satisfactory match between measurements and predictions at low speed. As the speed increases, a difference between measurements and predictions increases as well, showing that there is an overestimation of the rotor losses. This can be explained as follows.

The model is a 2–D straight–lined model. The current lines are assumed to be only in one direction. Thus, the current path in the rotor disk results shorter than the actual path, yielding a lower resistance and a higher loss prediction. Another aspect that has to be considered is the large airgap that results after removing the PMs (the actual airgap is $t_m + g = 5$ mm).

Due to the flux lines at the edges of the disk, the assumption of the 2–D model to have straight flux lines is not completely verified. Finally, the conductivity and the permeability of the rotor iron is assumed to be constant in the model, while it is reasonable that it may change when eddy currents are induced on the disk surface.

Total rotor losses due to MMF harmonics

In this subsection, the rotor losses due to the MMF harmonics are investigated. To this purpose, the rotor disk with de-energized PMs is used so as to avoid the PM losses due to the slot openings. The rotor is dragged at different speeds and the stator currents are imposed by the drive so that the main MMF harmonic moves synchronously with the rotor disk. As in the previous tests, the rotor losses are computed from the power balance (4.4).

The results are reported in Fig. 4.16, according to a stator current of 8 A (peak value).
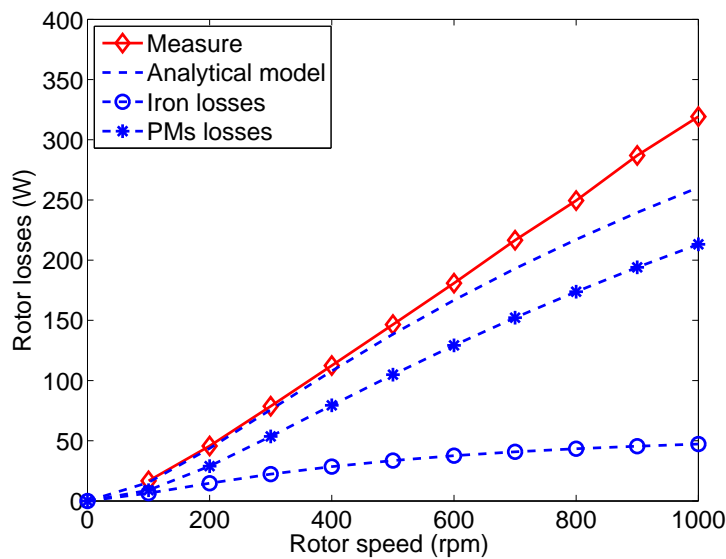

Figure 4.16: *Rotor losses due to MMF harmonics analytically predicted (dashed lines) and measured (solid diamond–marked line). From the analytical model, both contributions of the rotor losses are computed: in the iron disk (circle–marked line) and in the PMs (star–marked line).*

The analytical model predictions are reported using dashed lines. Using the analytical model, it is possible to separate the losses contributions in the PMs and in the rotor disk. The star–marked line refers to the PMs losses, the circle–marked line refers to the iron disk losses and

the total rotor losses are drawn using dashed line. The measured losses are reported with solid diamond–marked line.

The predicted rotor losses result in a satisfactory agreement with the measured losses. It is observed that the higher losses are in the PM, in agreement with the results obtained in Fig. 4.11 and in Fig. 4.14.

Since the measured rotor losses are slightly higher than the predicted ones, it means that the actual PM losses are higher than the analytical model estimation. Therefore, although the analytical model gives a quick estimation of the losses induced in the rotor, it must be kept in mind that there is a slight underestimation of the PM rotor losses.

It is worth noticed (see Fig. 4.14 and Fig. 4.16) that the higher rotor losses take place in the tests with ac currents, in which the main harmonic is synchronous with the rotor. This is due to the different speeds of the MMF harmonics with respect to the rotor. When dc current is considered (Fig. 4.14), all the MMF harmonics have the same speed with respect to the rotor. When ac current is considered (Fig. 4.16), all MMF harmonics but the main harmonic have different speed with respect to the rotor according to (1.4). Among the others, the subharmonic of order $\nu = 1$ (the fundamental harmonic) shows a high amplitude (see Fig. 4.1) and rotates at a speed six time the synchronous speed [33]. This subharmonic causes the highest rotor losses contribution and can be verified by means of the analytical model that considering ac current (i.e., with the main MMF harmonic synchronous with the rotor):

- the rotor losses caused by the subharmonic $\nu = 1$ are the 80% of the total losses at 1000 rpm.

- the rotor losses caused by the subharmonic $\nu = 1$ are 4.5 times higher than the rotor losses with dc current supply due to the same subharmonic with the same current, and rotor speed 1000 rpm.

4.5 Conclusions

This chapter deals with the impact of the rotor losses on the performance of a 12–slot 10–pole axial flux machine. Both the PM flux variation due to the slot openings and the armature MMF harmonics have been considered as sources of the rotor losses.

For the axial flux machine prototype, different rotors have been designed: with PMs, without PMs, and with de–energized PMs, allowing the various loss contributions to be measured independently. In addition, wedges of different materials have been adopted in the stator slots. The tests carried out on the prototype and reported in this chapter highlight the high contribution of both slot openings and MMF harmonics to the total rotor losses.

An analytical model has been used to compute the rotor losses. The prediction achieved by the analytical model has been experimentally proved. Then, the analytical model has been used for weighting the rotor losses in the various rotor parts: PMs and iron disk. In the PMs, the higher rotor losses have been found.

In the aforementioned prototype, running at the rated speed, the total rotor losses are the dominant losses of the machine. This means that the computation of these losses can not be omitted in the design process of fractional–slot PM machines, especially with opened slots.

CHAPTER 5

Multiphase Systems

Abstract

This chapter compares the post–fault current control strategies of a five–phase permanent magnet motor adopting a half–bridge and a full–bridge converter. The analysis covers both the open circuit of one and two phases.

It is shown that the adoption of the full–bridge converter allows to overcome the constraint of having a zero sum of the currents and this is particularly advantageous under the fault of two phases. It is also verified that it is possible to achieve a smooth and adequately high torque in case of fault.

The analytical model used to investigate the properties of each post-fault strategy yields more general results that can be applied to any five–phase PM motor [34]. The analytical model, developed for the five–phase motor drive, allows to identified easily the proper current control strategies.

The experimental results validate the theoretical predictions.

5.1 Five–phase motor prototypes

The experimental results described later refer to a 5–phase 20–slot 18–pole motor prototype. A special stator lamination has been used, to get a number of slots Q multiple of 5. The external diameter is 120 mm and the stack length is 50 mm. Two stators have been manufactured. The first one is characterized by a double–layer fractional–slot winding with unity coil throw shown on the left hand side of Fig. 5.1. It is designed by means of the star of slots [27] as sketched in Fig. 5.3a.
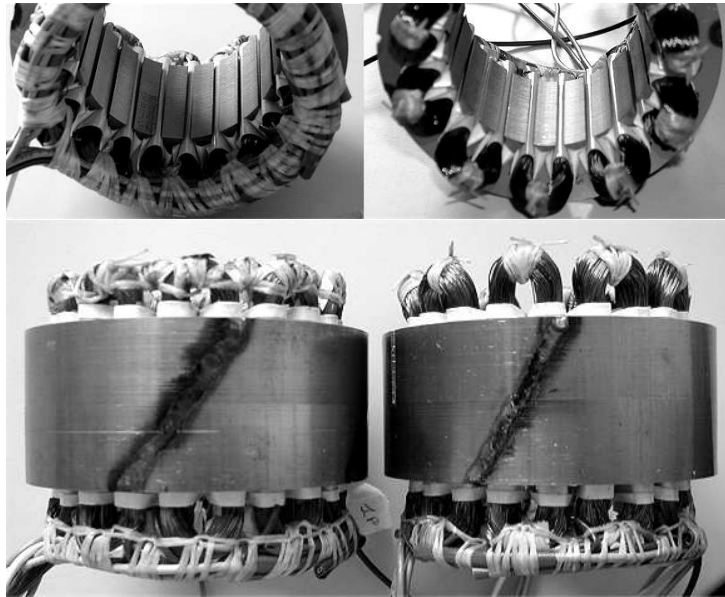

Figure 5.1: *A 5–phase 20–slot stator with double–layer and single–layer winding*
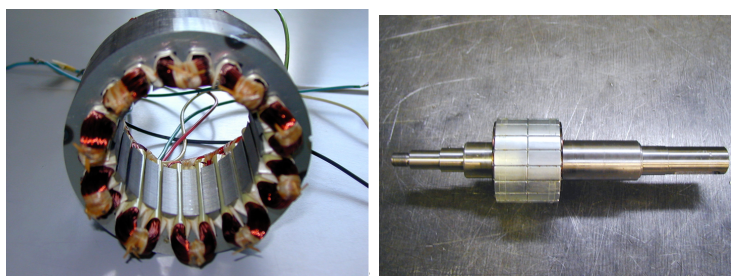

Figure 5.2: *Photo of the stator (left) and rotor (right) of the the five-phase PM machine.*

The combination of the number of poles and slots has been chosen so as to minimize the cogging torque and the torque ripple, as well as to reduce the mutual coupling among the phases. Coils in slot 1, 12, 11, 2 are connected together for the a- phase (see sectors highlighted by dashed lines). The other phases connections are obtained in a similar way, with a $2\pi/5$ angular displacement. From star of slots the winding distribution factors are $k_{d1} = 0.988$ and

$k_{d3} = 0.891$ for the main and third harmonic respectively. The pitch factors are $k_{p1} = 0.988$ and $k_{p3} = 0.891$, so that the winding factor are $k_{w1} = 0.976$ and $k_{w3} = 0.794$ respectively. Among the others, the configuration with $Q = 20$ $2p = 18$ exhibits the minimum MMF contents and thus the minimum torque ripple [35].

The right hand side of Fig. 5.1 shows the stator with a single–layer winding, which is an alternative to the left–hand one. In the single–layer winding each slot contains only coil sides of the same phase [3] as shown in Fig. 5.3b. This winding type reduces the physical contact between phases. Advantages and drawbacks are described in [36] and [37].

20–slot 18–pole motors feature only odd–order harmonics in the air–gap MMF distribution. In addition, the phases are almost completely decoupled. The PM flux–linkage is $\Lambda_m = 0.203$ Vs, self inductance is $L_a = 61.930$ mH, mutual inductances are $M_{ba} = 0.002$ mH and $M_{ca} = 0.011$ mH between adjacent and non–adjacent phases respectively. The phase resistance is $R = 24.6$ Ω at 25^oC ($R = 32$ Ω at 100^oC).

The nominal current is $\hat{I}_n = 0.85$ A (peak value) and the nominal torque is slightly lower than 6 Nm.

(a)

(b)

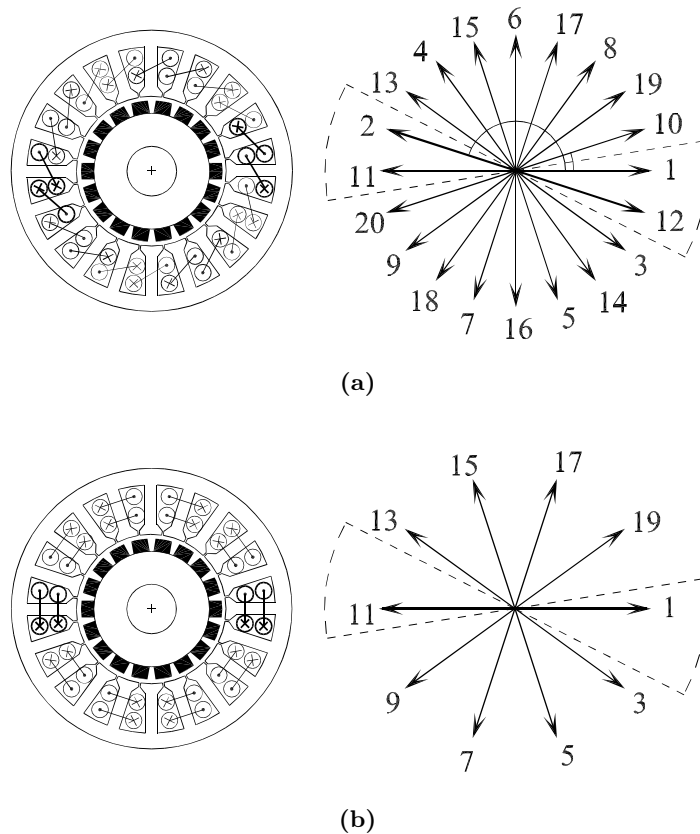**Figure 5.3:** *5–phase 20–slot 18–pole PM motor with* (a) *double– and* (b) *single–layer winding* [3]

The PM flux–linkage of the prototype is $\Lambda_m = 0.292$ Vs, self inductance is $L_a = 47$ mH, mutual inductances are $M_{ba} = 0.002$ mH and $M_{ca} = 0.011$ mH between adjacent and non–adjacent phases respectively. The phase resistance is $R = 24.6$ Ω at 25^oC ($R = 32$ Ω at 100^oC).

Nominal current is $\hat{I} = 0.85$ A (peak value) and the nominal torque is slightly greater than 5.5 Nm.

The full–bridge vs. half–bridge converter

The motor is supplied by both half–bridge and full–bridge converter, (Fig. 5.4), which allows some limitations to the current control to be removed, increasing the performance of the motor drive during post–fault operations.
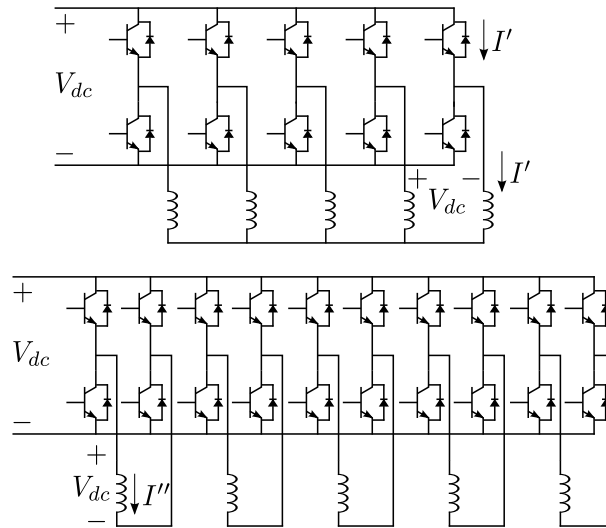

Figure 5.4: *The 5–phase half–bridge and full–bridge converters*

Infact, for the purpose of limiting the electrical interaction, the phases have to be supplied separately. Both the terminals of each phase are brought out to the motor and each phase is supplied by a full–bridge converter. The advantage of this solution is the high partitioning among the phases: the motor drive can operate even with a short–circuited phase, since it is no longer supplied by the corresponding bridge of the converter [38]. Let us refer to the same output motor power P_{out}. In the first solution the rms phase voltage is $E = V_{dc}/(\sqrt{2}(2\sin(2\pi/5)))$, while in the second solution it is $E = V_{dc}/\sqrt{2}$. As a consequence, according to a loss-less system and unity power factor, the rms current results $I' = (\sqrt{2}(2\sin(2\pi/5)))P_{out}/(5V_{dc})$ in the first case and $I'' = \sqrt{2}P_{out}/(5V_{dc})$ in the second case. It results that the Volt–Amps rating (given by the product of rated current by dc voltage and by the switch numbers) of the full–bridge converter is about 105 % the Volt–Amps rating of the half–bridge one.

Motor model

The model is based on the main assumptions of negligible motor losses and mutual coupling between phases to be zero even in presence of iron saturation. Then, each phase is considered individually, and the superposition of the effect is applied, as in [36].

The mth phase current (m defines the generic phase) can be expressed as

$$i_m(t) = \hat{I} \cos(\varphi_m + \alpha_i^e) \tag{5.1}$$

where $\varphi_m = \omega t - k_m 2\pi/5$, α_i^e is the current phase ($\alpha_i^e = 0$ means that the stator current vector is along the d–axis of the synchronous reference frame, $\alpha_i^e = \pi/2$ means that the stator current vector is along the q–axis), with $k_a = 0$, $k_b = 1$, $k_c = 2$, $k_d = 3$, $k_e = 4$. The motor torque can be written as

$$\tau(t) = -\sum_m \sum_\nu T_\nu \sin(\nu \varphi_m) \cos(\varphi_m + \alpha_i^e) \tag{5.2}$$

where T_ν are torque harmonics. For the prototype under test, the first three terms are $T_1 = 2.346$ Nm, $T_3 = -0.330$ Nm, $T_5 = 0.041$ Nm, and they are obtained by finite element simulations.

5.2 Torque developed before fault (healthy mode)

In healthy mode, the currents can be expressed as in (5.1), and the torque results as in (5.2). In healthy mode, only torque harmonics of order $\nu = 1 + 10k$ with $k = 0, \pm 1, \pm 2, ...$ (i.e. $\nu = 1, 9, 11, 19, 21, ...$) are different from zero [26].

Fig. 5.5 shows the measured torque behaviour vs. mechanical angle under healthy conditions. Comparing the measured torque with that obtained by the analytical model, (using (5.2) for the torque computation) a good agreement is obtained for the average torque, which results slightly higher than 5.5 Nm, as expected. On the contrary, the torque ripple (mainly due to the cogging torque) results to be slightly higher, probably due to the manufacturing process.
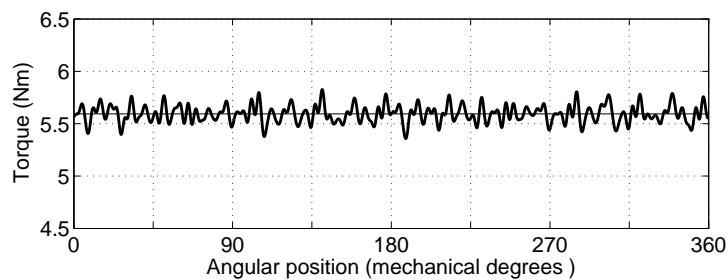

Figure 5.5: *Measured torque behaviours in healthy mode operation*

5.3 Torque developed after fault

At the occurrence of a fault, the current control strategy is modified so as to enable a smooth running also under faulty operations. Differently from [39] and [36], a smooth torque after fault is sought, accepting a decrease in the average torque. Only fundamental and, at most, third time–harmonics of current are computed analytically, without any numerical optimization and any look–up table [40].

The currents are modified with respect to (5.1). Fig. 5.6 refers to the complex representation in the event of the open circuit fault of phase a.
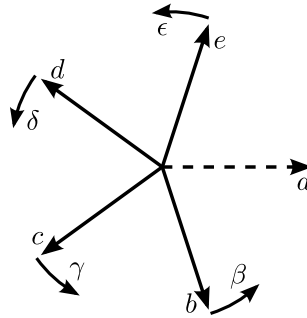

Figure 5.6: *Current vector diagram in the event of open circuit fault of a– phase*

The remaining phases are rotated (the displacement is with respect the healthy operating conditions) according to the angles β, γ, δ, ϵ for the b, c, d, and e phase respectively, i.e.:

$$
\begin{aligned}
i_b &= \hat{I} \cos(\varphi_b + \alpha_i^e + \beta) \\
i_c &= \hat{I} \cos(\varphi_c + \alpha_i^e + \gamma) \\
i_d &= \hat{I} \cos(\varphi_d + \alpha_i^e + \delta) \\
i_e &= \hat{I} \cos(\varphi_e + \alpha_i^e + \epsilon)
\end{aligned}
\tag{5.3}
$$

To the aim of further reducing the torque ripple (i.e. of eliminating the second and the fourth harmonic of the torque), current harmonics of third–order can be injected, as

$$
\begin{aligned}
i_{b3} &= \iota \hat{I} \cos 3(\varphi_b + \alpha_{i3}^e + \beta_3) \\
i_{c3} &= \iota \hat{I} \cos 3(\varphi_c + \alpha_{i3}^e + \gamma_3) \\
i_{d3} &= \iota \hat{I} \cos 3(\varphi_d + \alpha_{i3}^e + \delta_3) \\
i_{e3} &= \iota \hat{I} \cos 3(\varphi_e + \alpha_{i3}^e + \epsilon_3)
\end{aligned}
\tag{5.4}
$$

where ι refers to the ratio between the fundamental current and the third–order current harmonic, $\iota = \hat{I}_3/\hat{I}$. In the analytical model it is assumed that $\alpha_{i3}^e = \alpha_i^e$ and $\beta_3 = \beta$, $\gamma_3 = \gamma$, $\delta_3 = \delta$, and $\epsilon_3 = \epsilon$.

One–phase open circuit fault

Let us assume that the a–phase is permanently open so that $i_a = 0$. Since the motor phases are not mutually coupled, the superposition of the effect can be applied for the torque computation. Therefore, the torque under faulty operation is obtained by subtracting the torque due to the phase a only, say $\tau_a(t)$, from the torque under healthy conditions, given in (5.2).

Since the torque $\tau_a(t)$ contains both average and oscillating terms, a reduction of the average torque is expected of about 20 % together with a peak–to–peak ripple of 50 % with respect to the average value.

In post–fault operations, the current amplitude in the healthy phases is the same. In addition, for reason of symmetry, the current vectors have to be symmetric with respect to the faulty phase, yielding $\epsilon = -\beta$ and $\delta = -\gamma$, [34].

Using the half–bridge converter

When a half–bridge converter is adopted, the additional constraint that the sum of the currents is equal to zero ($\sum i = 0$) has to be fixed, so as to avoid any zero–sequence currents. Such a constraint implies that $\beta + \gamma = \pi/5$. As far as the smooth torque is concerned, the best result has been found with $\beta = 0.577$ rad (i.e. 33.06 deg). The computed torque, under this current control strategy, exhibits an average value of about 73.5 % of the nominal torque with a peak–to–peak torque ripple of 20 %.

In addition, a third time–harmonic of current can be injected so as to achieve a smoother torque. According to the prototype under study the final solution [34] is represented in Fig. 5.7. From the analytical model, the resulting average torque is about 74 % of the nominal torque, and the peak–to–peak torque ripple remains limited to 1.5 %.
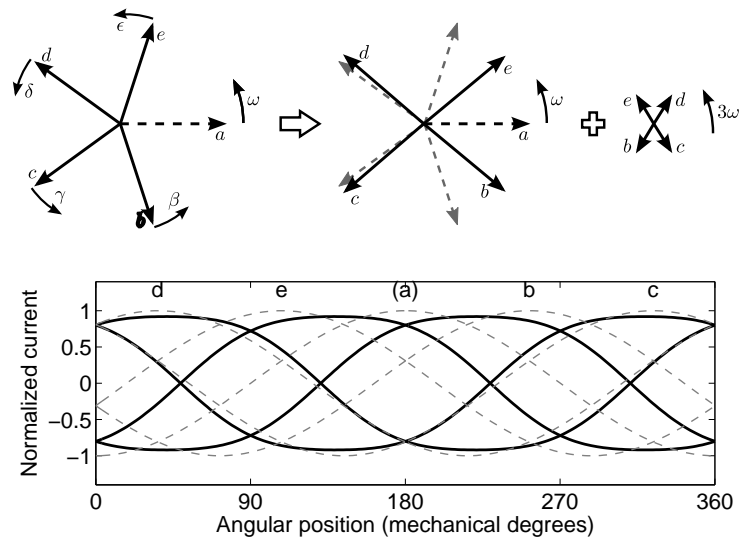

Figure 5.7: *Current vectors with $\beta = -\epsilon = 31.28$ degrees and $\iota = 0.0807$, therefore $\gamma = -\delta = 4.72$ degrees and corresponding waveforms*

Using the full–bridge converter

Adopting the full–bridge converter, the constrains $\sum i = 0$ is removed. Two different types of current control have been considered. The first case is illustrated in Fig. 5.8.

Figure 5.8: *Current vectors with $\beta = -\epsilon = 26.4$ degrees and $\iota = 0.08$, therefore $\gamma = -\delta = 0$ degrees and corresponding waveforms*

The vector of phase c and d are not modified, while the other two vectors are rotated by a suitable angle β and ϵ, where $\beta = -\epsilon$ to maintain the symmetry with respect to the fault. From the analytical model, the resulting average torque is about 75 % of the nominal torque, and the peak–to–peak torque ripple results in 18 %. By adding the third–order current harmonic, see the right hand side of Fig. 5.8, the average torque remains again about 75 % of the nominal torque, but the peak–to–peak torque ripple decreases to about 2 %. Fig. 5.9 illustrates the second case.
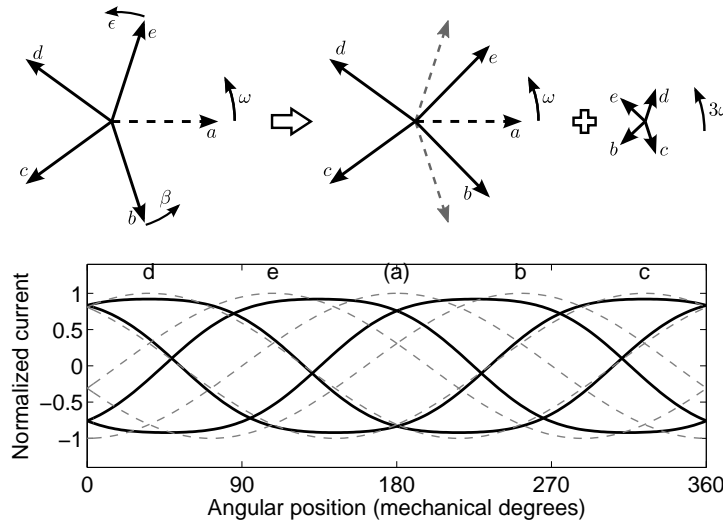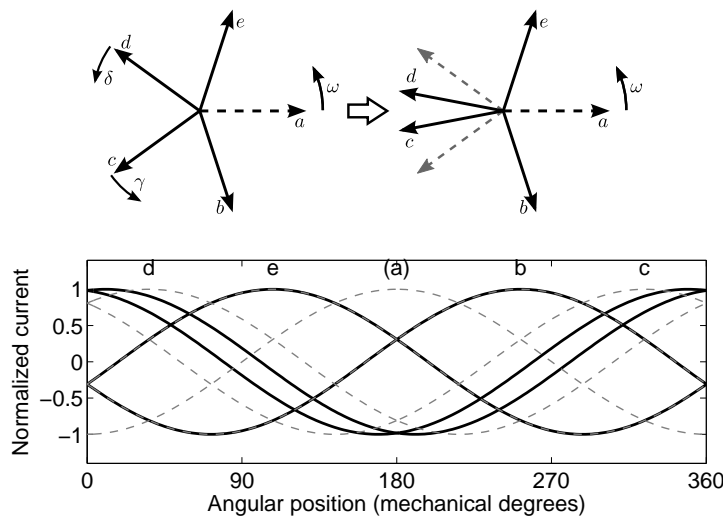

Figure 5.9: *Current vectors with $\beta = -\epsilon = 0$ degrees, therefore $\gamma = -\delta = 25.2$ degrees and corresponding waveforms*

The vector of phase b and e are not modified, while the other two vectors are rotated by a suitable angle γ and $\delta = -\gamma$. In this case, even without the injection of the third harmonic currents, the computed torque is quite satisfactory, with an average value of about 76 % and a peak–to–peak ripple of about 3 %.

Open circuit fault of two non–adjacent phases

The choice of the faulty phases is completely arbitrary, however, to the aim of simplifying the mathematical notation, phases b and e are opened . The expected average torque is about 40 % less of the nominal torque, proportionally to number of lost phases. As regards the torque ripple, it is computed to be about 90 %.

The first remedy control strategy is to adopt a system of sinusoidal currents (only the fundamental harmonic) where the current amplitudes of the phase c and d are ρ_1 times the current amplitude of the phase a (ρ_1 is the ratio between the amplitudes of fundamental current of different phases). In addition, in order to have the symmetry with respect to the faulty phases, the constraints $\alpha = 0$ and $\delta = -\gamma$ are fixed.

Using the half–bridge converter

Using the half–bridge converter, the constraint $\sum i = 0$ has to be considered as well. Referring to the predisposed prototype, the smoother torque has been computed with $\gamma = 0.536$ rad (i.e. 30.71 deg) and $\rho_1 = 1.264$. The latter factor means that the currents of the phases c and d result to be 26.4 % higher than the nominal current. The direct consequence is an increase of the Joule losses of about 66 % in the phases c and d. In any case, the total losses of the motor with two opened phases result lower than the rated losses in healthy mode. The computed average torque is about 64 % of the nominal torque, and the peak–to–peak torque ripple results in 17 %.

Similarly, the third time–harmonic of currents can be injected only in the three healthy phases. As before, $\alpha_{i3}^e = \alpha_i^e$ and $\gamma_3 = \gamma$ are assumed. Referring to the predisposed prototype, the best solution is achieved with $\gamma = 0.495$ rad (i.e. 28.33 degrees), $\iota = -0.108$, $\rho_1 = 1.154$, and $\rho_3 = -0.513$, as sketched in Fig. 5.10 (ρ_3 is the ratio between the amplitudes of the current harmonics of third–order of different phases). The computed average torque is about 61 % of the nominal torque, and the peak–to–peak torque ripple results in 3 %.

Using the full–bridge converter

Using the full–bridge converter, the constraint $\sum i = 0$ is removed.

Imposing current with only fundamental harmonic, the best results is achieved with a displacement of $\gamma = 0.619$ rad (i.e. 35.47 deg), and all currents with the same amplitude (i.e. $\rho_1 = 1$). From the analytical model, the resulting average torque is about 53 % of the nominal torque, and the peak–to–peak torque ripple remains limited to 15 %.

A smoother torque behaviour is achieved by injecting current harmonic of third order. The best result has been achieved by supplying only the phase c and d of the motor with the third–order current harmonic, as shown in Fig. 5.11. The computed average torque remains almost the same as above, but the peak–to–peak torque ripple decreases to less than 3.5 %.
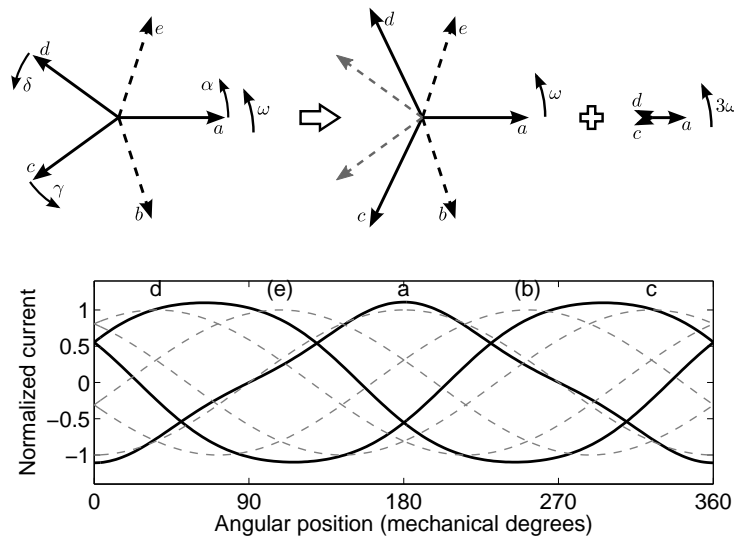
Figure 5.10: *Current vectors with two non–adjacent open phases: $\gamma = 28.33$ deg, $\rho_1 = 1.154$, $\rho_3 = -0.513$ and $\iota = -0.108$ and corresponding waveforms*
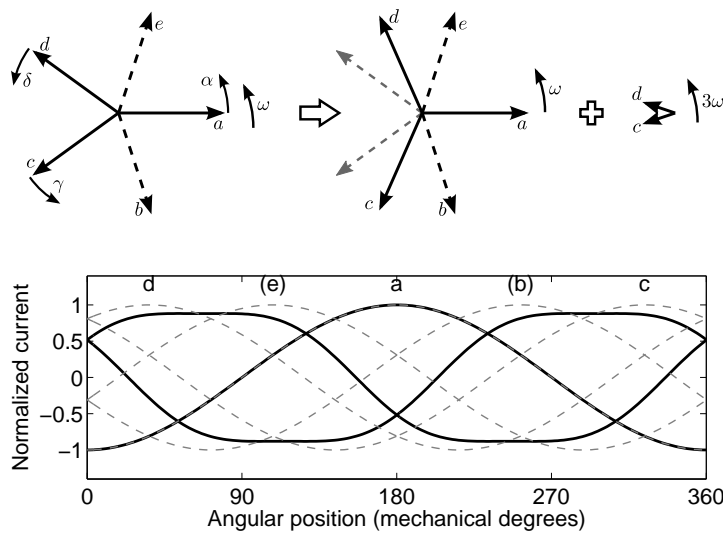
Figure 5.11: *Current vectors with two non–adjacent open phases: $\gamma = 30.2$ deg, $\rho_1 = 1$, and $\iota = 0.120$ and corresponding waveforms*

Open circuit of two adjacent phases

To the aim of simplifying the mathematical notation, the faulty phases are chosen to be the phases c and d. The healthy phases result to be the phases a, b and e. The symmetry with the faulty phases imposes $\alpha = 0$ and $\beta = -\epsilon$.

Using the half–bridge converter

Adopting the half–bridge converter, the constraint $\sum i = 0$ has to be also considered. In order to achieved a smooth torque, the computed value for the healthy phase currents are $\beta = -1.437$ rad (i.e. -82.33 degrees) and $\rho_1 = 0.555$, according to the predisposed prototype. However, the best solution that has been found is far from being acceptable. The computed torque exhibits an average value of 23 % of the nominal torque, and the torque ripple of about 55 %.

Even injecting a third time–harmonic of current, the torque behaviour is only slightly improved. As before, the best result is achieved when the third time–harmonic current is supplied only in phase b and e. These two current vector must have the same amplitude and be out of phase of 180 degrees (due to the constrain $\sum i = 0$ applied to the third order harmonic), as shown in the right part of Fig. 5.12. Referring to the predisposed prototype, $\beta = -1.742$ rad (i.e. -99.81 degrees), $\iota = 0.153$, and $\rho_1 = 0.505$ are computed. The computed torque exhibits an average value of 17 % of the nominal torque, and the torque ripple of about 8 %.

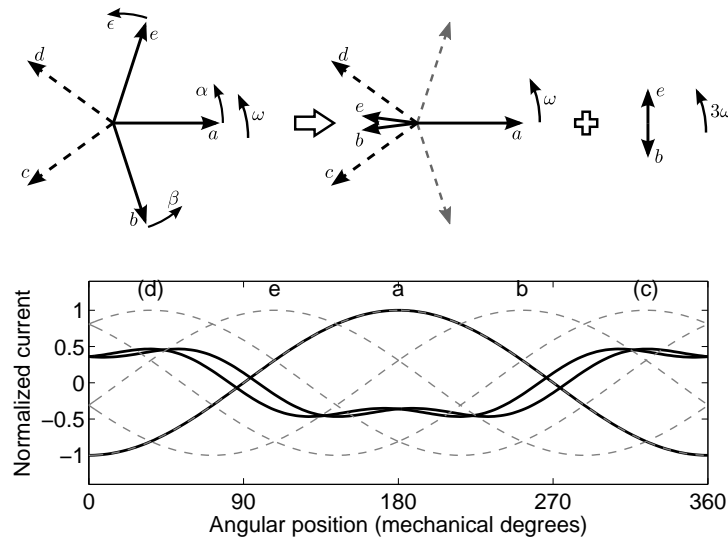**Figure 5.12:** *Current vectors with two adjacent open phases: $\beta = -99.81$ degrees, $\iota = 0.153$ and $\rho_1 = 0.505$ and corresponding waveforms*

It is worth noticing that the reduction of the torque ripple implies a high reduction of the average torque (from 60 to 17 %). The main cause of the reduction of the average torque is the constraint $\sum i = 0$ due to the adoption of the half–bridge converter.

Using the full–bridge converter

At the occurrence of this fault, the adoption of a full–bridge converter appears very advantageous: each phase could be supplied independently and a zero–sequence current is feasible.

Feeding the motor with fundamental currents only, with the same amplitudes ($\rho_1 = 1$) the best result is achieved with $\beta = 0.336$ rad (i.e. 19.24 deg). The computed torque is about 55 % of the nominal torque with a ripple of about 6 %.

By injecting the current harmonics of third order, the best result is achieved when only phase b and e are supplied, while third harmonic of phase a is equal to zero. The resulting coefficients are $\beta = 0.348$ rad (i.e. 19.96 degrees) and $\iota = -0.107$, as shown in Fig. 5.13. The computed torque remains about 55 % of the nominal torque with the ripple reduced to about 4 %.
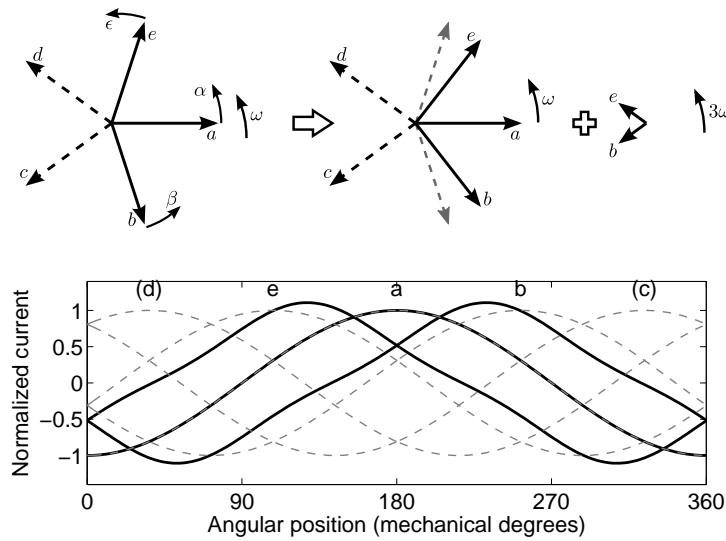
Figure 5.13: *Current vectors with two adjacent open phases: $\beta = 19.96$ degrees, $\iota = -0.107$ and corresponding waveforms*

5.4 Measurements of torque with different current control strategies

This section shows the measurements of the torque behaviours, according to the different current control strategies, computed above. In all tests, a good agreements between predicted and measured behaviours have been found, verifying the hypothesis and the procedures adopted in the analytical approach.

One–phase open circuit fault

Fig. 5.14a refers to the operating conditions with one opened phase without any adjustment of the other healthy phases.
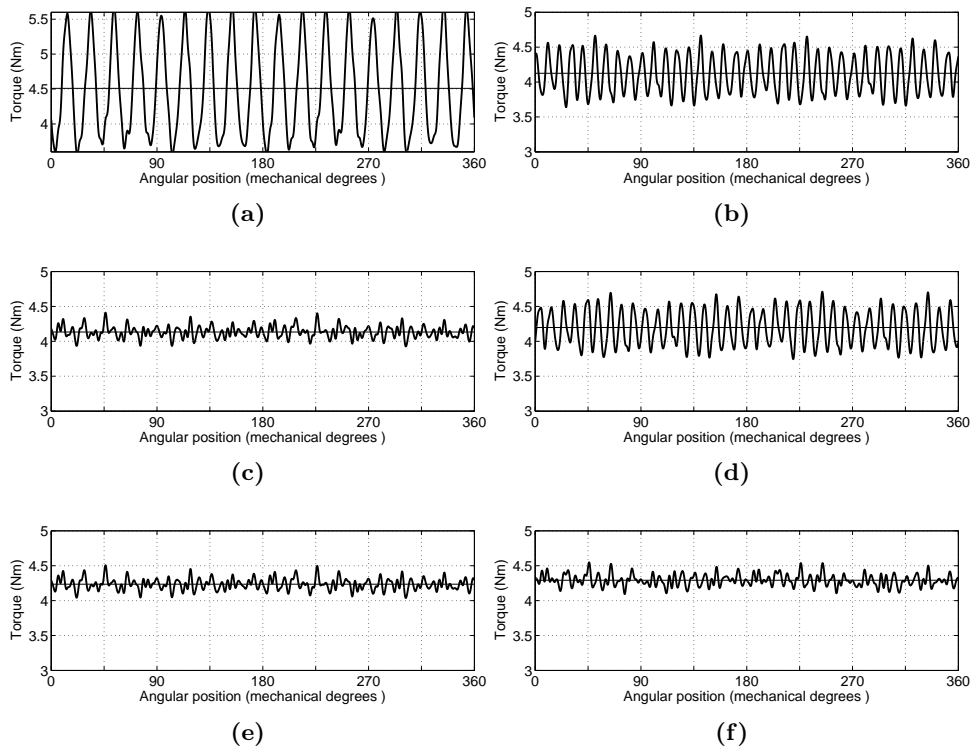
Figure 5.14: *Open circuit of one phase. Measured torque behaviours:*
(a) $\beta = 0$ deg and $\iota = 0$,
(b) $\beta = 33.06$ deg and $\iota = 0$,
(c) $\beta = 31.28$ deg and $\iota = 0.0876$,
(d) $\beta = 29.56$ deg and $\iota = 0$ and full–bridge converter ($\sum i \neq 0$),
(e) $\beta = 25.72$ deg and $\iota = 0.0867$ and full–bridge converter ($\sum i \neq 0$),
(f) $\gamma = -24.00$ deg and $\iota = 0$ and full–bridge converter ($\sum i \neq 0$),

The resulting torque behaviour is as expected. The average torque results slightly lower than 80 % of the nominal torque (i.e. about 4.5 Nm instead of 5.5 Nm), and the torque ripple results slightly higher than 50 % (i.e. about 2 Nm over 4.5 Nm).

Using the half–bridge converter

Fig. 5.14b shows the behaviour of the torque with the control strategy proposed adopting the half–bridge converter, with the phase displacement between the vectors only. There is not change in the current amplitude, and no injection of third–order harmonics. As expected, the average torque results in 74 % of nominal torque, and the torque ripple is about 20 % with respect to the average value.

Fig. 5.14c refers to the current control strategy with the injection of the third–order current harmonics. Once again the results are as predicted. The average torque remains unchanged, while the torque ripple is reduced to the same value observed under healthy operations.

Using the full–bridge converter

Figs. 5.14d, 5.14e and 5.14f refer to the torque behaviours achieved by using the full–bridge converter, so that the sum of the currents is not more equal to zero.

Fig. 5.14d has been obtained by an angular displacement of current vectors of the phases e and f, as described in the first current control strategy (page 80). As predicted, the average torque results in 75 % of nominal torque, and the torque ripple slightly lower than 20 % of the average value.

Fig. 5.14e shows torque behaviour, introducing the displacement in the same current vectors and injecting a third–order harmonic component, as described at page 80, Fig. 5.8. As predicted, the same average torque is achieved, and the torque ripple reduces to that measured under healthy operation.

Fig. 5.14f shows the measured torque behaviour, corresponding to the second current control strategy described at page 80, see Fig. 5.9. An angular displacement is in the current vectors of phase c and d only, without any third–order current harmonic. The resulting torque exhibits an average torque higher than 76 % of nominal torque, and the torque ripple equal to that measured under healthy operation, as predicted. It is worth to notice that using the full–bridge converter, a smooth torque is achieved with a satisfactory average torque, even without injecting the third–order harmonic. Since the remedy control strategy requires only a current vector displacement, it results to be very easy to be implemented.

Two non–adjacent phases open circuit fault

Fig. 5.15a refers to the measured torque behaviour corresponding to two opened non–adjacent phases.

Figure 5.15: *Open circuit of two non–adjacent phases. Measured torque behaviours:*
(a) faulty operations, without control,
(b) $\rho_1 = 1.264$ and $\gamma = 30.71$ deg,
(c) $\rho_1 = 1.13$, $\gamma = 27.73$ deg, $\iota = -0.112$ and $\rho_3 = 0.51$,
(d) $\gamma = 35.47$ deg, $\iota = 0$ and full–bridge converter ($\sum i \neq 0$),
(e) $\gamma = 29.28$ deg and $\iota = 0.122$ and full–bridge converter ($\sum i \neq 0$).

As predicted before (page 81, the average torque is about 60 % of nominal torque in healthy conditions (i.e. 3.3 Nm versus 5.5 Nm) and the torque ripple is about 91 % (i.e. 3 Nm over 3.3 Nm).

Using the half–bridge converter

Fig. 5.15b shows the measured torque behaviour, when the current vectors of the phases c and d are increased of 26.4 % in amplitude (i.e. $\rho_1 = 1.264$) and rotated by the angle $\gamma = 30.71$ deg, see page 81. The measured torque is in accord with the computed one: the average torque is about 64 % of the nominal torque, and the peak–to–peak torque ripple results to be slightly higher that the predicted 17 %.

Fig. 5.15c shows the measured torque behaviour, when the current harmonics of third order are included, according with the parameters found before (page 81). The measured average torque results slightly lower than predicted, decreasing from 3.45 Nm to 3.25 Nm. However, the torque ripple results to be comparable with that measured in healthy operations (see Fig. 5.5).

Using the full–bridge converter

Using full–bridge converter, Fig. 5.15d shows the torque behaviour with current vector of equal amplitude and a displacement $\gamma = -\delta = 35.47$ deg and only fundamental harmonic. As expected, the measured average torque is about 55 % of the nominal torque (i.e. 3.05 Nm over 5.5 Nm), and the peak–to–peak torque ripple about 24 % (i.e. 0.75 Nm over 5.5 Nm), slightly higher than the computed one.

A further comment can be carried out about the comparison of the Joule losses when the motor operates in healthy and faulty mode. When two of the five phases are opened, the remaining three phases can be increased by a factor 1.29, so as to have the same Joule losses. The direct consequence is an increase of the torque of the same factor, reaching the 70 % of the nominal torque.

Fig. 5.15e shows the measured torque behaviour when additional third–order current harmonics are injected, as discussed before (page 81). The average torque slightly increases, and the torque ripple decreases, although remaining higher than that measured under healthy mode operations.

Two adjacent phases open circuit fault

In the case of fault of two adjacent phases the advantages of using the full–bridge converter are better highlighted.

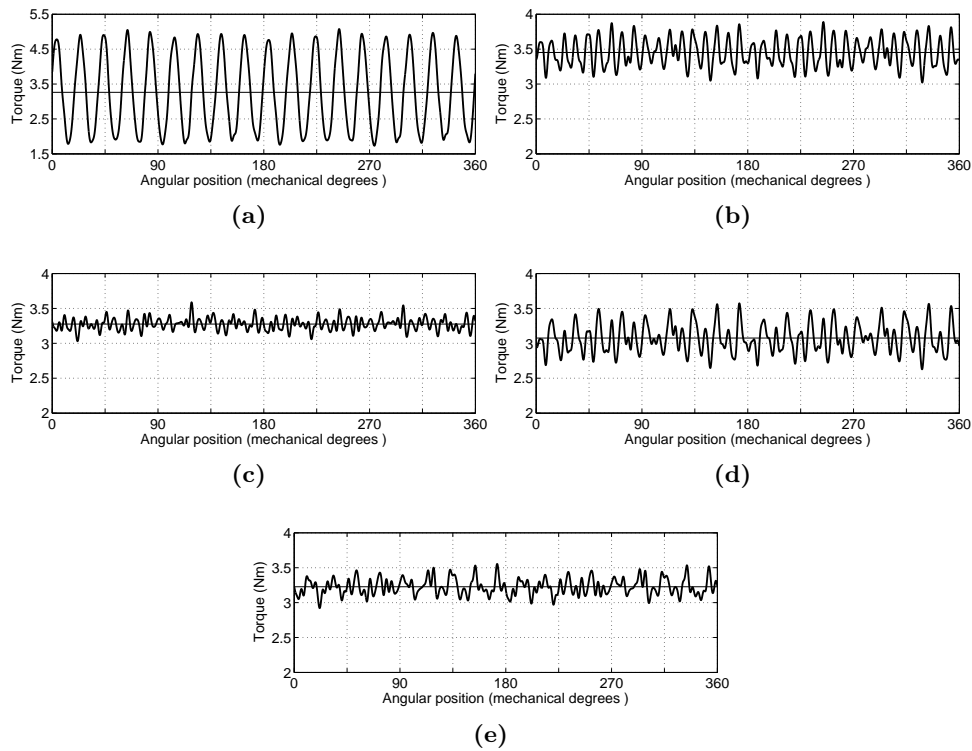Fig. 5.16a shows the measured torque behaviour, with two opened adjacent phases and no remedy control.
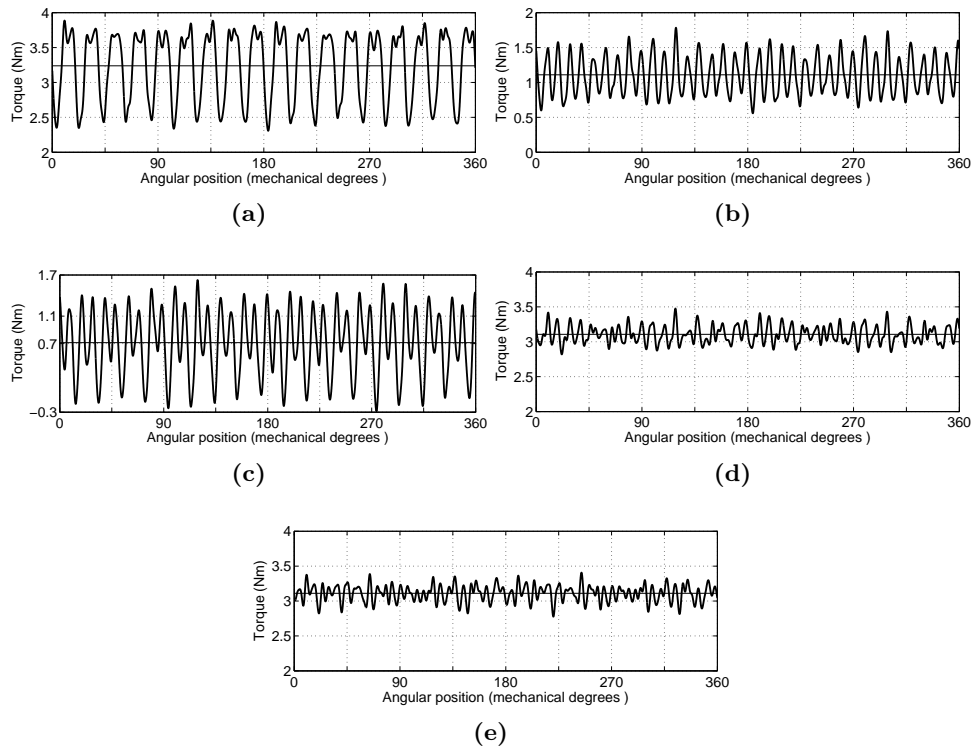
Figure 5.16: *Open circuit of two adjacent phases. Measured torque behaviours:*
(a) faulty operations, without control,
(b) $\rho_1 = 0.555$ and $\beta = -82.33$ deg,
(c) $\rho_1 = 0.505$, $\beta = -99.81$ deg and $\iota = 0.153$,
(d) $\beta = 19.25$ deg and $\iota = 0$ and full–bridge converter $(\sum i \neq 0)$,
(e) $\beta = 19.94$ deg and $\iota = 0.107$ and full–bridge converter $(\sum i \neq 0)$.

According to the loss of two phases, the average torque decreases to 60 % of the nominal value: the measured average torque is about 3.25 Nm. The torque ripple is about 46 % (i.e. 1.5 Nm over 3.25 Nm), slightly higher than predicted (about 38 %).

Using the half–bridge converter

Fig. 5.16b shows the measured torque behaviour after an adjustment of the vector angles. As predicted, a direct consequence of imposing a low torque ripple is a high decreasing of the average torque. The measured average torque falls down to 1.1 Nm, which is the 20 % of the nominal torque (predicted value is about 23 %). The torque ripple reaches about 100 % of the average value, higher than predicted. Thus motor operations are strongly penalized. The very high decrease of the average torque is mainly due to the constraint $\sum i = 0$, imposed by the use of the half–bridge converter.

As commented before (page 83), even injecting current harmonics of third order (only in phase b and e), the torque behaviour is only slightly improved, as shown in Fig. 5.16c. The average torque is further reduced, being 13 % of the nominal torque. Then, contrarily to the predictions, the torque ripple increases.

From these tests, it is clear that the motor performance are not acceptable. The limitation of the average torque and the high ripple do not allow the motor to operate adequately. Therefore, the use of the half–bridge converter is really disadvantageous when a fault occurs in two adjacent phases.

Using the full–bridge converter

A great improvement is achieved using a full–bridge converter. Fig. 5.16d shows the measured torque behaviour feeding the motor with fundamental currents only, rearranging the current vectors as described before (page 84). The measured average torque is about 56 % of the nominal torque, as predicted, while the torque ripple is slightly higher, 15 % instead of 6 %.

It is worth noticing that the average torque remains close to the theoretical value of 60 % corresponding to two opened phases. Once again, the use of the full–bridge converter gives a substantial improvement of the motor performance. In addition, considering the same Joule losses, the average torque can be increased of a factor 1.29, increasing to 72 % of the nominal torque in healthy operating conditions.

By injecting the current harmonics of third order, there is not a substantial improvement in the torque behaviour as shown in Fig. 5.16e. The measured average torque and the ripple remain almost the same.

5.5 Conclusions

This chapter analyses the open circuit faults of one and two phases of a five–phase PM motor, together with some current control strategies to be adopted in the presence of such faults. The current control strategies are proposed to achieve a smooth torque and adequately high average torque.

It is shown that the use of the full-bridge converter have the following advantages: (i) a smooth torque is achieved even with no injection of current harmonics of third order, and (ii) all the currents under post–fault operation show the same amplitude. These two issues allow an easier control to be adopted, even after the occurrence of fault: only a rotation of the fundamental harmonic of the currents is enough to achieve smooth and high torque.

In addition, at the occurrence of two opened adjacent phases, that is the worst case considered here, there is not the limitation of having $\sum i = 0$ (required by the half–bridge converter). The direct consequence is that the average torque during post–fault operation remains to a high value.

Finally, in order to maintain the same Joule losses in healthy and in faulty operating conditions, the torque can be increased by a factor of 1.12 in case of four healthy phases, and of 1.29 in case of three healthy phases.

CHAPTER 6

Experimental comparison between two fault–tolerant fractional–slot multiphase PM motor drives

Abstract

In this chapter an experimental comparison between two fault–tolerant fractional–slot permanent magnet motor drives is presented.

Five–phase and dual–three phase motor drives are considered.

Both of them exhibit fault–tolerant capability, but also completely different peculiarities. The five–phase machine requires a custom machine design and inverter, but it is able to operate with the loss of one or two phases with higher performance than the dual–three phase machine. On the other hand, the second configuration is obtained with standard components and, in the event of fault, one half of the machine is disconnected so as to operate with the healthy part only.

The aim is to highlight the main differences between the two motor drives in terms of their performance under fault conditions.

Open circuit and short circuit faulty operating conditions are taken into account by means of measurements on prototypes.

Advantages and drawbacks of the two systems are discussed and remarked.

6.1 Multiphase machines

To the purpose of achieving a motor drive with high fault–tolerance, the first step is to choose that motor exhibiting an intrinsic fault–tolerant capability. Fractional–slot winding motors with non–overlapped coils prove to be well suited for fault–tolerant applications [37]. They allow a physical separation among the phases, limiting the propagation of the fault. They are also characterized by a high self inductance, necessary to limit the short–circuit current.

In addition, a suitable combination of slots and poles yield a very low mutual coupling between phases, avoiding faulty and healthy phases mutual interaction [27]. The single–layer winding has been proposed so as to eliminate the physical contact between phases [3, 36].

Five phase motor

The five–phase motor is characterized by a number of slots multiple of 5. This requires both custom laminations for the machine stator and custom inverter to supply the five–phase motor. The scheme of a five phase motor drive is shown in Fig. 6.1. Two kinds of converter can be used, as reported in chapter 5: a half–bridge and a full–bridge converter. The second solution has two main advantages: (i) the phase currents are independent, i.e. they are not constrained to satisfy the condition $\sum i = 0$, as in the half–bridge converter; (ii) there is not electrical interaction among phases, so that one can be disconnected independently from the others [38]. As reported in chapter 5, the Volt–Amps rating (given by the product of rated current by dc voltage and by the switch numbers) of the full–bridge converter is about 105 % the Volt–Amps rating of the half–bridge one.
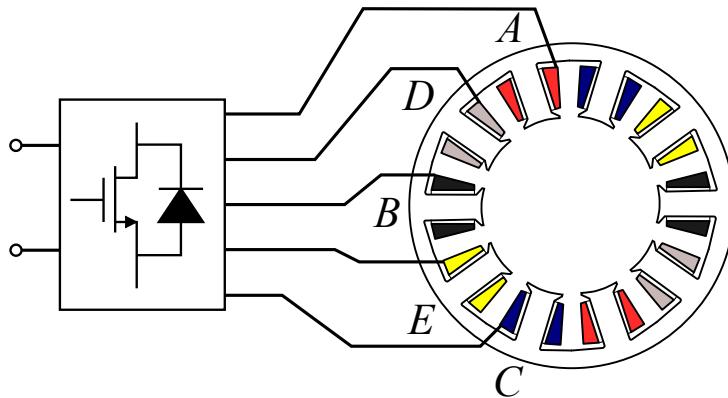
Figure 6.1: *Scheme of the five–phase motor drive.*

A five–phase motor can operate also in case of one or two opened phases; Fig. 6.2 shows examples of the loss of one and two phases, the second being adjacent or not.

In the event of a fault, the current control strategy is modified so as to enable a smooth running also under faulty operations (see chapter 5). The current control strategy is modified with respect to normal conditions and current harmonics of third–order can be injected to the aim of increasing the average torque and reducing the torque ripple.

The experimental results described in this chapter refer to a 5–phase 20–slot 18–pole surface mounted permanent magnet (SPM) motor prototype (see chapter 5).
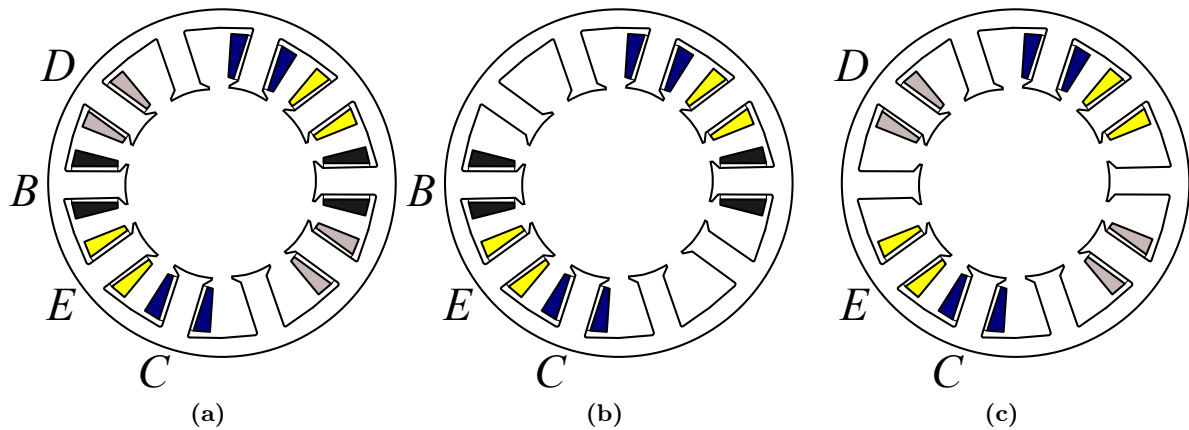
Figure 6.2: *Five–phase motor: examples of the loss of one or two phases.* (a): *single phase open circuit;* (b): *double adjacent phases open circuit;* (c): *double non adjacent phases open circuit.*

Dual–three phase motor

In a dual three–phase winding motor drive, there are two identical windings, each supplied by a separate inverter. In the event of a fault in a part of one winding, the corresponding inverter is switched off and only the healthy winding continues to be supplied [14, 41].

The power cutback corresponds to half the nominal motor power, and the motor drive continues to operate under such an operating condition. This aspect could be extremely relevant in high power applications, due to the converter cost. Such a system can be considered a modular solution [42]. The scheme of the dual three–phase motor drive is shown in Fig. 6.3.

Figure 6.3: *Scheme of the dual three–phase motor drive.*

The phases of the two windings are labeled as A, B, and C for the first winding, and A', B', and C' for the second one. As will be shown in the following, some distinctions can be carried out according to the arrangements of the coils of the two windings.

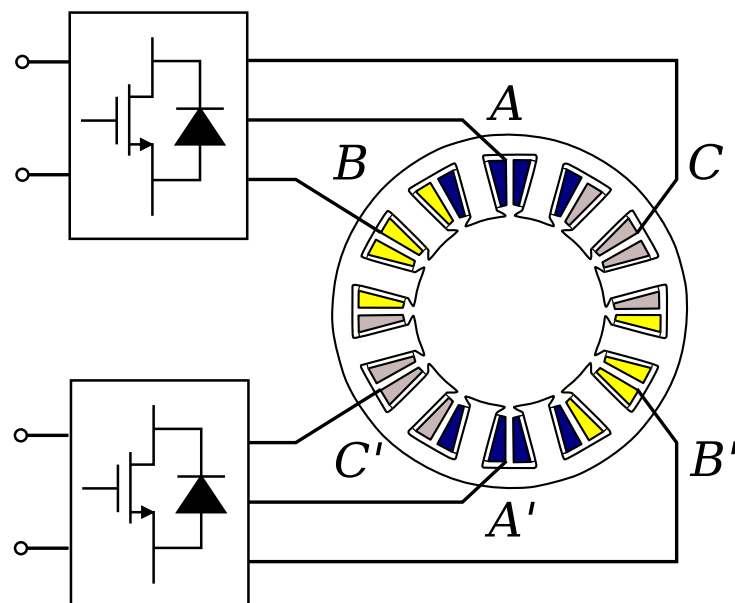A 12–slot 10–pole interior permanent magnet (IPM) motor with non–overlapped coils winding has been built and tested [43], Fig. 6.4.
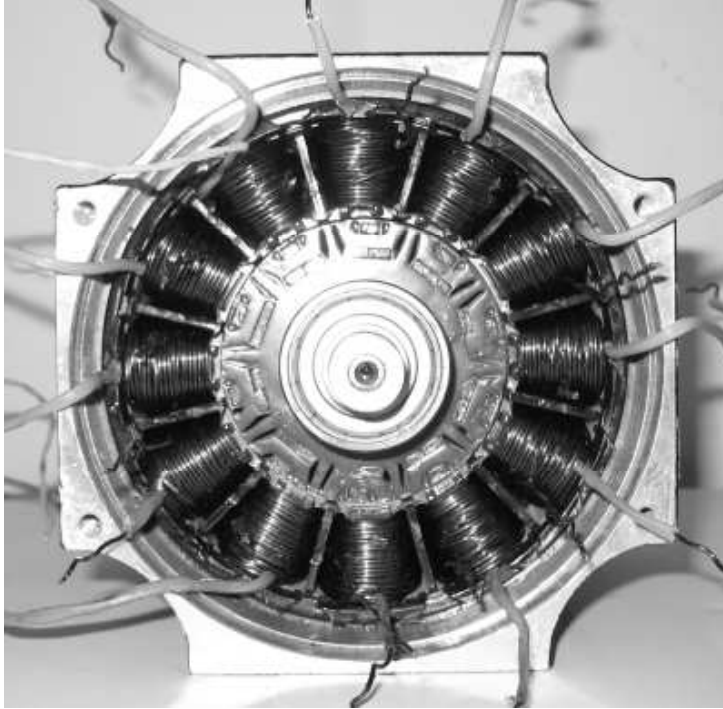
Figure 6.4: *The 12–slot 10–pole dual three–phase motor prototype.*

It exhibits a high self inductance and a low mutual inductance. The terminals of each coil are available, so as to allow different winding connections.

Double–layer (DL) windings are reported in Fig. 6.5, in which only one of the two three–phase windings is shown. The single–layer winding configurations are reported in [43]. In the configuration DL–1, each of the two three–phase windings is placed in a well–defined part of the stator, Fig. 6.5a. On the contrary, the coils of the two windings are alternated along all the stator circumference in configurations DL–2, Fig. 6.5b, and DL–3, Fig. 6.5c.

Depending on the winding arrangements, it can be possible to take advantage of the presence of the two separate three–phase windings. Under specific electrical and mechanical conditions [43], a complete six–phase motor can be obtained from the dual–three phase machine configuration. In the 12–slot 10–pole motor, a six–phase supply can be used only when the double–layer DL–3 configuration is adopted, see Fig. 6.5c.
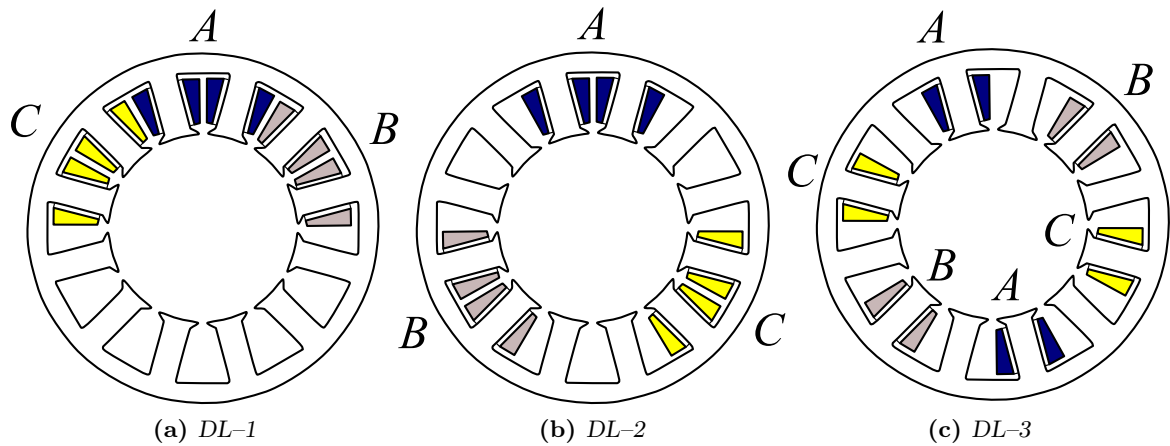
Figure 6.5: *Dual three–phase motor: three examples of the remaining phase coils, after removing one of the two three–phase double–layer windings.*

6.2 Healthy mode operations

Five phase motor

Average torque results in 5.5 Nm, in a good agreement with the torque computed analytically [44]. Torque ripple (mainly due to the cogging torque) is quite low, it results to be slightly higher than predicted [44], probably due to the manufacturing process.

Dual three–phase

Referring to Table 6.1, for motor with the six–phase supply the average torque results to be slightly higher (and the torque ripple lower) than with the corresponding three–phase supply. This is due to the higher winding factor (with six–phase winding there is a unity distribution factor), and the lower MMF harmonic contents.

Table 6.1: *Dual three–phase motor: performance with various winding arrangements IPM motor ($\hat{I} = 6.2$ A peak).*

Motor config.	Measured average torque (Nm)	Measured torque ripple (%)	Simulated unbalanced radial force (N)
six–phase	7.07	11.1 %	1.78
DL healthy	6.83	16.4 %	1.3
DL–1	3.36	20.7 %	1009
DL–2	3.14	22.5 %	723
DL–3	2.79	12.6 %	0.6

With three–phase supply, the average torque and the torque ripple remain almost the same as shown in Table 6.1.

6.3 Open circuit faulty mode operations

Five phase motor

Measurements of the torque behaviours, according to different current control strategies are reported in [44]. Hereafter the results that yield the lowest torque ripple are summarized. In all tests, a good agreements between predicted [45] and measured behaviours have been found.

One–phase open circuit fault

Measured machine performance with one open circuited phase is reported in the second row of Table 6.2.

Table 6.2: *Five–phase motor: measured performance with various open circuit faulty mode operations.*

Motor config.	half–bridge		full–bridge	
	Average torque	Torque ripple	Average torque	Torque ripple
healthy	100 % (5.5Nm)	5 %	100 % (5.5Nm)	5 %
1 phase open circuit	74 % (4.07Nm)	8 %	78 % (4.29Nm)	7 %
2 adj. phases open circuit	59 % (3.25Nm)	13 %	57 % (3.14Nm)	16 %
2 non adj. phases open circuit	20 % (1.1Nm)	100 %	56 % (3.08Nm)	15 %

The table refers to the torque behaviours achieved by using both a half–bridge and a full–bridge converter and by adopting the proper current control strategy described in [45].

It is worth to notice that using both the converters, a smooth torque is achieved with a satisfactory average torque (about 78 % of the torque in healthy conditions).

Two non–adjacent phases open circuit fault

Third row of table 6.2 refers to the measured torque behaviour corresponding to two open circuited non–adjacent phases using half–bridge and full–bridge converter. The resulting torque is quite smooth with average value slightly lower than 60 %.

Two adjacent phases open circuit fault

In the case of fault of two adjacent phases the advantages of using the full–bridge converter are highlighted.

Fourth row of table 6.2 reports the measured torque behaviours with two open circuited adjacent phases after the application of the proper current control strategy. In this case, the use of the full–bridge converter gives a substantial improvement of the motor performance: properly high average torque and reduced torque ripple.

Dual three–phase motor

As said above, the faulty three–phase winding is completely disconnected and the motor operates with only one of the two three–phase windings supplied. As regards the average torque, regardless of the winding configuration, all motors exhibit almost half a torque than healthy operation [43].

The torque ripple varies according to on the adopted configuration, see Table 6.1. Among the others the DL–3 configuration exhibits always a value of torque ripple almost equal to the healthy configuration, but a slightly lower average torque.

As regards the unbalanced radial force on the rotor, the worst case is achieved with the configuration DL–1, since the winding covers only a part of the stator. However, a non negligible radial force is observed also in configuration DL–2.

6.4 Short–circuit faulty mode operations

Both five–phase and dual–three phase motor are designed in order to reduce the short–circuit current I_{shc}, as explained in [34]. The SPM machine (as the five–phase motor prototype) shows a higher short–circuit current as respect to the IPM machine (as the dual–three phase motor prototype) due to the lower inductance.

For the purpose of quantifying the impact of the short–circuit fault in the IPM prototype, the rotor was dragged by a master drive with all the stator coils short–circuited. The steady state short–circuit currents and braking torque were measured at different speed.

Table 6.3: *Dual three–phase motor: measured average torque, torque ripple and short–circuit (ShC) current, while one winding continues to be properly supplied ($\hat{I} = 6.2$ A peak).*

Wind. config.	1–PH SHC			3–PH SHC		
	T (Nm)	ΔT (%)	$\hat{I}_{shc}$ (A)	T (Nm)	ΔT (%)	$\hat{I}_{shc}$ (A)
DL–1	3.05	38.6	2.23	2.73	38.9	2.26
DL–2	2.87	36.8	2.68	2.44	29.2	2.56
DL–3	2.61	41.3	3.52	1.86	16.0	3.54

Five phase motor

According to a complete short–circuit of one phase coil, short circuit current is increasing with the speed, but it is limited in the motor working range [46].

Dual three–phase motor

Tests were carried out feeding one winding by the converter, and the other winding short–circuited. Two cases have been tested: (i) with only one phase short–circuited, (ii) with all three phases short–circuited. The experimental results are reported in Table 6.3.

In all tests, the amplitude of the short–circuit current remains limited and close to that estimated in the short–circuit above. The lower values are found in DL–1 configuration while the higher values are found in DL–3 configuration, where the healthy and faulty coils are alternated and thus the mutual coupling between the two windings is relevant [43].

The average torque decreases when one winding is short–circuited, about 7–8 % with one phase short–circuited and about 20–30 % with the three phases short–circuited. It could be noted that the pulsating torque, occurring with one faulty phase, involves a higher increase of the torque ripple.

DL–2 and DL–3 configurations with one short–circuited winding exhibit a torque ripple close to same achieved with one open–circuited winding (see Table 6.1).

6.5 Discussion

Hereafter the advantages and drawbacks of the two motor drives considered are summarized. Concerning the five-phase motor drive advantages and drawbacks are summarized as follow:

- Custom laminations have to be designed and stamped for the five–phase motor stator.

- A non standard five–phase converter is needed to control the motor.

- The main advantages of using a five–phase motor drive are found in its reliability to operate properly also in faulty conditions. It can operate with one or two open circuited phases (adjacent or not) giving the drive a high tolerance to faults. In both cases the disconnected

phases are the faulty ones only, while other phases remain operating as in the normal working conditions.

- In all faulty cases, a proper current control strategy can be found so as to limit the torque ripple, and this could be a mandatory requirement in several applications.

- When the drive operate in faulty conditions, the average torque results to be proportional to the number of the healthy operating phases, for phase currents amplitude fixed to nominal value.

- It has also been seen that, when two adjacent phases are open circuited, the best result is achieved adopting a full–bridge inverter since it allows a properly high average torque and a low torque ripple to be obtained.

As far as the dual three–phase winding motor drive is concerned, the following considerations are made:

- The major advantage is the possibility to use standard components available on the market, as three–phase inverters and three–phase laminations,

- In the event of fault of one winding or one converter, the motor is operated by means of the remaining healthy winding only, of course, at reduced power. Independently of the winding arrangement, the average torque for given current is approximately halved. However the torque ripple generally increases.

- A high unbalanced radial force on the rotor arises when supplying a single winding, even if the coils of this winding are distributed along the stator circumference. In order to limit this radial force, it is necessary that coils of the same phase are placed on symmetrical parts of the stator, as for the configuration DL-3 or motor with periodicity higher than unity.

- Finally, all winding arrangements yield a low mutual coupling between the two windings, but the configuration DL-3. This is not surprising, since such a configuration is characterized by alternate coils of the two windings.

6.6 Conclusions

Two fault–tolerant motor drives (a five–phase and a dual–three phase motor drive) have been compared both in healthy and in faulty mode operations. Fault–tolerance as well as modularity can be obtained by both systems. Short circuit fault as well as open circuit faults have been considered. As regard the behaviour under fault, better results in terms of average torque and torque smoothing can be achieved with a five–phase motor drive. However, this drive requires a non standard motor as well as a non standard converter. It is well suited for particular applications as for aerospace and aeronautic ones. Dual–three phase systems seem to be suitable for industry, since standard motors and converters can be used. Choosing properly the winding, the five–phase motor can be designed using standard lamination; in this way the limitation due to the non standard lamination is overcame.

CHAPTER 7

Five–phase space vector
harmonic analysis

Abstract

This chapter deals with the harmonic analysis of the orthogonal space vector components of a five–phase machine. It gives a complete analysis of the harmonic contents of the resulting space vector, considering both symmetric and asymmetric systems.

Then, the impact of some phase asymmetries on the space vector harmonic contents is investigated. Therefore the results achieved in such a study will be of reference for determining a fault diagnosis procedure.

Diagnosis techniques have to detect the fault at an early state avoiding the fault to be propagated to the healthy machine parts [18, 19]. These non–invasive techniques sense the unexpected electrical signal, which commonly is combined with a phase asymmetry, caused by fault [20, 21, 24, 47].

This chapter investigates the effect of such an asymmetry on the electrical quantities of the machine. Space vectors are defined for the five–phase machine including harmonic contents in the electrical quantities. The impact of the asymmetry of one phase on the space vector harmonic contents is investigated.

At first, a symmetric system is described, with voltages of purely sinusoidal waveform. Then, a symmetric system is studied including voltages with more complex waveforms, that is, with many harmonics superimposed to the fundamental one. Finally, the asymmetry is introduced in one phase voltage, according to both the sinusoidal voltages and the non-sinusoidal ones.

7.1 Definition of the space vector

This section reports a definition of the space vector of a five–phase machine. Let us refer to a generic electrical quantity, for example the phase terminal voltage. The transformation from the phase voltage v_0, v_1, v_2, v_3, and v_4 to the orthogonal components into the stationary reference frame, that is, v_α, v_β, v_{α_2}, v_{β_2}, and v_z, is achieved by means of a matrix vector given by (7.1), where $\dot{a}$ is the operator $\dot{a} = e^{\jmath 2\pi/5}$. The first vector corresponds to the space vector $\vec{\mathbf{v}}_{\alpha\beta} = v_\alpha + \jmath v_\beta$, the second vector corresponds to the space vector $\vec{\mathbf{v}}_{\alpha_2\beta_2} = v_{\alpha_2} + \jmath v_{\beta_2}$, and the third quantity is the zero sequence component v_z. The coefficient $2/5$ is used to have the same amplitude of the voltage space vector and of the phase voltages.

$$
\begin{bmatrix} \vec{\mathbf{v}}_{\alpha\beta} \\ \vec{\mathbf{v}}_{\alpha_2\beta_2} \\ v_z \end{bmatrix} = \frac{2}{5} \begin{bmatrix} \dot{a}^0 & \dot{a}^1 & \dot{a}^2 & \dot{a}^3 & \dot{a}^4 \\ \dot{a}^0 & \dot{a}^2 & \dot{a}^4 & \dot{a}^6 & \dot{a}^8 \\ \frac{1}{2} & \frac{1}{2} & \frac{1}{2} & \frac{1}{2} & \frac{1}{2} \end{bmatrix} \begin{bmatrix} v_0 \\ v_1 \\ v_2 \\ v_3 \\ v_4 \end{bmatrix}
\tag{7.1}
$$

Hereafter, space vector $\vec{\mathbf{v}}_{\alpha_2\beta_2}$ is obtained by using the powers multiple of two of the operator $\dot{a}$ (i.e. $\dot{a}^0$, $\dot{a}^2$, $\dot{a}^4$, $\dot{a}^6$, and $\dot{a}^8$), as in [48]. An alternative definition of the second space vector is given in [16], where the power multiple of three of the operator $\dot{a}$ are used (i.e. $\dot{a}^0$, $\dot{a}^3$, $\dot{a}^6$, $\dot{a}^9$, and $\dot{a}^{12}$), achieving the space vector $\vec{\mathbf{v}}_{\alpha_3\beta_3}$. In any case, the two space vectors contain the same information, so that they are identical from the frequency analysis point of view.

Fig. 7.1 shows the operators of the space vector $\vec{\mathbf{v}}_{\alpha_2\beta_2}$ and of the space vector $\vec{\mathbf{v}}_{\alpha_3\beta_3}$. It is worth noticing that the sequence of the operators is the same, but it is clockwise for $\vec{\mathbf{v}}_{\alpha_2\beta_2}$ and counterclockwise for $\vec{\mathbf{v}}_{\alpha_3\beta_3}$.
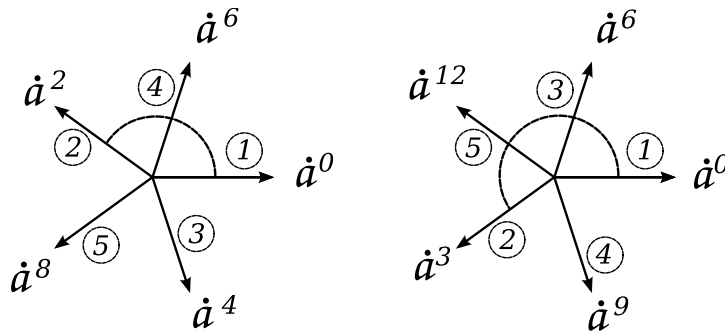

Figure 7.1: *Complex operators of the space vectors $\vec{\mathbf{v}}_{\alpha_2\beta_2}$ and $\vec{\mathbf{v}}_{\alpha_3\beta_3}$.*

7.2 Symmetric systems

Case 1: symmetric system with only fundamental harmonic

At first, a symmetric system is considered, formed by five voltages of sinusoidal waveform:

$$v_m(t) = \hat{V}_1 \cos\left(\delta_1 - m\frac{2\pi}{5}\right) \tag{7.2}$$

where $m = 0, 1, 2, 3, 4$ indicates the voltage phase. In the following, space vectors in $\alpha\beta$ and $\alpha_2\beta_2$ reference frames are derived, as well as zero sequence component. In order to compact the equations, $\delta_1 = \omega t$ is introduced.

$\alpha\beta$ reference frame

From the definition (7.1), the space vector in $\alpha\beta$ reference frame can be achieved as:

$$\vec{\mathbf{v}}_{\alpha\beta} = \frac{2}{5}\left[v_0(t) + v_1(t)\,e^{j2\pi/5} + v_2(t)\,e^{j4\pi/5} + v_3(t)\,e^{j6\pi/5} + v_4(t)\,e^{j8\pi/5}\right] \tag{7.3}$$

Substituting (7.2) in (7.3), it results in:

$$\vec{\mathbf{v}}_{\alpha\beta} = \frac{\hat{V}_1}{5}\left[\sum_{m=0}^{4} e^{j(\delta_1)} + \sum_{m=0}^{4} e^{-j\left(\delta_1 - 2m\frac{2\pi}{5}\right)}\right] \tag{7.4}$$

The first term within square brackets is the sum of five parallel phasors, while the second sum is always zero. Therefore, the space vector simply reduces in:

$$\vec{\mathbf{v}}_{\alpha\beta} = \hat{V}_1 e^{j(\delta_1)} \tag{7.5}$$

If such a space vector is represented in the synchronous reference frame, that is, the $d-q$ reference frame, it results to be a stationary vector.

$\alpha_2\beta_2$ reference frame

From the definition in (7.1), the space vector in $\alpha_2\beta_2$ reference frame results in:

$$\vec{\mathbf{v}}_{\alpha_2\beta_2} = \frac{2}{5}\left[v_0(t) + v_1(t)\,e^{\jmath 4\pi/5} + v_2(t)\,e^{\jmath 8\pi/5} + v_3(t)\,e^{\jmath 12\pi/5} + v_4(t)\,e^{\jmath 16\pi/5}\right] \qquad (7.6)$$

Substituting (7.2) in (7.6), it results in:

$$\vec{\mathbf{v}}_{\alpha_2\beta_2} = \frac{\hat{V}_1}{5}\left[\sum_{m=0}^{4} e^{\jmath\left(\delta_1 + m\frac{2\pi}{5}\right)} + \sum_{m=0}^{4} e^{-\jmath\left(\delta_1 - 3m\frac{2\pi}{5}\right)}\right] \qquad (7.7)$$

In this case both sums are zero, so the space vector in $\alpha_2\beta_2$ reference frame is always equal to zero: $\vec{\mathbf{v}}_{\alpha_2\beta_2} = 0$.

Zero sequence component

From (7.1), the zero sequence component results in:

$$v_z = \frac{1}{5}\left[v_0(t) + v_1(t) + v_2(t) + v_3(t) + v_4(t)\right] \qquad (7.8)$$

and, from (7.2), it is $v_z = 0$.

In conclusion, the space vector that represents a five–phase symmetric system of sinusoidal voltages has only two components different from zero, expressed as $\vec{\mathbf{v}}_{\alpha\beta}$. In $\alpha\beta$ reference frame it results to be a rotating space vector with constant amplitude and angular speed equal to ω.

Example

The symmetric system of sinusoidal voltages of Fig. 7.2a is considered. Fig. 7.2b shows the $\alpha\beta$ space vector associated with this system. The trajectory of the space vector is a circle, since it rotates with constant amplitude and speed.

Space vector in $\alpha_2\beta_2$ reference frame is zero as well as zero sequence component. They are not shown in the Fig. 7.2.
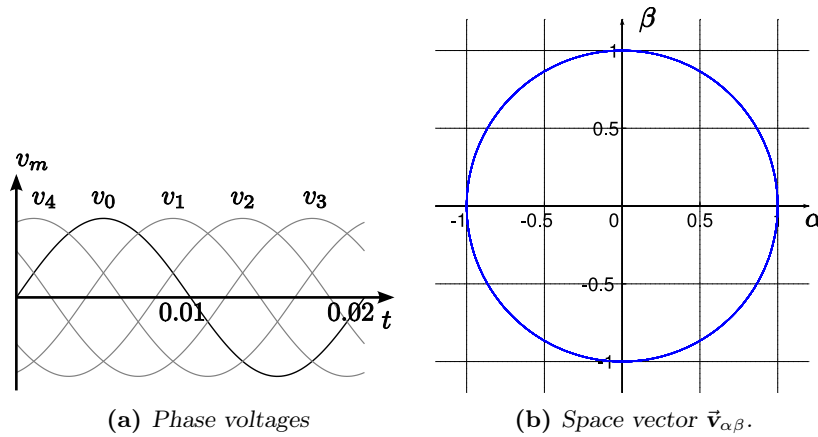
(a) *Phase voltages*

(b) *Space vector $\vec{v}_{\alpha\beta}$.*

Figure 7.2: *Symmetric system of sinusoidal voltages and space vector $\vec{v}_{\alpha\beta}$. Space vector $\vec{v}_{\alpha_2\beta_2}$ and zero sequence component v_z are zero and not reported here.*

Case 2: symmetric system with various harmonics

A symmetric system of five voltages is considered hereafter, including time harmonics in the five–phase voltages. The mth phase voltage is expressed as

$$v_m(t) = \sum_{n=1}^{\infty} \hat{V}_n \cos\left(\delta_n - nm\frac{2\pi}{5}\right) \tag{7.9}$$

where $\delta_n = n\omega t$. The aim of this section is to determine the behaviour of the space vectors in the two reference frames $\alpha\beta$ and $\alpha_2\beta_2$.

$\alpha\beta$ reference frame

The space vector is obtained as:

$$\vec{v}_{\alpha\beta} = \sum_{n=1}^{\infty} \frac{\hat{V}_n}{5} \sum_{m=0}^{4} e^{j\left(\delta_n + m(1-n)\frac{2\pi}{5}\right)} + e^{-j\left(\delta_n - m(1+n)\frac{2\pi}{5}\right)} \tag{7.10}$$

The vector $\vec{v}_{\alpha\beta}$ is different from zero only for harmonic orders equal to $n = 1 \pm 5k$, where $k = 0, 1, 2, \ldots$ This means that n is assumed with sign, and one of the two sums can be omitted. Therefore, the $\alpha\beta$ space vector can be written as:

$$\vec{v}_{\alpha\beta} = \sum_{n=-\infty}^{\infty} \hat{V}_n e^{j\delta_n} \qquad (n = 1 \pm 5k) \tag{7.11}$$

It represents a sum of rotating vectors, whose rotation direction and speed depend on the harmonic order n.

For other harmonic orders (i.e. $n \neq 1 \pm 5k$), the two terms in (7.10) are equal to zero, because they represent five vectors with the same amplitude but shifted of $2\pi/5$ radians each other. Therefore, for such harmonic orders, $\vec{\mathbf{v}}_{\alpha\beta} = 0$. Table 7.1 summarizes the order of the harmonics that are included in the $\alpha\beta$ space vector, together with the corresponding frequency ω. The rotation direction is identified by the sign.

Table 7.1: *Harmonic orders of the space vector components and corresponding frequency.*

	$\alpha\beta$		$\alpha_2\beta_2$		z	
k	n	frequency	n	frequency	n	frequency
0	$+1$	$+\omega$	$+2$	$+2\omega$	0	0
1	-4	-4ω	-3	-3ω	5	5ω
	$+6$	$+6\omega$	$+7$	$+7\omega$		
2	-9	-9ω	-8	-8ω	10	10ω
	$+11$	$+11\omega$	$+12$	$+12\omega$		
$\dots$	$\dots$	$\dots$	$\dots$	$\dots$	$\dots$	$\dots$

$\alpha_2\beta_2$ reference frame

The space vector is written as:

$$\vec{\mathbf{v}}_{\alpha_2\beta_2} = \sum_{n=1}^{\infty} \frac{\hat{V}_n}{5} \sum_{m=0}^{4} e^{\jmath\left(\delta_n + m(2-n)\frac{2\pi}{5}\right)} + e^{-\jmath\left(\delta_n - m(2+n)\frac{2\pi}{5}\right)} \tag{7.12}$$

The vector $\vec{\mathbf{v}}_{\alpha_2\beta_2}$ is different from zero for harmonic orders equal to $n = 2 \pm 5k$. It represents a sum of rotating vectors, whose rotation direction and speed depend on the harmonic order n. Assuming $n = 2 \pm 5k$ (with $k = 0, 1, 2, \dots$), the space vector can be written as

$$\vec{\mathbf{v}}_{\alpha_2\beta_2} = \sum_{n=-\infty}^{\infty} \hat{V}_n e^{\jmath\delta_n} \qquad (n = 2 \pm 5k) \tag{7.13}$$

For other harmonic orders ($n \neq 2 \pm 5k$) the two terms of (7.12) are equal to zero. Table 7.1 summarizes the order of the harmonics that are included in the $\alpha_2\beta_2$ space vector, together with the corresponding frequency, whose sign identifies the rotation direction.

Zero sequence component

From (7.8) and (7.9), the zero sequence component results in

$$v_z = \sum_{n=1}^{\infty} \hat{V}_n cos\delta_n \qquad (n = 5k) \tag{7.14}$$

The harmonic orders of v_z are also reported in Table 7.1.

Example

A symmetric system of five squarewaves is considered. The waveform of the first phase voltage is shown in Fig. 7.3a. The harmonic contents of such a waveform include all odd harmonics of order from 1 to 99.
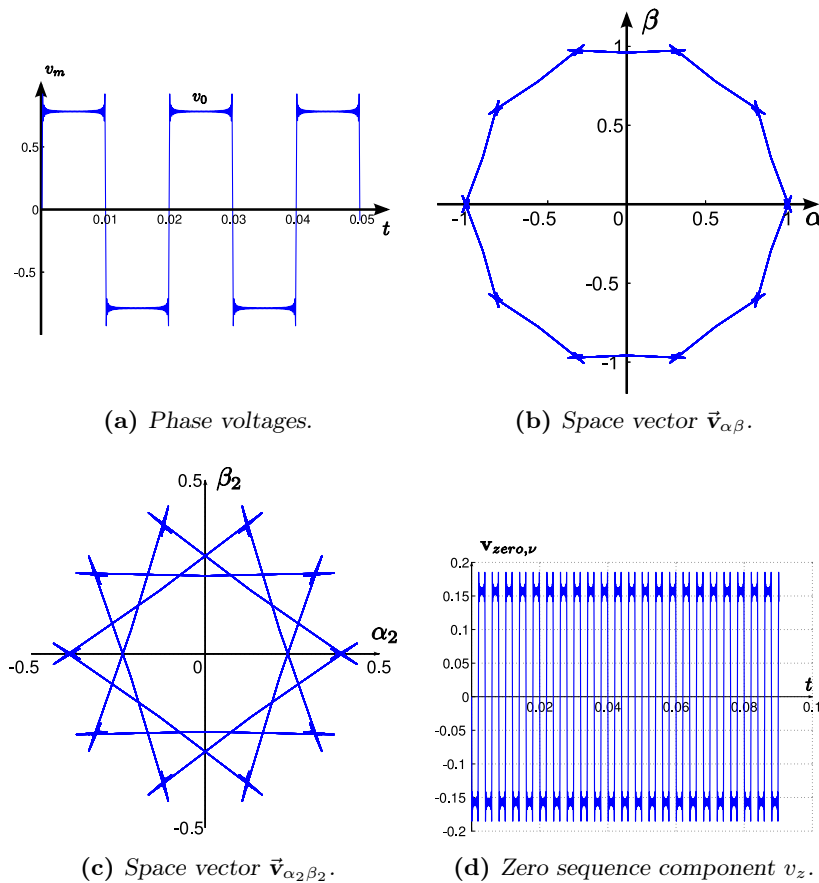

(a) *Phase voltages.*

(b) *Space vector* $\vec{v}_{\alpha\beta}$.

(c) *Space vector* $\vec{v}_{\alpha_2\beta_2}$.

(d) *Zero sequence component* v_z.

Figure 7.3: *Symmetric system formed by squarewave voltages, with corresponding space vector components.*

Fig. 7.3b shows the $\alpha\beta$ space vector trajectory. It represents a decagon, but the space vector moves along the edges of the decagon jumping from a vertex to another every tenth of period.
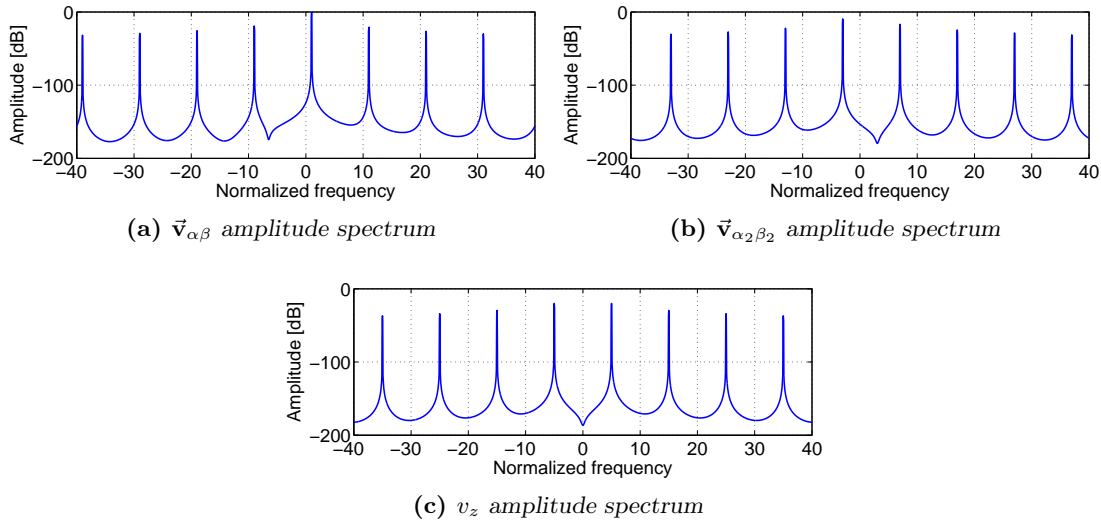
(a) $\vec{\mathbf{v}}_{\alpha\beta}$ *amplitude spectrum*

(b) $\vec{\mathbf{v}}_{\alpha_2\beta_2}$ *amplitude spectrum*

(c) v_z *amplitude spectrum*

Figure 7.4: *Amplitude spectra of space vectors associated with a system of squarewave voltages, shown in Fig. 7.3.*

Fig. 7.3c shows the $\alpha_2\beta_2$ space vector trajectory. In this case, the space vector moves along the lines of a star, jumping from a vertex to another. Fig. 7.3d shows the zero sequence component. It contains all harmonics of order multiple of 5.

It is interesting to observe the harmonic spectrum of the space vectors. Fig. 7.4 shows the spectrum of $\vec{\mathbf{v}}_{\alpha\beta}$, $\vec{\mathbf{v}}_{\alpha_2\beta_2}$ and v_z. The harmonics of the space vector components correspond to the results reported in Table 7.1.

7.3 Asymmetric systems

Case 1: only fundamental harmonic

This subsection considers a system of five sinusoidal voltages in which one phase voltage has amplitude different from the others. The asymmetric phase is the rth phase, where r can assume the values 0, 1, 2, 3, or 4. The rth phase voltage is assumed to have amplitude $\gamma_1 \hat{V}_1$ instead of $\hat{V}_1$, as in (7.2), where γ_1 is a proper factor.

$\alpha\beta$ reference frame

The space vector in $\alpha\beta$ reference frame is:

$$\vec{\mathbf{v}}_{\alpha\beta}^{(r)} = \hat{V}_1 \left(\frac{4 + \gamma_1}{5} \right) e^{\jmath\delta_1} + \hat{V}_1 \left(\frac{\gamma_1 - 1}{5} \right) e^{-\jmath\left(\delta_1 - 2r\frac{2\pi}{5}\right)} \tag{7.15}$$

With this notation, the space vector can be considered as the sum of two vectors rotating in opposite directions, whose amplitude depends on γ_1, and the initial phase depends on the asymmetric rth phase. This is sketched in Fig. 7.5, which shows these two space vectors, according to

$\gamma_1 = 0.75$. If these vectors are represented in the synchronous $d - q$ reference frame, also shown in Fig. 7.5, a vector results to be stationary, while the other results to be rotating clockwise at double frequency.
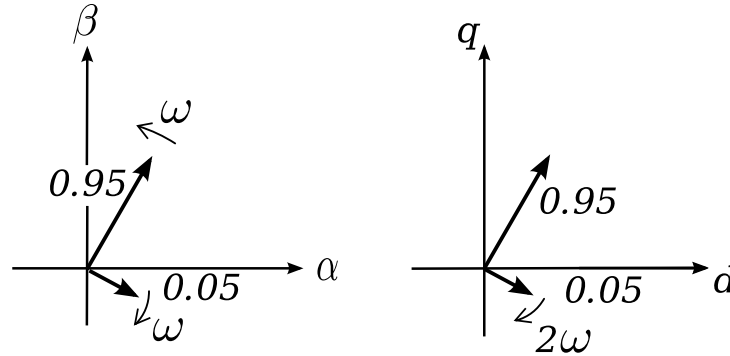

Figure 7.5: *Two rotating space vectors*

The space vector (7.15) can be expressed also highlighting the space vector found in a symmetric system (7.5). It is:

$$\vec{\mathbf{v}}_{\alpha\beta}^{(r)} = \hat{V}_1 e^{j\delta_1} + \hat{V}_1 \frac{2(\gamma_1 - 1)}{5} \cos\left(\delta_1 - r\frac{2\pi}{5}\right) e^{jr\frac{2\pi}{5}} \tag{7.16}$$

With this notation, the space vector of a system with one phase asymmetry corresponds again to the sum of two vectors. The first is rotating and it is equal to that found with a symmetric system (i.e., $\hat{V}_1 e^{j\delta_1}$). The second is pulsating, along a given direction which depends on the asymmetric phase (i.e. the rth phase). This is sketched in Fig. 7.6, which shows these two space vectors, according to $\gamma_1 = 0.75$. If these vectors are represented in the synchronous $d - q$ reference frame, also shown in Fig. 7.6, one results to be stationary, while the other results to be rotating clockwise at double frequency, describing a circle crossing the origin.
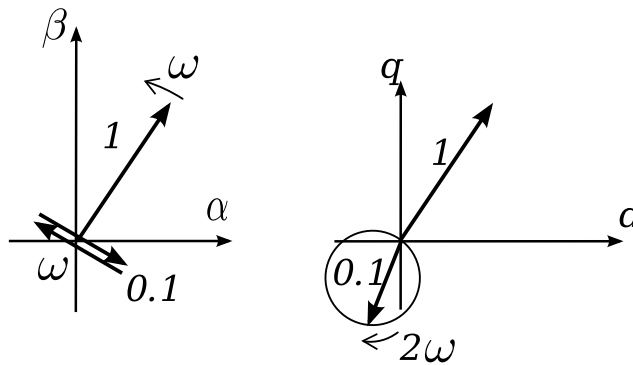

Figure 7.6: *Rotating and pulsating space vectors.*

$\alpha_2\beta_2$ reference frame

Similar considerations can be carried out in $\alpha_2\beta_2$ reference frame. The space vector with one asymmetric phase can be expressed as:

$$\vec{\mathbf{v}}_{\alpha_2\beta_2}^{(r)} = \hat{V}_1 \frac{2(\gamma_1 - 1)}{5} \cos\left(\delta_1 - r\frac{2\pi}{5}\right) e^{jr\frac{4\pi}{5}} \tag{7.17}$$

where, as above, γ_1 is the asymmetry ratio and r indicates which phase voltage is different from the others.

Zero sequence component

It is:

$$v_z^{(r)} = \hat{V}_1 \frac{(\gamma_1 - 1)}{5} \cos\left(\delta_1 - r\frac{2\pi}{5}\right) \tag{7.18}$$

Example

Fig. 7.7a shows an example of asymmetric system with only sinusoidal waveforms; in this case the voltage amplitude $\hat{V}_1$ is reduced down to 75 % of the voltage in symmetric conditions, i.e. $\gamma_1 = 0.75$. The trajectory of $\vec{\mathbf{v}}_{\alpha\beta}$ becomes an ellipse, as shown in Fig. 7.7b, where the minor and major axes depend on the asymmetric rth phase, as results from (7.15). The trajectory of $\vec{\mathbf{v}}_{\alpha_2\beta_2}$ is a straight line, as shown in Fig. 7.7c. Its direction depends on the asymmetric rth phase, as depicted by (7.17). The trajectory of v_z shown in Fig. 7.7d is a sinewave, as expected by (7.18).

Case 2: voltages with various harmonics

As above, it is possible to compute the space vectors in the $\alpha\beta$ and $\alpha_2\beta_2$ reference frames. In the following, for the sake of compactness, the whole space vectors of the asymmetric system are not reported Only the space vectors representing the difference between the asymmetric and symmetric system are considered. So that, they express the change from symmetric system due to the asymmetry. They are $\Delta\vec{\mathbf{v}}_{\alpha\beta}^{(r)}$, $\Delta\vec{\mathbf{v}}_{\alpha_2\beta_2}^{(r)}$ and $\Delta v_z^{(r)}$. The whole space vectors are achieved by summing them to the space vectors of the symmetric system (7.11), (7.13) and (7.14).

In $\alpha\beta$ reference frame, it is

$$\Delta\vec{\mathbf{v}}_{\alpha\beta}^{(r)} = \sum_{n=-\infty}^{\infty} \hat{V}_n \frac{(\gamma_n - 1)}{5} e^{j\left(\delta_n + r(1-n)\frac{2\pi}{5}\right)} \tag{7.19}$$

In $\alpha_2\beta_2$ reference frame, it is

$$\Delta\vec{\mathbf{v}}_{\alpha_2\beta_2}^{(r)} = \sum_{n=-\infty}^{\infty} \hat{V}_n \frac{(\gamma_n - 1)}{5} e^{j\left(\delta_n + r(2-n)\frac{2\pi}{5}\right)} \tag{7.20}$$

(a) *Phase voltages*

(b) $\vec{v}_{\alpha\beta}$ *trajectory*

(c) $\vec{v}_{\alpha_2\beta_2}$ *trajectory*
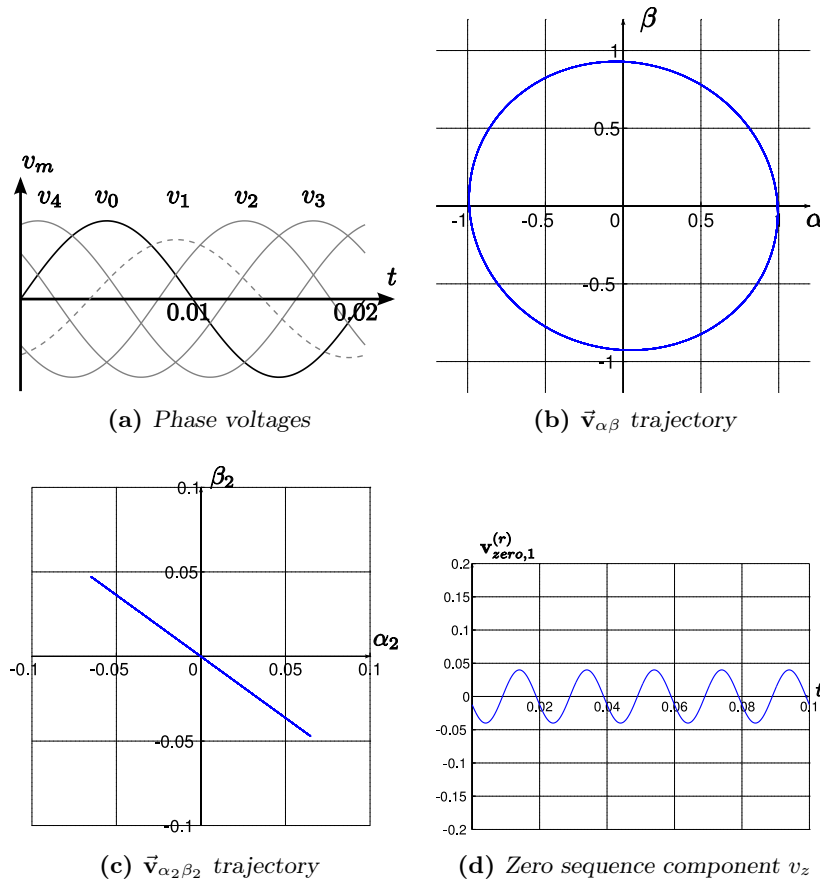

(d) *Zero sequence component* v_z

Figure 7.7: *System with sinusoidal waveforms with one asymmetric phase. Phase voltages and space vector components.*

Finally, the zero sequence component is

$$\Delta v_z^{(r)} = \sum_{n=1}^{\infty} \frac{\hat{V}_n}{5}(\gamma_n - 1)\cos\left(\delta_n - rn\tfrac{2\pi}{5}\right) \tag{7.21}$$

It is worth noticing that harmonics of any order appear in these space vector components. In other words, the asymmetry of one phase yields the rising of harmonics of any order in the space vectors, whose amplitude and phase depend on the harmonic order n and on the asymmetry factor γ_n.

From (7.19) and (7.20), for each harmonic order n, there are two vectors: one rotating clockwise and the other rotating counterclockwise, with frequency $+n\omega$ and $-n\omega$ respectively.

Table 7.2 reports amplitude and frequency of the whole space vectors, given by summing the space vectors $\vec{v}_{\alpha\beta,n(sym)}$ and $\vec{v}_{\alpha_2\beta_2,n(sym)}$ of the symmetric system, given in (7.11) and (7.13), to the space vectors $\Delta\vec{v}_{\alpha\beta,n}$ and $\Delta\vec{v}_{\alpha_2\beta_2,n}$ achieved by (7.19) and (7.20).

Table 7.2 highlights that for any frequency, there is a couple of space vectors rotating in opposite directions. This is emphasised by the sign of the frequency $n\omega$. As far as the amplitudes

Table 7.2: *Harmonic orders included in $\alpha\beta$ and $\alpha_2\beta_2$ space vector and corresponding rotation direction.*

	$\vec{\mathbf{v}}_{\alpha\beta,n(sym)} + \Delta\vec{\mathbf{v}}_{\alpha\beta,n}$					$\vec{\mathbf{v}}_{\alpha_2\beta_2,n(sym)} + \Delta\vec{\mathbf{v}}_{\alpha_2\beta_2,n}$			
	frequencies		amplitude			frequencies		amplitude	
n	$n > 0$	$n < 0$	$\omega > 0$	$\omega < 0$	n	$n > 0$	$n < 0$	$\omega > 0$	$\omega < 0$
1	ω	$-\omega$	A_1	B_1	1	ω	$-\omega$	B_1	B_1
2	2ω	-2ω	B_2	B_2	2	2ω	-2ω	A_2	B_2
3	3ω	-3ω	B_3	B_3	3	3ω	-3ω	B_3	A_3
4	4ω	-4ω	B_4	A_4	4	4ω	-4ω	B_4	B_4
5	5ω	-5ω	B_5	B_5	5	5ω	-5ω	B_5	B_5
6	6ω	-6ω	A_6	B_6	6	6ω	-6ω	B_6	B_6
7	7ω	-7ω	B_7	B_7	7	7ω	-7ω	A_7	B_7

are concerned, Table 7.2 highlights the amplitudes of the space vectors, distinguishing the positive rotating and negative rotating vectors. The impact of the space vectors $\Delta\vec{\mathbf{v}}_{\alpha\beta,n}$ and $\Delta\vec{\mathbf{v}}_{\alpha_2\beta_2,n}$ results as follows:

- where the components of the symmetric system were zero, the amplitude grows up to $B_n = \hat{V}_n(\gamma_n - 1)/5$.

- where the components of the symmetric system were not zero, see Table 7.1, the amplitude of the components of the symmetric system becomes equal to $A_n = \hat{V}_n(\gamma_n + 4)/5$.

Example 1

A system of five squarewave voltages is considered. An amplitude variation is considered in a single harmonic component of one phase voltage. The amplitude of the harmonic voltage of third order is assumed $0.99\hat{V}_3$, instead of $\hat{V}_3$. Although the trajectory of the space vectors is almost unvaried with respect to that of Fig. 7.3, their harmonic spectra allow the asymmetry to be highlighted. Note that the behavior of the amplitude spectrum is independent of the asymmetric phase.

Fig. 7.8a refers to the $\vec{v}_{\alpha\beta}$ spectrum. Two peaks appear, corresponding to the frequencies $3f$ and $-3f$, which are not present in the spectrum of the symmetric squarewave system, compare with Fig. 7.4a. It is worth noticing that the impact of the harmonic distortion on the spectrum is evident also with a very small asymmetry (i.e. $\gamma_3 = 0.99$).

Fig. 7.8b refers to the $\vec{v}_{\alpha_2\beta_2}$ spectrum. In this case, the rise of the peak corresponding to the frequency $3f$ is evident. The amplitude of the component at $-3f$ (already present in a symmetric system) is reduced, as also reported in Table 7.2.
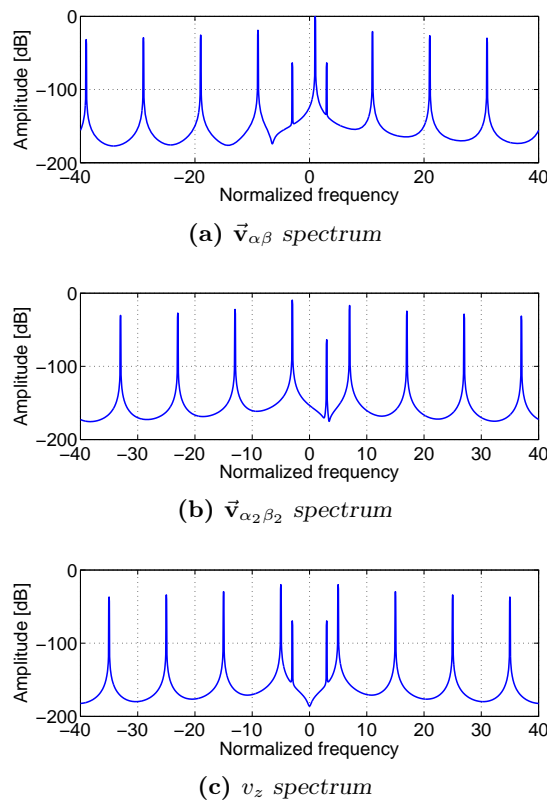

(a) $\vec{v}_{\alpha\beta}$ spectrum

(b) $\vec{v}_{\alpha_2\beta_2}$ spectrum

(c) v_z spectrum

Figure 7.8: *Amplitude spectra of an asymmetric system of squarewave voltages: only harmonic of 3th order in one phase is reduced of 1% ($\gamma_3 = 0.99$).*

The effect of the asymmetry is a reduction of such a component, however, the decrease is small and difficult to be recognized.

Fig. 7.8c shows the v_z amplitude spectrum, showing again the rise of the components at $3f$ and $-3f$.

Example 2

Also referring to a system of five squarewave voltages, a variation is considered in all the harmonic components of one phase. The voltage amplitude of all harmonics is assumed changed in $0.99\hat{V}_n$.

Fig. 7.9a refers to the $\vec{v}_{\alpha\beta}$ spectrum. As expected, the peaks appear at any frequency, regardless if they are present or not in the spectrum of the symmetric squarewave system, as reported in Table 7.2. Fig. 7.9b refers to the $\vec{v}_{\alpha_2\beta_2}$ spectrum. Also in this case, all harmonics are present in the spectrum. Fig. 7.9c shows the v_z amplitude spectrum, showing again the rise of all the harmonics.

(a) $\vec{v}_{\alpha\beta}$ spectrum

(b) $\vec{v}_{\alpha_2\beta_2}$ spectrum

(c) v_z spectrum
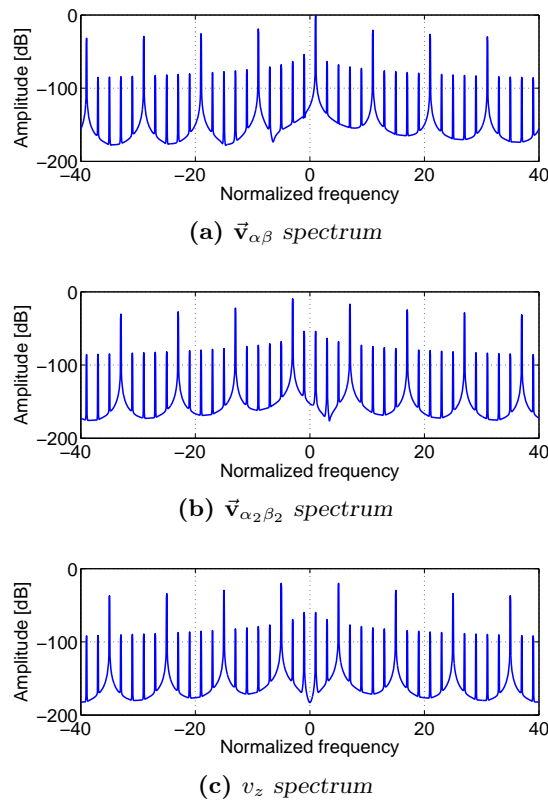
Figure 7.9: *Amplitude spectra of a asymmetric system of squarewave voltage: all harmonics in phase 1 are reduced of 1 % ($\gamma_n = 0.99$ for any odd ho).*

7.4 Simulation results

The five–phase motor shown in Fig. 5.2 has been simulated by using finite elements. The motor is assumed to operate under nominal load, and the phase currents are imposed as sources of the field problem. The five–phase voltage behaviours are computed from the field solution. The space vector components are computed by means of (7.1) and the corresponding spectra are reported in Fig. 7.10.
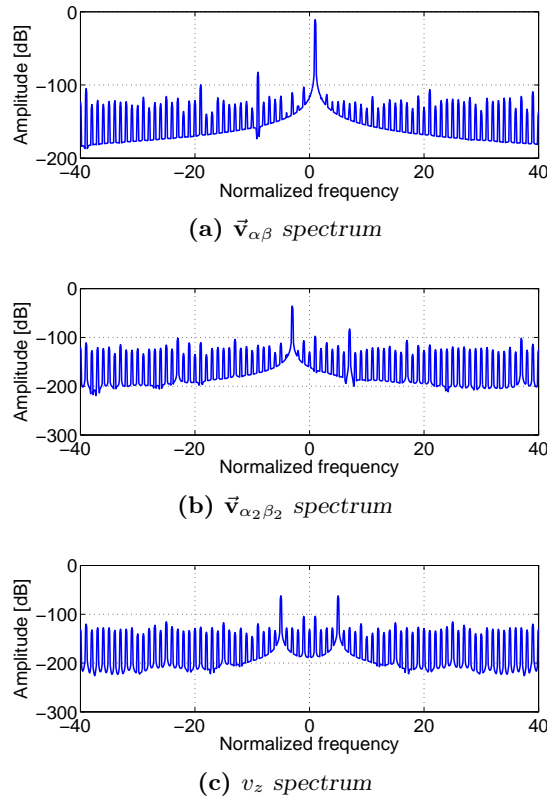

(a) $\vec{\mathbf{v}}_{\alpha\beta}$ spectrum

(b) $\vec{\mathbf{v}}_{\alpha_2\beta_2}$ spectrum

(c) v_z spectrum

Figure 7.10: *Space vector amplitude spectra of a healthy machine.*

The same motor has been simulated assuming that some turns of one coil are short–circuited. The number of short–circuited turns are one hundredth of the total number of turns of the coil. In this faulty operating condition, the five–phase voltage behaviours are computed again, together with the corresponding space vector components from (7.1). The corresponding spectra are reported in Fig. 7.11.

In the $\vec{\mathbf{v}}_{\alpha\beta}$ spectrum, there is an evident rise of the harmonics of frequency $-f$, $\pm 3f$ and $5f$. They are noticeable in Fig. 7.11a. A high distortion appears in the $\vec{\mathbf{v}}_{\alpha_2\beta_2}$ spectrum, as evident in Fig. 7.11a. Also the spectrum of the zero sequence component shows an evident distortion, see Fig. 7.11c.
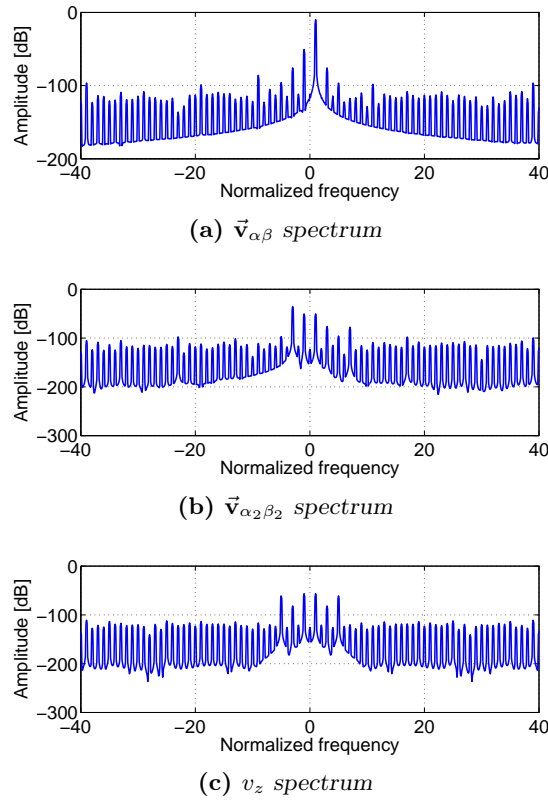
(a) $\vec{\mathbf{v}}_{\alpha\beta}$ *spectrum*

(b) $\vec{\mathbf{v}}_{\alpha_2\beta_2}$ *spectrum*

(c) v_z *spectrum*

Figure 7.11: *Space vector amplitude spectra in case of short–circuited turns in one coil.*

7.5 Conclusions

This chapter investigates the impact of the asymmetry in one phase of a five–phase machine. The analysis is carried out by means of the space vectors, highlighting a vector in $\alpha\beta$ and a vector in $\alpha_2\beta_2$ reference frame, and the zero sequence component.

It is shown that the asymmetry of one phase of the system causes a variation of the harmonic amplitude of any order. The harmonics that are present in the space vectors of a symmetric system decrease slightly, while harmonics that are not present in the space vectors of a symmetric system grow up. The amplitude of these harmonics depend on the asymmetry level.

As a diagnosis criterium, it is convenient to check up on the harmonics that are not present in the symmetric system (i.e. those harmonics that are not included in Table 7.1), for instance the harmonics of second and third order in v_α, v_β, or the harmonic of first order in v_{α_2}, v_{β_2}.

Then, since the amplitude of the harmonics decreases with the order of the harmonic themselves, it is more convenient to limit the diagnosis to few harmonics close to the fundamental one. Although the problem of discriminate the asymmetry due to a fault or due to a mechanical eccentricity, or to a manufacturing inaccuracy, is not solved, the chapter results can be adopted for diagnosis purposes. In this case, a mapping of the behaviour of the electrical machine seems to be necessary to correctly identify the fault event.

CHAPTER 8

Fault detection of five–phase PM machines

Abstract

The chapter focuses on the fault detection of a five-phase Permanent-Magnet machine.

The effects of a limited number of short-circuited turns is investigated by theoretical and Finite Element (FE) analysis, and then a procedure for fault detection is proposed, focusing on the severity of the fault (i.e. the number of short-circuited turns and the related current).

The novel fault detection proposed method is capable of an early detection of open and short circuit faults in a drive with current regulation. The advantages of the proposed method are that it is on-line and non-invasive and provides alert signals at an early stage. In fact it does not require any dedicated sensor for the fault detection.

In particular, the diagnostic technique detects turn–to–turn short–circuit faults. The detection of such a fault is an hard task, since the distortion of the flux is limited and the asymmetry is very small (especially in case of a low number of short–circuited turns), even though the short–circuit current is high. This procedure provides quantitative information about fault severity and the capability of identifying the faulty phase.

The main drawback is that a measurement of the current (in a VSI fed drive) or the voltage (in a CSI fed drive) of each phase is required. Moreover a dedicated power converter must be developed with a multiphase output [49], [50].

After a modeling of the faulty machine, an accurate FE modeling of the machine is described, where FE results are used to compute the PM flux linkage in a faulty phase. Eventually the influence of the faults on machine electric quantities is investigated and a fault detection procedure is validated by simulation and experiments.

8.1 Modelling of five-phase PM Machines

The five-phase PM machine described in chapter 5 is used to validate the proposed fault detection method.

As seen before, the special design of Fig. 5.3b is characterised by a mutual coupling between phases equal to zero, even in the presence of iron saturation [45]. Hence each phase can be modeled independently. The phase voltage can be expressed by

$$v_k(t) = e_k(t) + R\,i_k(t) + L\,\frac{d\,i_k(t)}{d\,t} \tag{8.1}$$

the back emf is expressed by

$$e_k(t) = \frac{d\,\lambda_{mk}(t)}{d\,t} \tag{8.2}$$

with k= 0, 1, …, 4. $\lambda_{mk}(t)$ is obtained from FE computations. Eventually the phase current is expressed by

$$i_k(t) = I_M \, \sin\left(\theta + \frac{2\,k\,\pi}{5}\right) \tag{8.3}$$

A current controlled multi-phase drive is used, where symmetrical sinusoidal currents are forced. Specifically each phase current is independently regulated by a hysteresis control that drives the H-bridge switches, Fig. 5.4.

8.2 Modelling a partial coil short circuit fault

The fault modeled is the partial short circuit of a coil, where a part of the turns in a coil is short-circuited due to insulation deterioration. Under these conditions the faulty phase can be modeled adding a short-circuited dummy winding mutually coupled to the remaining healthy part of the phase [47]. The model of a healthy phase is described by

$$v \;=\; Ri + L\frac{di}{dt} + \frac{d\lambda_{pm}}{dt}, \tag{8.4}$$

where v and i is the phase voltage and current, and the healthy phase parameters are: resistance R, inductance L and the PM flux linkage λ_{pm}.

The partial short circuit is characterised by n, the number of short-circuited turns, where N is the total number of turns of the phase. The electrical model of the fault is shown in Fig. 8.1. For the dummy winding a linear relationship is assumed between the number of shorted turns n and the resistance and PM flux linkage, and a quadratic relationship between the number of shorted turns and the inductance.
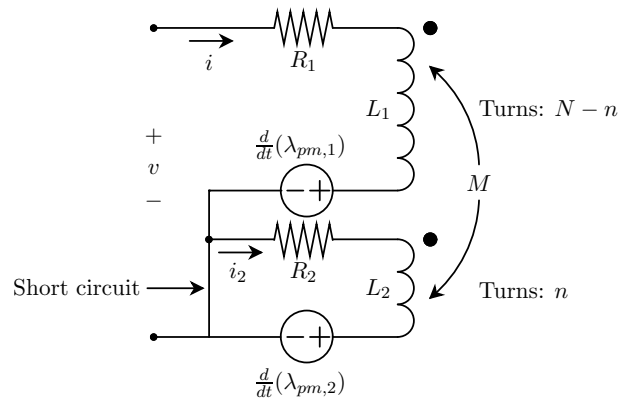
Figure 8.1: *Phase model of the five-phase PM machine in case of shorted turns fault.*

The electrical parameters for the two windings in Fig. 8.1 can be expressed as

$$R_1 = R \frac{N-n}{N} \qquad\qquad R_2 = R \frac{n}{N} \qquad (8.5)$$

$$L_1 = L \left(\frac{N-n}{N}\right)^2 \qquad\qquad L_2 = L \left(\frac{n}{N}\right)^2 \qquad (8.6)$$

$$\lambda_{pm,1} = \lambda_{pm} \frac{N-n}{N} \qquad\qquad \lambda_{pm,2} = \lambda_{pm} \frac{n}{N}. \qquad (8.7)$$

It is assumed that no leakage flux is present between the two parts of the coil, so that the mutual inductance is $M = \sqrt{L_1 L_2}$.

Applying the equivalent transformer model the reduced electrical circuit for the phase can be found. The equivalent transformer model is reported in Fig. 8.2.
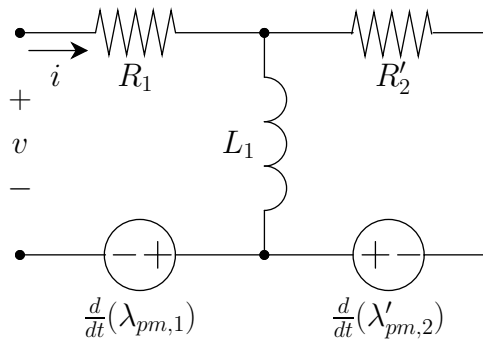
Figure 8.2: *Equivalent model under fault conditions.*

The magnetising inductance of the model is equal to the primary inductance L_1 under the assumption that no leakage flux is present.

The resistance and PM flux linkage on the secondary side (short-circuited part) referred to

the primary side are

$$R'_2 = R\frac{(N-n)^2}{Nn} \tag{8.8}$$

$$\lambda'_{pm,2} = \lambda_{pm}\frac{N-n}{N}. \tag{8.9}$$

The model of Fig. 8.2 can be rearranged by means of the Thevenin theorem. With simple computations the equivalent Thevenin parameters for a phase under fault are obtained:

$$R_{eq}(\omega) = R\frac{N-n}{N}\cdot\frac{1+\omega^2\frac{L^2 n}{R^2 N}}{1+\omega^2\left(\frac{nL}{NR}\right)^2} \tag{8.10}$$

$$L_{eq}(\omega) = L\left(\frac{N-n}{N}\right)^2\cdot\frac{1}{1+\omega^2\left(\frac{nL}{NR}\right)^2} \tag{8.11}$$

$$\lambda_{pm,eq}(s) = \lambda_{pm}\frac{N-n}{N}\cdot\frac{1}{1+\frac{nL}{NR}s} \tag{8.12}$$

For frequencies $\omega \ll \frac{NR}{nL}$ the resistance and PM flux linkage decreases linearly and the inductance quadratic with the number of short circuited turns n.

Fault Influence

From the equivalent model it is possible to establish the parameters variation due to a fault.

The equivalent phase impedance $Z_{eq} = R_{eq} + sL_{eq}$ normalised with respect to the healthy resistance is reported in Fig. 8.3 as bode diagrams.

For frequencies $\omega \gg \frac{NR}{nL}$ the phase impedance becomes dominantly resistive. For frequencies below, the impedance change are more attenuated.

Hence the detection of a small short circuit e.g. $\frac{n}{N} < 5\%$ at low frequencies may be difficult, as the electrical characteristic of the phase does not change significantly. Using a high frequency signal (i.e. a frequency above $\frac{NR}{nL}$) is it possible to detect small short circuit faults because the phase impedance angle changes significantly as observed in Fig. 8.3.
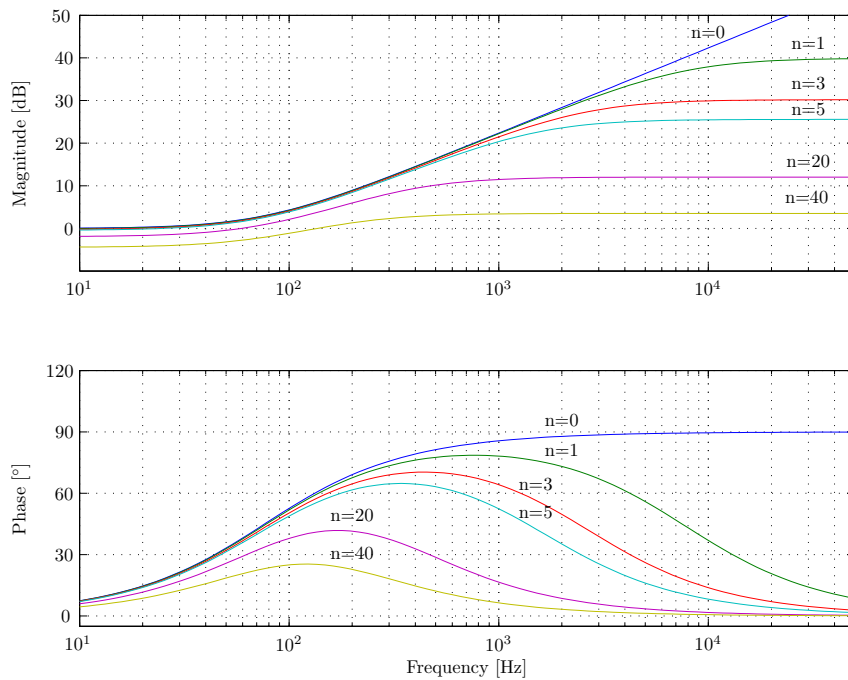
Figure 8.3: *Bode diagram of the phase impedance $\frac{Z_{eq}}{R}$.*

8.3 FE Modelling of the five-phase PM Machine

Finite Element (FE) analysis is adopted to compute both PM flux linkages and inductances of the five–phase machine. The FE analysis is carried out imposing the currents and computing the flux linked by the phase coils. A cross–section of the machine is shown in Fig. 8.4. The flux linkages are computed at no–load, see Fig. 8.4a, varying the position of the rotor, so that the complete waveform of the flux linkage is predicted.

To this aim a zero winding current is forced while the rotor spins with small angular steps $\delta\theta$ up to a polar pitch equal to $360/p = 40$ degrees.

The choice of the angular step $\delta\theta$ is critical. In fact it is below limited by the resolution of results, and it is above by the size of the parts of the assembly. In fact a numerical high frequency noise would be generated if a very small angular step is used. An angular step $\delta\theta = 0.2$ mechanical degrees was chosen as an optimal trade-off.

This is useful for the spectral analysis and the computation of the signatures in case of faulty conditions. The inductance is computed removing the PMs from the rotor, imposing a current only in the coils of one phase, see Fig. 8.4b. Then, the ratio between the flux linkage and the current is computed. Finally, the analytical model is completed by adding the resistance and the end–winding effects that are not included in the two–dimensional FE analysis [51].

In the event of a short–circuit fault of some turns, the short–circuit current is computed by means of the lumped–parameter circuit and then forced in the slots where are the short–circuited turns. The value of short–circuit current is varied as it depends on the flux linkage rate of change.
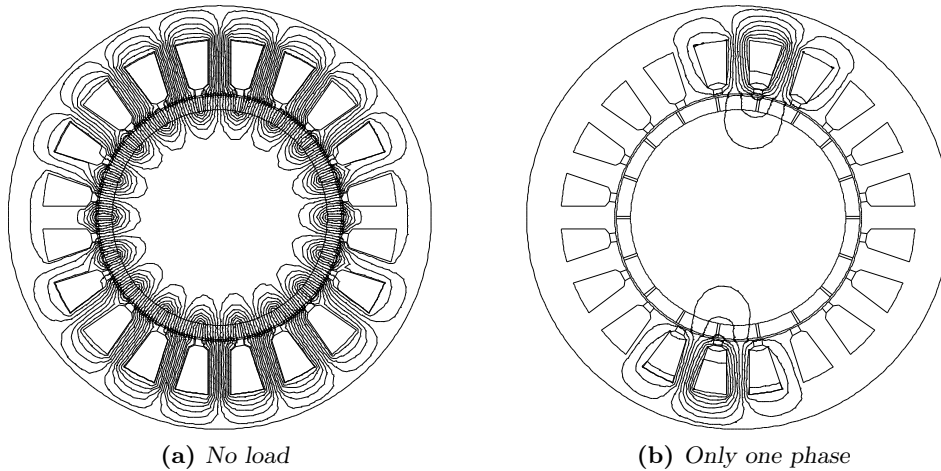
(a) *No load*   **(b)** *Only one phase*

Figure 8.4: *Flux map of the five–phase motor* (a) *at no load and* (b) *with a current only in one phase (without PMs).*

8.4 Five–phase motor drive diagnosis procedure

The task of an effective diagnostic index is to give a clear information about the occurred faults, even when it involves only a part of the machine. The index has to recognize the asymmetry of the phases, without giving false indications on the healthy components.

The effect of a turn–to–turn short–circuit is analysed using the symmetrical components transformation [16] [48]. Hence the fault can be detected checking the additional harmonics, and since their amplitude decreases with ν the most effective diagnostic index is the amplitude of the component of the space vector $v_{\alpha\beta}$ at $-f_s$, where $f_s = 2\pi\omega$ is the supply frequency.

With similar considerations for the space vector in $\alpha_2\beta_2$ in the event of a fault all the harmonics appear. Hence the most effective diagnostic index is the amplitude of the component of the space vector $v_{\alpha_2\beta_2}$ at $3\,f_s$ (or at f_s).

With some further simplification the location of the faulty phase can be identified, as detailed in the next section.

Thus, in the event of a fault that modifies the fundamental component of one phase, there are two key effects in $\alpha_2\beta_2$ reference frame:

- one harmonic of fundamental order appears in the space vector (harmonic that is not present in healthy conditions);

- the trajectory of the space vector is a straight line, whose direction is bound to the faulty phase, and can be use for its detection.

8.5 Simulation and Experimental results

FE analysis results

As discussed in the previous section, in the event of short–circuit, an increase of the harmonic contents is expected in both space vectors $\vec{v}_{\alpha\beta}$ and $\vec{v}_{\alpha_2\beta_2}$. The FE analysis is coupled with the analytical model for the computation of the electromotive forces and the short–circuit currents. From the FE analysis in faulty operating conditions, the phase flux linkages are computed again, and they are transformed to achieve the space vectors on which the harmonic spectrum is computed.

Fig. 8.5 shows the spectrum of the space vector of $\vec{v}_{\alpha\beta}$ for the five–phase PM machine in case of healthy operating conditions and in case of 20, 40 and 60 short–circuited turns.

(a) *Component at frequency $f = -150Hz$*   **(b)** *Component at frequency $f = -50Hz$*

(c) *Component at frequency $f = 50Hz$*   **(d)** *Component at frequency $f = 150Hz$*
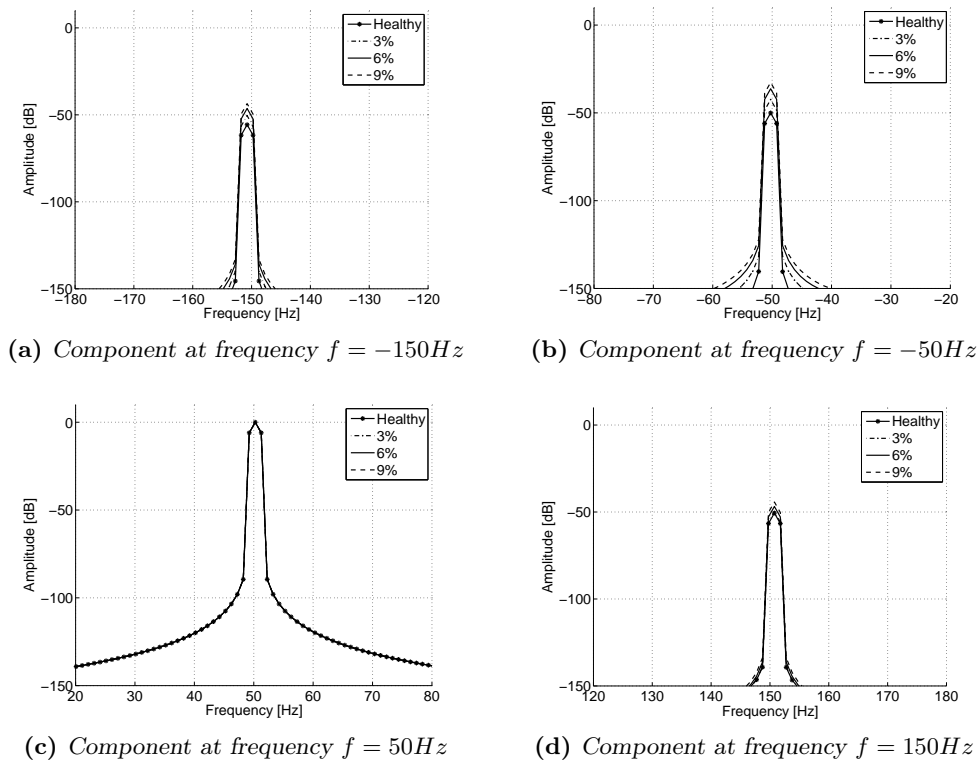
Figure 8.5: *Spectrum of $\vec{v}_{\alpha\beta}$ for the five–phase PM machine in case of healthy conditions (star–marked line), $n/N =\simeq 3$ % short–circuited turns (dash–dotted line), $n/N =\simeq 6$ % short–circuited turns (solid line) and $n/N =\simeq 9$ % short–circuited turns (dashed line).*

Being N=692, the percentage of short–circuited turns is about 3 %, 6 % and 9 %, respectively. In Fig. 8.5b, an enlargement of the behaviour around the frequency $-f_s$ is shown (the supply frequency is $f_s = 50$ Hz). The increase of the amplitude of the harmonic of such order, is evident.

The results show that the amplitude of the component at $-f_s$ increases with the number of short–circuited turns. On the contrary, the amplitude of other components, shown in Figs. 8.5a, 8.5c and 8.5d, at different frequencies, yields no useful information for a reliable fault detection,

since its variation is smaller than the variation of the component at $-f_s$. Since the variation of the amplitude of the component at $-f_s$ of $\vec{v}_{\alpha\beta}$ is significant, it can be an efficient quantitative diagnostic index. Together with the fault detection, this index can yield information about its severity (i.e. the number of short-circuited turns).

As for the polar representation of the space vector, the trajectory is an ellipse in healthy conditions, but it results to be deformed in the event of fault. As explained in chapter 7, the deformation is in the direction of the faulty phase.

At last, Fig. 8.6 shows the spectrum of the $\vec{v}_{\alpha_2\beta_2}$. As expected from the theoretical analysis, the components at frequency $-f_s$, f_s and $3f_s$ (shown in Fig. 8.6c and 8.6d respectively) increase almost proportionally to the number of the short–circuited turns.
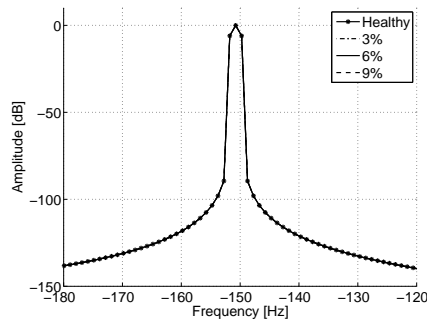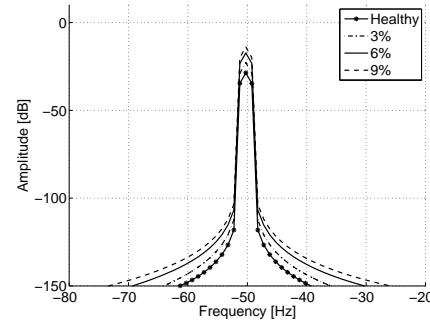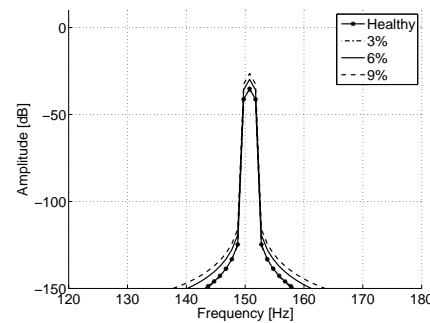

(a) Component at frequency $f = -150$ Hz

(b) Component at frequency $f = -50 Hz$
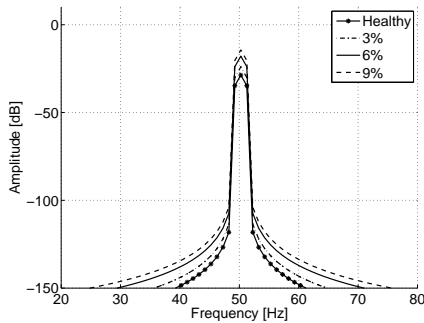
(c) Component at frequency $f = 50$ Hz

(d) Component at frequency $f = 150$ Hz

Figure 8.6: Spectrum of $\vec{v}_{\alpha_2\beta_2}$ for the five–phase PM machine in case of healthy conditions (star–marked line), $n/N = \simeq 3$ % short–circuited turns (dash–dotted line), $n/N = \simeq 6$ % short–circuited turns (solid line) and $n/N = \simeq 9$ % short–circuited turns (dashed line).

Experimental validation of the model

Some experimental tests were made to validate the equivalent model.

In order to simulate the partial short–circuit fault, 4 turns are added in a coil of one phase of the five–phase motor prototype. Two turns are wound in the same direction of the phase coil and short–circuited. The length of such a two–turn coil is so as to allow short–circuit current to be measured. The other two turns are for measuring the induced voltage. The same two–turn coil can be connected in series and with opposite direction to the phase coil, so as to reproduce the decrease of MMF caused by the loss of the two turns.

Fig. 8.7 shows the measured short–circuit current in the two short–circuited turns, together with the induced voltage in the other two opened turns, when the rotor runs at 600 r/min (i.e. about 565.5 rad/s). Induced voltage and current are in phase. As expected, with a low number of short–circuited turns, the circuit impedance is mainly resistive, and the inductive part of the impedance is negligible.
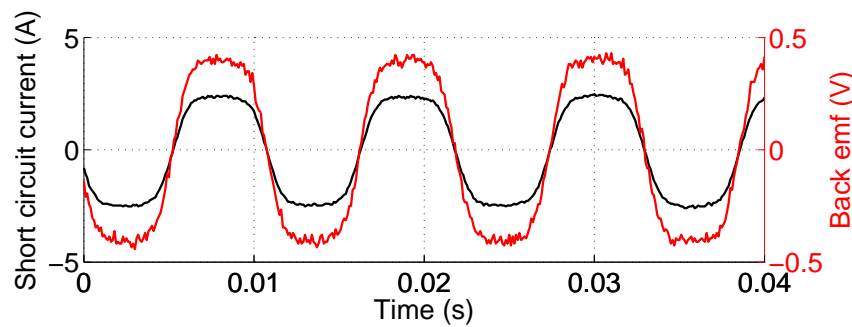

Figure 8.7: *short–circuit current and back emf with a 2–turns fault*

Fig. 8.8 shows the phase current according to a complete short–circuit of the phase coil, at rotor speed of 600 r/min. It also shows the induced voltage in the opened two–turn coil. The phase displacement between the two waveform confirms that with a large number of short–circuited turns the inductance has not to be neglected.
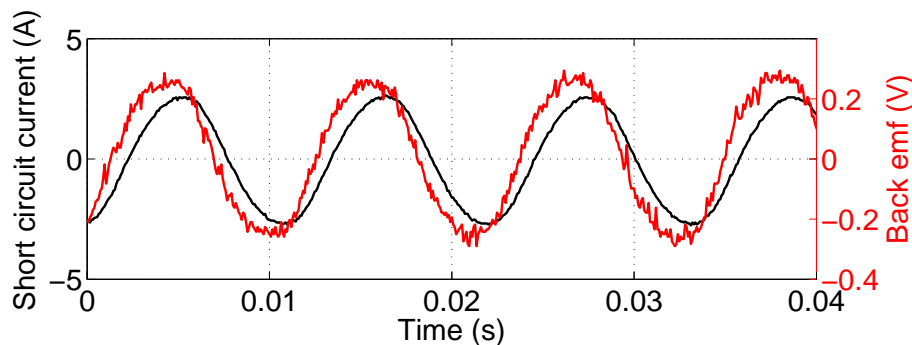

Figure 8.8: *short–circuit current and back emf with a whole winding fault*

Fig. 8.9 shows the measured short–circuit current and the induced voltage versus rotor speed, according to a complete short–circuit of the phase coil. There is a satisfactory match between

the predictions by using the analytical model and the experimental results. The deviation is probably due to a local variation of the magnetic loading in the stator iron, especially at the higher currents, that is not considered in the analytical model. In fact, the short–circuit current yields a flux that drives down the PM flux.

It is also noticing that, at higher and higher speed, the short–circuit current tends to become constant and equal to $I_{shc} = \lambda_{pm}/L$.
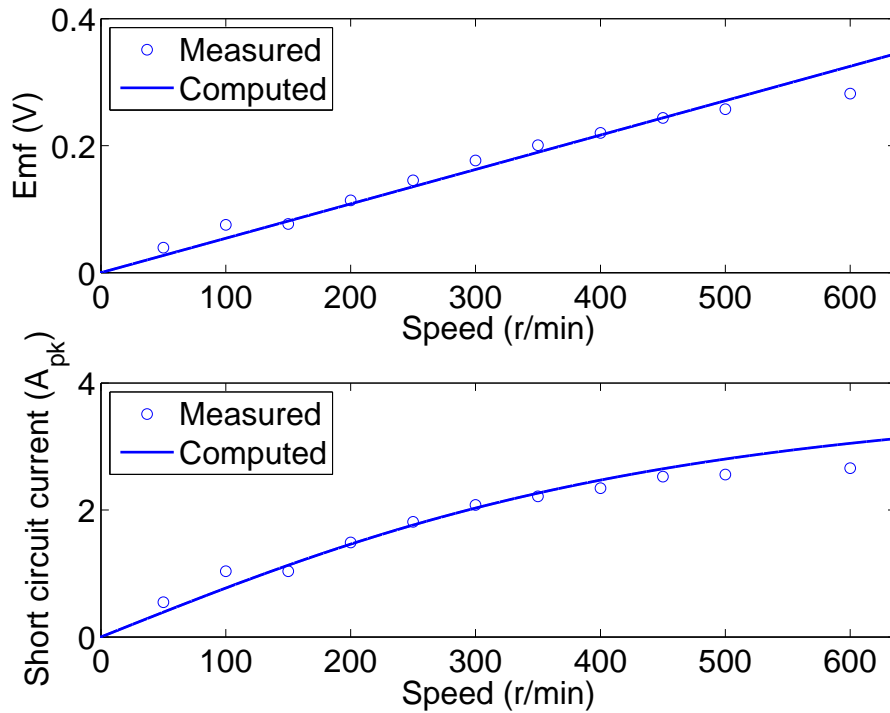

Figure 8.9: *Full short–circuit induced voltage and current versus rotation speed*

From the tests presented above, it appears that the analytical model adopted results to be appropriate to describe the faulty phase behavior. It will be used in the following, for successive considerations.

Further tests

Other measurements have been carried out on another motor prototype, with the aim to verify the circuital model proposed for the partial short–circuit fault. The winding of one phase has 88 turns, constituted by the series connection of 6 coils: two coils made by 22 turns, and four made by 11 turns. The terminals of these coils are accessible from the outer side of the motor. In this way it is possible to short–circuit the winding portions with steps of 1/8 of winding (i.e. 11 turns each step). Measurements have been done for different speeds (from 200 to 600 rpm, with steps of 200 rpm) and with 11, 22, 33 and 44 short circuited turns. Terminal voltage and short–circuit current have been measured in the phase under consideration, with and without a

terminal load. Some comparisons among measurements and analytical model have been carried out.

Measurements without load

First, the terminal voltage and the short circuit current have been measured in the prototype. The motor has been dragged at different speeds and, for each speed, a different number of turns have been short circuited. Figs. 8.10 and 8.11 show the results compared with the analytical ones. Circle marks refers to the computed voltage and the short circuit current. The results of the measurements are drawn using solid line.
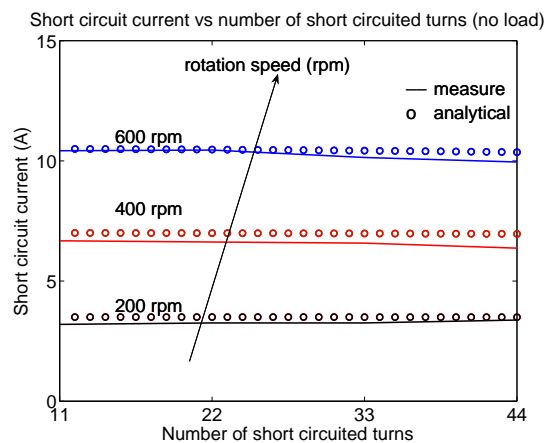

Figure 8.10: *Comparison among measurements and analytical results: short circuit current vs number of short circuit turns, without load*
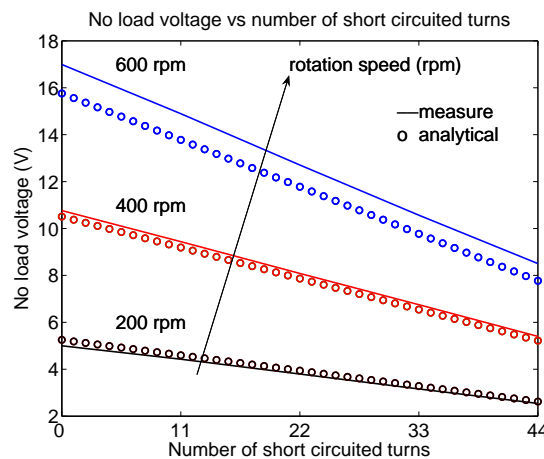

Figure 8.11: *Comparison among measurements and analytical results: no load voltage vs number of short circuit turns*

Load measurements

In this case, a load resistance of about $20\,\Omega$ has been connected to the phase terminals. The voltage across the resistance, the load current and the short circuit-current have been measured for different speeds and with different number of short–circuited turns. Figs. 8.12, 8.13 and 8.14
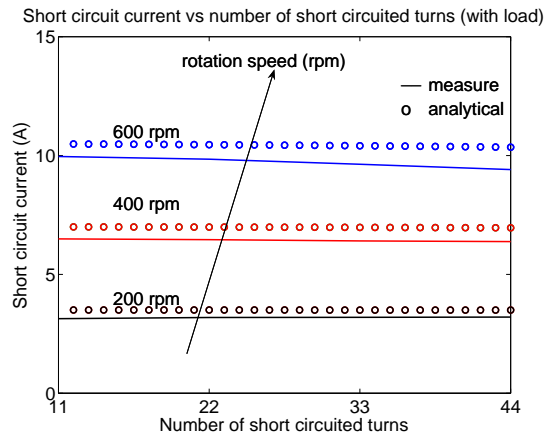

Figure 8.12: *Comparison among measurements and analytical results: short circuit current vs number of short circuit turns, with load*
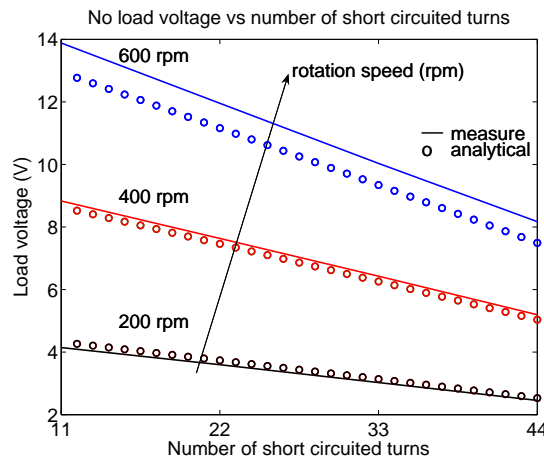

Figure 8.13: *Comparison among measurements and analytical results: load voltage vs number of short circuit turns*

show, using circle marks, the computed load voltage and current and the short–circuit current. The results of the measurements are drawn using solid line. Measurements show that there is a quite good agreement with the results obtained from the proposed analytical circuital model. For high speed (i.e. 800 and 1000 rpm) a slight difference have been found between measurements and analytical results, probably due to saturation effects.
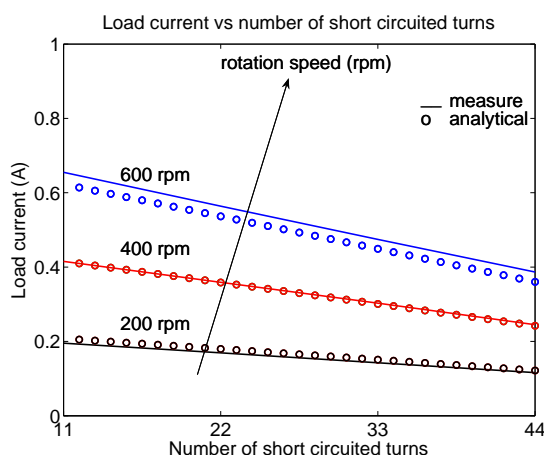
Figure 8.14: *Comparison among measurements and analytical results: load current vs number of short circuit turns*

8.6 Further experimental tests

Fig. 8.15 refers to the measurement done on the 5–phase prototype available in laboratory; in this prototype only two turns of one phase (phase 4) can be short–circuited. At first, these
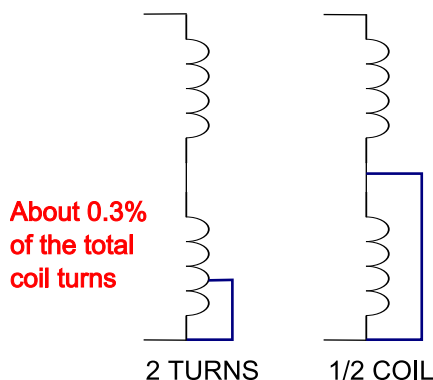

Figure 8.15: *Measurement set up*

two turns have been short circuited on phase 4. Then, one of the two coils of phase 4 has been short circuited; the latter situation corresponds to half a phase short circuited. No load voltages have been measured, dragging the rotor at the speed of 333 rpm, to achieve the frequency of 50 Hz. Because of some oscilloscope limitations, only 4 voltage have been measured. Fig. 8.16 shows the measured no load voltage in healthy case, i.e. no turns are short circuited.
Fig. 8.17 shows the measured no load voltage when 2 turns are short circuited.
Fig. 8.18 shows the measured no load voltage when half a coil is short circuited.

It can be noticed that, when only 2 turns are short circuited, there is no visible effect on the no load voltages. It is due to the very low number of short circuited turns, equal to about 3 % of the total turns of one phase coil. The variation is difficult to bo be detected also when harmonic analysis is carried out. Even thought the proposed diagnosis technique can be applied,
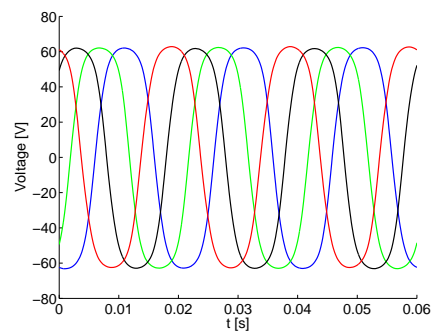
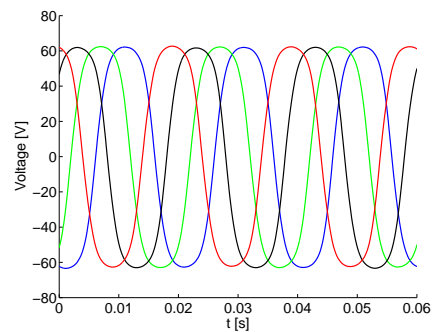**Figure 8.16:** *No load voltage in healthy case*

Figure 8.17: *No load voltage with 2 short–circuited turns*

the limited voltage distortion make difficult the fault detection.

On the other hand, when half a coil is short circuited, the effect on the voltages is clearly visible, affecting the other phase voltages as well.

It is expected that, for a reasonable number of short circuited turns, there could be a satisfactory effect in terms of voltage space vector analysis. It is estimated that the diagnosis technique allows the fault to be detected when at least 10 % of the turns of one phase winding are short circuited.
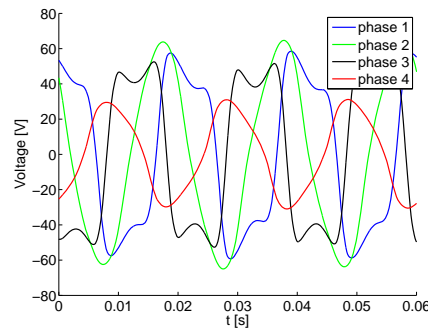
Figure 8.18: *No load voltage with one of the two coils of phase 4 short–circuited*

8.7 Conclusions

A five-phase PM machine has been designed for fault tolerant applications. It is characterised by a mutual inductance equal to zero and a high self inductance, in order to limit the short circuit current. However, with a limited number of short-circuited turns the current in the short-circuited turns increases with ω and the behavior is almost purely resistive, so that back emf and current are in phase. Only the resistance limits the short circuit current, thus it is mandatory to detect quickly the fault in case of a limited number of short-circuited turns.

A proper model of the phase winding has been developed in order to investigate the behavior of the machine under these conditions. Some experiments have been carried out so as to validate the effectiveness of the model.

The detection of the short–circuit fault was investigated relying on the frequency analysis of the space vectors of the five–phase motor, provided that the electrical quantities of each phase are measured. It is proved that the partial short–circuit fault can be efficiently detected by monitoring the amplitude of the harmonic components of the space vectors in the $\alpha\beta$ and $\alpha_2\beta_2$ reference frame. The amplitude of the harmonic component at frequency $-f_s$ in $\alpha\beta$ and $+3f_s$ in $\alpha_2\beta_2$ can be used to check the fault severity.

Moreover under some assumptions it is possible to identify the location of the faulty phase, using the polar representation of the space vector in $\alpha_2\beta_2$.

CHAPTER 9

Short–circuit fault diagnostic index

Abstract

The chapter focuses on a new diagnostic index for fault detection of a five-phase permanent-magnet machine. This machine has been designed for fault tolerant applications, and it is characterized by a mutual inductance equal to zero and a high self inductance, in order to limit the short–circuit current.

This chapter defines a diagnostic index for stator fault detection based upon the combination of information from two different reference frames.

Both analytical and simulation analysis are adopted to validate the new diagnostic index. The analytical results are currently being validated by experiments on a dedicated test bed. The chapter contribution is the definition of a novel fault detection index, which works as digital signal, is not dependent by the harmonic content of the signal used, and gives a DC output equal to zero in healthy condition and different from zero during a fault. The idea is to develop a reliable index capable of an early detection of short–circuit faults. This is an on–line and non–invasive method, which uses the measured voltage of each phase to construct the index and to detect the fault, in order to provide alert signals at an early stage. In fact, it does not require any dedicated sensor for the fault detection.

Here a method is proposed for the detection of the turn–to–turn short–circuit fault. The detection of this kind of fault is a hard task, since the distortion of the flux is limited and the asymmetry is very small (especially in case of a low number of short–circuited turns), even though the short–circuit current is high.

9.1 The Diagnostic Index

Five–phase reference frame

The task of an effective diagnostic index is to give a clear information about the occurred faults, even when it involves only a part of the machine. The index has to recognize the asymmetry of the phases, without giving false indications on the healthy components.

The effect of a turn–to–turn short–circuit is analyzed using the symmetrical components transformation [16], [48]. The transformation from the phase components to the orthogonal components is achieved by

$$
\begin{bmatrix} v_\alpha \\ v_\beta \\ v_{\alpha_2} \\ v_{\beta_2} \\ v_0 \end{bmatrix} = K \begin{bmatrix} \Re\left(\dot{a}^0 \quad \dot{a}^1 \quad \dot{a}^2 \quad \dot{a}^3 \quad \dot{a}^4\right) \\ \Im\left(\dot{a}^0 \quad \dot{a}^1 \quad \dot{a}^2 \quad \dot{a}^3 \quad \dot{a}^4\right) \\ \Re\left(\dot{a}^0 \quad \dot{a}^2 \quad \dot{a}^4 \quad \dot{a}^6 \quad \dot{a}^8\right) \\ \Im\left(\dot{a}^0 \quad \dot{a}^2 \quad \dot{a}^4 \quad \dot{a}^6 \quad \dot{a}^8\right) \\ \frac{1}{\sqrt{2}} \quad \frac{1}{\sqrt{2}} \quad \frac{1}{\sqrt{2}} \quad \frac{1}{\sqrt{2}} \quad \frac{1}{\sqrt{2}} \end{bmatrix} \begin{bmatrix} v_a \\ v_b \\ v_c \\ v_d \\ v_e \end{bmatrix} \tag{9.1}
$$

where $\dot{a} = e^{j2\pi/5}$ and $K = 2/5$ for transformation with constant amplitude. The first two components define the space vector $\vec{v}_{\alpha\beta} = v_\alpha + jv_\beta$, while the third and fourth components define the space vector $\vec{v}_{\alpha_2\beta_2} = v_{\alpha_2} + jv_{\beta_2}$.

There are different variations of the transformation in literature, especially for the space vector $\vec{v}_{\alpha_2\beta_2}$. Hereafter, it is obtained by a double increment of the power of $\dot{a}$, as in [48].

Harmonic contents in the space vectors

The voltage, or any other electrical quantity, of the h–th phase of the five–phase machine can be expressed as the sum of its harmonic components as

$$
v_h = \sum_{\nu=-\infty}^{\infty} V_\nu e^{j\left(\nu\omega t + \varphi_\nu - \nu h \frac{2\pi}{5}\right)} \tag{9.2}
$$

where $h = 0, 1, 2, 3, 4$ for phase a, b, c, d and e, respectively. Therefore, omitting the coefficient K the space vector in the $\alpha\beta$ reference frame becomes

$$
\vec{v}_{\alpha\beta} = \sum_{h=0}^{4} \sum_{\nu=-\infty}^{\infty} V_\nu e^{j\left(\nu\omega t + \varphi_\nu + (1-\nu)h\frac{2\pi}{5}\right)} \tag{9.3}
$$

From inspection of (9.3), only the harmonics of order $\nu = 1 \pm 5k$, with $k = 0, \pm 1, \pm 2, ...$ appear in the space vector $\vec{v}_{\alpha\beta}$. Similarly, the space vector in the $\alpha_2\beta_2$ reference frame is:

$$
\vec{v}_{\alpha_2\beta_2} = \sum_{h=0}^{4} \sum_{\nu=-\infty}^{\infty} V_\nu e^{j\left(\nu\omega t + \varphi_\nu + (2-\nu)h\frac{2\pi}{5}\right)} \tag{9.4}
$$

hence, only the harmonics of order $\nu = 2 \pm 5k$, with $k = 0, \pm 1, \pm 2, ...$ appear in the space vector $\vec{v}_{\alpha_2\beta_2}$.

The new diagnostic index here proposed is defined by:

$$\vec{D} = \vec{v}_{\alpha\beta} \cdot \vec{v'}_{\alpha_2\beta_2} \tag{9.5}$$

where $\vec{v}_{\alpha\beta}$ is given in (9.3) and $\vec{v'}_{\alpha_2\beta_2}$ is the complex conjugate of $\vec{v}_{\alpha_2\beta_2}$, given in (9.4).

Asymmetry of one phase

Let us assume that a fault occurs in one phase coil and that it affects only the amplitudes of voltage harmonics. As proved in [46] in the event of a fault each voltage component is decreased. Defining κ the voltage reduction factor and a the faulty phase, the harmonic of ν–th order of the space vector $\vec{v}_{\alpha\beta}$ becomes:

$$\vec{v}_{\nu\alpha\beta} = \kappa V_\nu e^{j(\nu\omega t + \varphi_\nu)} + \sum_{h=1}^{4} V_\nu e^{j(\nu\omega t + \varphi_\nu + (1-\nu)h\frac{2\pi}{5})} \tag{9.6}$$

The amplitude of the first term can be split as:

$$\kappa V_\nu = V_\nu + V_\nu(\kappa - 1) \tag{9.7}$$

In healthy condition, the spectrum contains only the harmonics of order ν equal to $(1 \pm 5k)$ in the space vector $\vec{v}_{\alpha\beta}$ and the harmonics of order $\nu = (2 \pm 5k)$ in the space vector $\vec{v}_{\alpha_2\beta_2}$. Other harmonics form a symmetric five phase system, with sum equal to zero. During a fault condition the additional term

$$V_\nu(\kappa - 1)e^{j(\nu\omega t + \varphi_\nu)} \tag{9.8}$$

arises for each harmonic system.

It turns out that in the event of a fault all the harmonic components appear in both the spectrum of $\vec{v}_{\alpha\beta}$ and $\vec{v}_{\alpha_2\beta_2}$. During fault condition, the diagnostic index $\vec{D}$ is modified by the terms that arise in both $\vec{v}_{\alpha\beta}$ and $\vec{v'}_{\alpha_2\beta_2}$.

Let's consider a signal formed by several harmonics components (i.e. 1th, 3th, 5th, etc...); in case of healthy condition only harmonics of frequency $(1 \pm 5k)f$ appear in the $\vec{v}_{\alpha\beta}$ reference frame and only the frequencies $(2 \pm 5k)$ appear in the $\vec{v'}_{\alpha_2\beta_2}$ reference frame. In the event of a fault, all the frequencies appear (with different amplitude) in the space vectors so in the $\vec{D}$ index terms in the form:

$$... + V_\nu e^{j(\nu\omega t + \varphi_\nu)} \cdot V_\nu e^{-j(\nu\omega t + \varphi_\nu)} + ... \tag{9.9}$$
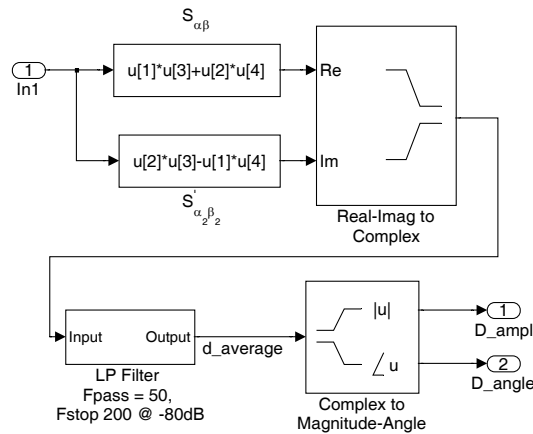
(a) *Diagnostic index construction*
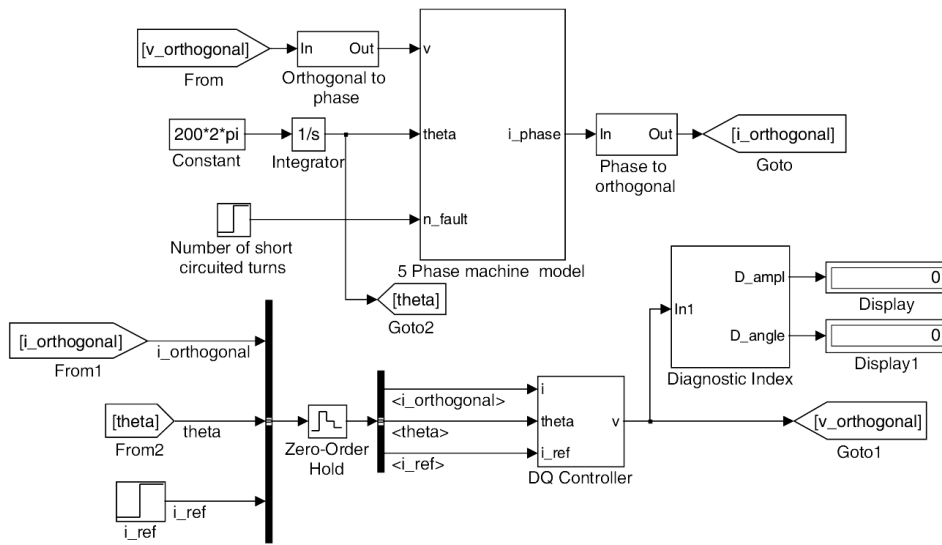
(b) *Simulink® model of the motor drive*

Figure 9.1: *Simulink® model used for the simulations*

will appear. They form DC components, as the result of the multiplication of terms with opposite frequencies (i.e. $+f$ and $-f$). In this case the average value of the diagnostic index $\vec{D}$ will be different from zero in the event of a fault. Fig. 9.1a shows the schematic diagram of the proposed index, the filter is used to eliminate the harmonic components from the signal. Only the magnitude is monitored to identify if a fault occurred.

9.2 Simulation Results

A five–phase permanent–magnet machine with 20 stator slots and 9 pole pairs have been used for tests. Each stator coil is wound around a single tooth, achieving a a single–layer winding with non–overlapped coils [52]. Each phase has a total number of turns equal to $N = 692$. The diagnostic index proposed is based on a real machine drive architecture (see Fig. 9.1b). A PI controller is used to emulate the current control loop. The controller works on a rotating reference frame synchronous with the rotor, say the dqd_2q_20 reference frame.

Because of the reference frame, there are five reference signals, that provide the real and imaginary components of the current in the rotating frames themselves (i_d^*, i_q^*, $i_{d_2}^*$, $i_{q_2}^*$ and i_0^*.) The PI controller provides each of the five components of the supplying voltage in the rotating reference frame (i.e. v_d, v_q, v_{d_2}, v_{q_2}, v_0). Then the transformation to the orthogonal reference frame $\alpha\beta\alpha_2\beta_20$ gives the signals v_α, v_β, v_{α_2}, v_{β_2}, v_0 from whose the new diagnostic index $\vec{D}$ is built, as defined in (9.5). Some simulations show that the output of the index block is a good indicator of the short circuit fault in one phase, also in case of a very low number of short circuited turns.

Fig. 9.2 shows the results of a $1.5\,s$ simulation, where at time $0.5\,s$ a current reference in q axis has been imposed equal to $i_d^* = 1$, while at time $1\,s$ a fault occurrence of 5 short–circuited turns on phase c has been imposed. It is worth noticing the diagnostic index gives a considerable indication only when a fault occurs, while it's equal to zero in healthy conditions.
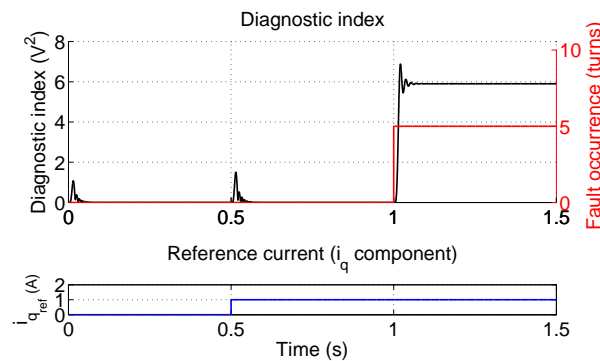

Figure 9.2: *Diagnostic index under a short–circuit fault of 5 turns in phase c*

9.3 Conclusions

The detection of the short–circuit fault has been investigated relying on the frequency analysis of a new kind of diagnostic index which combine signals from two different reference frames ($\alpha\beta$ and $\alpha_2\beta_2$) of the five phase machine.

It is proved that the partial short–circuit fault can be efficiently detected by monitoring the amplitude of the proposed diagnostic index which gives a DC output signal equal to zero during normal operation and different from zero during a fault.

Bibliography

[1] P. Salminen, "Fractional slot permanent magnet synchronous motor for low speed applications," Dissertation, 198, Lappeenranta University of Technology, Lappeenranta, Finland, 2004, iSBN 951-764-982-5(pdf).

[2] G. Atkinson, B. Mecrow, A. Jack, D. Atkinson, P. Sangha, and M. Benarous, "The design of fault tolerant machines for aerospace applications," in *Proc. of IEEE International Electrical Machines and Drives Conference*, San Antonio, Texas, 2005, May 15–18, pp. 1863–1869.

[3] N. Bianchi, M. D. Pré, G. Grezzani, and S.Bolognani, "Design Considerations on Fractional–Slot Fault–Tolerant Synchronous Motors," *IEEE Trans. on Industry Applications*, vol. 42, no. 4, pp. 997–1006, 2006.

[4] R. Zannol, "Analytical Study of Rotor Losses of a PM Motor (in italian)," Master's thesis, Department of Electrical Eng., University of Padova, 2003–2004, tutor: Prof. N. Bianchi.

[5] K. Atallah, D. Howe, P. Mellor, and D. Stone, "Rotor Loss in Permanent–Magnet Brushless AC Machines," *IEEE Transactions on Industry Applications*, vol. 36, no. 6, pp. 1612–1617, Nov/Dec 2000.

[6] T. Hiroaki, Z. Xia, J. Wang, K. Atallah, and D. Howe, "Rotor eddy–current loss in permanent magnet brushless machines," *IEEE Transactions on Magnetics*, vol. 40, no. 4, pp. 2104–2106, July 2004.

[7] N. Schofield, K. Ng, Z. Zhu, and D. Howe, "Parasitic rotor losses in a brushless permanent magnet traction machine," in *Proc. of Electric Machine and Drives Conference, EMD97*, I. C. No.444, Ed., 1–3 Sept. 1997, pp. 200–204.

[8] H. Polinder and M. J. Hoeijmaker, "Eddy current losses in segmented surface–mounted magnets of a PM machine," *IEE Proceedings of Electr. Power Appl.*, vol. 146, no. 3, pp. 261–266, May 1999.

[9] M. Shah and S. Lee, "Optimization of shield thickness of finite length rotors for eddy current loss minimization," in *Proc. of IEEE Industry Applications Society Annual Meeting, IAS06*, Miami, FL, Oct 2006, pp. 2368–2373.

[10] N. Bianchi, M. D. Pré, L. Alberti, and E. Fornasiero, *Theory and Design of Fractional–Slot PM Machines*, ser. IEEE IAS Tutorial Course notes, IAS'07 Annual Meeting. CLEUP, Padova (Italy), New Orleans, LA, September 23, 2007, (info@cleup.it).

[11] M. Shah and A. EL-Refaie, "Eddy current loss minimization in conducting sleeves of high speed machine rotors by optimal axial segmentation and copper cladding," in *Proc. of IEEE Industry Applications Society Annual Meeting, IAS07*, New Orleans, LA, 23–27 Sept 2007, pp. 544–551.

[12] M. Shah and S. Lee, "Rapid analytical optimization of eddy current shield thickness for associated loss minimization in electrical machines," in *Proc. of IEEE International on Electric Machines and Drives Conference, IEMDC05*, San Antonio, TX, May 2005, pp. 1304–1310.

[13] N. Bianchi, S. Bolognani, and E. Fornasiero, "A general approach to determine the rotor losses in three–phase fractional–slot pm machines," vol. 1, 2–5 May 2007, Antalya, Turkey, pp. 634–641.

[14] D. Diallo, M. E. H. Benbouzid, and A. Makouf, "A fault-tolerant control architecture for induction motor drives in automotive applications," *IEEE Trans. on Vehicular Technology*, vol. 53, no. 6, pp. 1847–1855, Nov. 2004.

[15] J. A. Haylock, B. C. Mecrow, A. G. Jack, and D. J. Atkinson, "Operation of a fault tolerant PM drive for an aerospace fuel pumpapplication," in *Electric Power Applications, IEE Proceedings -*, vol. 145, no. 5, Sep. 1998, pp. 441–448.

[16] L. Parsa and H. Toliyat, "Five–phase permanent–magnet motor drives," *IEEE Trans. on Industry Applications*, vol. 41, no. 1, pp. 30–37, Jan/Feb 2005.

[17] A. G. Jack, B. C. Mecrow, and J. A. Haylock, "A comparative study of permanent magnet and switched reluctance motors for high-performance fault-tolerant applications," *IEEE Trans. on Ind. Appl.*, vol. 32, no. 4, pp. 889–895, Jul./Aug. 1996.

[18] M. El Hachemi Benbouzid, "A review of induction motors signature analysis as a medium for faults detection," *IEEE Trans. on Industrial Electronics*, vol. 47, no. 5, pp. 984–993, Oct. 2000.

[19] S. Nandi, H. A. Toliyat, and X. Li, "Condition monitoring and fault diagnosis of electrical motors-a review," *IEEE Transaction on Energy Conversion*, vol. 20, no. 4, pp. 719–729, Dec. 2005.

[20] G. B. Kliman and J. Stein, "Methods of motor current signature analysis," *Electric Power Components and Systems*, vol. 20, no. 5, pp. 463 – 474, 1992.

[21] A. Bellini, F. Filippetti, G. Franceschini, C. Tassoni, and G. B. Kliman, "Quantitative evaluation of induction motor broken bars by means of electrical signature analysis," *IEEE Trans. on Ind. Appl.*, vol. 37, no. 5, pp. 1248–1255, Sep./Oct. 2001.

[22] L. Parsa and H. A. Toliyat, "Fault-tolerant five-phase permanent magnet motor drives," in *Industry Applications Conference, 2004. 39th IAS Annual Meeting. Conference Record of the 2004 IEEE*, vol. 2, Oct. 2004, pp. 1048–1054.

[23] C. B. Jacobina, I. S. Freitas, T. M. Oliveira, E. R. C. da Silva, and A. M. N. Lima, "Fault tolerant control of five-phase AC motor drive," in *Power Electronics Specialists Conference, 2004. PESC 04. 2004 IEEE 35th Annual*, vol. 5, Jun. 2004, pp. 3486–3492.

[24] J. Apsley and S. Williamson, "Analysis of multiphase induction machines with winding faults," *IEEE Trans. on Ind. Appl.*, vol. 42, no. 2, pp. 465–472, Mar./Apr. 2006.

[25] H.-M. Ryu, J.-W. Kim, and S.-K. Sul, "Synchronous-frame current control of multiphase synchronous motor under asymmetric fault condition due to open phases," *IEEE Trans. on Ind. Appl.*, vol. 42, no. 4, pp. 1062–1070, Jul./Aug. 2006.

[26] M. Liwschitz-Garik and C. C. Whipple, *Electric Machinery, vol.II, A–C Machines.* New York: D. Van Nostrand Company Inc., 1960.

[27] N. Bianchi and M. D. Pré, "Use of the star of slots in designing fractional–slot single–layer synchronous motors," *IEE Proc. – Electr. Power Appl.*, vol. 153, no. 3, pp. 459–466, May 2006, (online no. 20050284).

[28] Z. Zhu, K. Ng, N. Schofield, and D.Howe, "Improved analytical modelling of rotor eddy current losses in brushless machines equipped with surface–mounted permanent magnets," *IEE Journal, Electric Power Applications*, vol. 151, no. 6, pp. 641–650, Nov. 2004.

[29] W. Schuisky, *Berechnung Elektrischer Machinen.* Springer Verlag, Wien, 1967.

[30] J. Ede, K. Atallah, G. Jewell, J. Wang, and D. Howe, "Effect of axial segmentation of permanent magnets on rotor loss in modular permanent-magnet brushless machines," *IEEE Trans. on Industry Applications*, vol. 43, no. 5, pp. 1207–1213, Sept/Oct 2007.

[31] T.-S. Kwon, S.-K. Sul, L. Alberti, and N. Bianchi, "Design and Control of an Axial-flux Machine for a Wide Flux-weakening Operation Region," *IEEE Transactions on Industry Applications*, vol. 45, no. 4, pp. 1258–1266, Jul./Aug. 2009.

[32] F. Caricchi, F. G. Capponi, F. Crescimbini, and L. Solero, "Experimental study on reducing cogging torque and no-load power loss in axial-flux permanent-magnet machines with slotted winding," *IEEE Transactions on Industry Applications*, vol. 40, no. 4, pp. 1066–1075, Jul./Aug. 2004.

[33] N. Bianchi and E. Fornasiero, "Impact of MMF Space Harmonic on Rotor Losses in Fractional-slot Permanent-magnet Machines," *IEEE Transactions on Energy Conversion*, vol. 24, no. 2, pp. 323–328, Jun. 2009.

[34] N. Bianchi, S. Bolognani, and M. D. Pré, "Design and tests of a fault–tolerant five–phase permanent magnet motor," in *Proc. of IEEE Power Electronics Specialist Conference, PESC'06*, Jeju, Korea, 18–22 June 2006, pp. 2540–2547.

[35] N. Bianchi, S. Bolognani, M. D. Pre, and G. Grezzani, "Design considerations for fractional-slot winding configurations of synchronous machines," *IEEE Transactions on Industry Applications*, vol. 42, no. 4, pp. 997–1006, Jul./Aug. 2006.

[36] B. Mecrow, A. Jack, D. Atkinson, G. Atkinson, A. King, and B. Green, "Design and testing of a four–phase fault–tolerant permanent–magnet machine for an engine fuel pump," *IEEE Trans. on Enegy Conversion*, vol. 19, no. 4, pp. 671–678, December 2004.

[37] N. Bianchi, S.Bolognani, and G. Grezzani, "Fractional-slot IPM servomotors: analysis and performance comparisons," in *Proc. of International Conference on Electrical Machines, ICEM'04*, vol. CD Rom, paper no. 507, Cracow, Poland, 5–8 Sept. 2004, pp. 1–6.

[38] T. M. Jahns, "Improved reliability in solid state a.c. drives by means of multiple independent phase–drive units," *IEEE Trans. on Industry Applications*, vol. IA–16, no. 3, pp. 321–331, May 1980.

[39] J. Haylock, B. Mecrow, A. Jack, and D. Atkinson, "Operation of fault tolerant PM drive for an aerospace fuel pump application," *IEE Proc. – Electr. Power Appl.*, vol. 145, no. 5, pp. 441–448, Sept. 1998.

[40] J. Ede, K. Atallah, J. Wang, and D. Howe, "Effect of optimal torque control on rotor loss of fault–tolerant permanent magnet brushless machines," *IEEE Trans. on Magnetics*, vol. 38, no. 5, pp. 3291–3293, September 2002.

[41] G. Singh and V. Pant, "Analysis of a multiphase induction machine under fault condition in a phase–redundant ac drive system," *Electric Machines and Power Systems*, vol. 28, no. 6, pp. 577–590, Dec. 2000.

[42] Y. Fujimoto and T. Sekiguchi, "Fault–tolerant configuration of distributed discrete controllers," *IEEE Transactions on Industrial Electronics*, vol. 50, no. 1, pp. 86–93, February 2003.

[43] M. Barcaro, N. Bianchi, and F. Magnussen, "Analysis and tests of a dual three-phase 12-slot 10-pole permanent magnet motor," in *Energy Conversion Congress and Exposition, 2009. ECCE. IEEE*, San Jose, CA, Sep. 20–24, 2009, pp. 3587–3594.

[44] N. Bianchi, S. Bolognani, M. Dai Pre, and E. Fornasiero, "Post-fault operations of five-phase motor using a full-bridge inverter," in *Power Electronics Specialists Conference, 2008. PESC 2008. IEEE*, Rhodes, Jun. 15–19, 2008, pp. 2528–2534.

[45] N. Bianchi, S. Bolognani, and E. Fornasiero, "A General Approach to Determine the Rotor Losses in Three-phase Fractional-slot PM Machines," in *Electric Machines & Drives Conference, 2007. IEMDC '07. IEEE International*, vol. 1, Antalya, May 3–5, 2007, pp. 634–641.

[46] C. Bianchini, E. Fornasiero, T. N. Matzen, N. Bianchi, and A. Bellini, "Fault detection of a five-phase Permanent-magnet machine," in *Industrial Electronics, 2008. IECON 2008. 34th Annual Conference of IEEE*, Orlando, FL, Nov. 10–13, 2008, pp. 1200–1205.

[47] A. Bellini, F. Filippetti, G. Franceschini, and C. Tassoni, "Closed-loop control impact on the diagnosis of induction motors faults," *IEEE Trans. on Ind. Appl.*, vol. 36, no. 5, pp. 1318–1329, Sep./Oct. 2000.

[48] E. Levi, M. Jones, S. Vukosavic, A. Iqbal, and H. Toliyat, "Modeling, control, and experimental investigation of a five-phase series-connected two-motor drive with single inverter supply," *IEEE Trans. on Industrial Electronics*, vol. 54, no. 3, pp. 1504–1516, June 2007.

[49] O. Lopez, J. Alvarez, J. Doval-Gandoy, and F. D. Freijedo, "Multilevel Multiphase Space Vector PWM Algorithm," *IEEE Transactions on Industrial Electronics*, vol. 55, no. 5, pp. 1933–1942, May 2008.

[50] D. Casadei, D. Dujic, E. Levi, G. Serra, A. Tani, and L. Zarri, "General Modulation Strategy for Seven-phase Inverters With Independent Control of Multiple Voltage Space Vectors," *IEEE Transactions on Industrial Electronics*, vol. 55, no. 5, pp. 1921–1932, May 2008.

[51] U. Manual, "Finite element method magnetics," *Version 4.2*, no. http://femm.foster-miller.net, March 2, 2007.

[52] N. Bianchi, S. Bolognani, and M. D. Pré, "Design and tests of a fault–tolerant five–phase permanent magnet motor," in *Proc. of IEEE Power Electronics Specialist Conference, PESC'06*, Jeju, Korea, 18–22 June 2006, pp. 2540–2547.